

5-2019

Experimental and Computational Analysis of a 3D Printed Wing Structure

Aryslan Malik

Follow this and additional works at: <https://commons.erau.edu/edt>



Part of the [Aerodynamics and Fluid Mechanics Commons](#)

Scholarly Commons Citation

Malik, Aryslan, "Experimental and Computational Analysis of a 3D Printed Wing Structure" (2019).
Dissertations and Theses. 440.
<https://commons.erau.edu/edt/440>

This Thesis - Open Access is brought to you for free and open access by Scholarly Commons. It has been accepted for inclusion in Dissertations and Theses by an authorized administrator of Scholarly Commons. For more information, please contact commons@erau.edu.

EXPERIMENTAL AND COMPUTATIONAL ANALYSIS
OF A 3D PRINTED WING STRUCTURE

A Thesis

Submitted to the Faculty

of

Embry-Riddle Aeronautical University

by

Aryslan Malik

In Partial Fulfillment of the

Requirements for the Degree

of

Master of Science in Aerospace Engineering

May 2019

Embry-Riddle Aeronautical University

Daytona Beach, Florida

ACKNOWLEDGMENTS

I would like to express my very great appreciation to my advisor Dr. Claudia Moreno and my co-advisor Dr. Ali Yeilaghi Tamijani for their constructive feedback and constant support with the development of this research work.

I would also like to extend my thanks to the ERAU makerspace lab assistant Andrew McClary, PhD researcher Sandeep Chava, and machine shop supervisor William Russo who helped me with the experimental part of the research work.

EXPERIMENTAL AND COMPUTATIONAL ANALYSIS


OF A 3D PRINTED WING STRUCTURE

by

Aryslan Malik

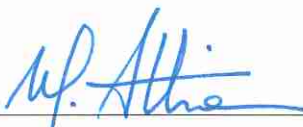
A Thesis prepared under the direction of the candidate's committee chairman, Dr. Claudia Moreno, Department of Aerospace Engineering, and has been approved by the members of the thesis committee. It was submitted to the School of Graduate Studies and Research and was accepted in partial fulfillment of the requirements for the degree of Master of Science in Aerospace Engineering.

THESIS COMMITTEE



Chairman, Dr. Claudia Moreno


Co-Advisor, Dr. Ali Yeilaghi Tamijani



Member, Dr. William MacKunis


Graduate Program Coordinator, Dr. Magdy Attia

4. 24. 2019
Date


Dean of College of Engineering, Dr. Maj Mirmirani

4/24/2019
Date


Senior Vice President for Academic Affairs and Provost, Dr. Lon Moeller

4/24/19
Date

TABLE OF CONTENTS

LIST OF TABLES	v
LIST OF FIGURES	vi
SYMBOLS	ix
ABBREVIATIONS	x
ABSTRACT	xi
1. Introduction.....	1
2. Aerodynamic Modeling	9
2.1 Vortex Lattice Method	11
2.1.1. VLM Validation	13
2.2 Doublet Lattice Method	15
2.2.1. DLM Validation	21
3. Structural Modeling	34
3.1 FEM Validation	38
4. Grid Interpolation	41
5. Analysis of the F-5 wing.....	47
5.1 Static experiment of 3D printed wing prototype	48
5.2 Static test of 3D printed wing using DIC	53
5.3 Ground Vibration Test of the 3D printed wing	61
5.4 Experimental setup of the wing in ERAU wind tunnel	70
5.5 Modal and aeroelastic analysis in Nastran/Patran	73
6. Concluding remarks and future work	80
REFERENCES	82

LIST OF TABLES

Table 1.1 F-5 fighter wing general characteristics.....	7
Table 2.1 Comparison of lift coefficients for pitching wing with AR = 2.0, 10 panels span-wise, varying number of chord-wise panels and $M = 0.8$	28
Table 3.1 Displacements of point A and B	39
Table 5.1 Displacement of tip chord trailing edge point	51
Table 5.2 Static tests performed with VIC-3D	54
Table 5.3 Case study design of flutter model via stiffness and dimension control	77

LIST OF FIGURES

Figure

1.1	Nasa Armstrong's Active Aeroelastic Wing (2004).	2
1.2	Hadley Page Bi-plane 0/400 bomber (1915).	4
2.1	Vortex and control points layout (Mason, 1998)	11
2.2	Wing geometry in Matlab Aeroelastic Code's VLM.....	13
2.3	Wing geometry in Tornado VLM	14
2.4	Comparison of pressure coefficient at the root chord of the wing.....	15
2.5	Comparison of pressure coefficient at the tip chord of the wing.....	15
2.6	Sketch of experimental model (Lessing, Troutman & Menees, 1960)	22
2.7	Geometry of the model generated in the DLM code	23
2.8	Root chord pressure distribution, bending mode	26
2.9	Tip chord pressure distribution, bending mode	27
2.10	Comparison of CL (real) for rectangular $AR = 2$ wing, $M = 0.8$, reduced frequency $k = 0.1$	29
2.11	Comparison of CL (imaginary) for rectangular $AR = 2$ wing, $M = 0.8$, reduced frequency $k = 0.1$	30
2.12	Comparison of CL (real) for rectangular $AR = 2$ wing, $M = 0.8$, reduced frequency $k = 0.5$	30
2.13	Comparison of CL (imaginary) for rectangular $AR = 2$ wing, $M = 0.8$, reduced frequency $k = 0.5$	31
2.14	Comparison of CL (real) for rectangular $AR = 2$ wing, $M = 0.8$, reduced frequency $k = 1.0$	31
2.15	Comparison of CL (imaginary) for rectangular $AR = 2$ wing, $M = 0.8$, reduced frequency $k = 1.0$	32
2.16	Comparison of CL (real) for rectangular $AR = 2$ wing, $M = 0.8$, reduced frequency $k = 2.0$	32
2.17	Comparison of CL (imaginary) for rectangular $AR = 2$ wing, $M = 0.8$, reduced frequency $k = 2.0$	33
3.1	Nodal DoF of a triangular plate in bending (Singiresu, 2017)	34
3.2	Square plate schematic.....	38
3.3	Deflection of Point A (center).....	40
3.4	Deflection of Point B (corner)	40
4.1	Example of 2x2 aerodynamic grid.....	41

4.2	FEM superimposed on 2x2 aerodynamic grid.....	42
4.3	Spline grid.....	45
5.1	Rendering of the F-5 wing.....	47
5.2	Wing internal structure (rib-spar geometry).....	48
5.3	Wing box with hidden top surface.....	48
5.4	Top view with dimensions of the 3D printed wing.....	50
5.5	3D printed F-5 wing fixture.....	50
5.6	FE model's boundary conditions.....	51
5.7	Displacement of tip chord trailing edge point as a function of load.....	52
5.8	Static test, DIC setup with (a) a speckle pattern and (b) position of cameras.....	54
5.9	DIC test 1, no-load.....	56
5.10	250-gram load case with (a) VIC-3D results and (b) Nastran results.....	57
5.11	500-gram load case with (a) VIC-3D results and (b) Nastran results.....	58
5.12	750-gram load case with (a) VIC-3D results and (b) Nastran results.....	59
5.13	1000-gram load case with (a) VIC-3D results and (b) Nastran results.....	60
5.14	Maximum z-axis displacement as a function of load.....	61
5.15	3D printed wing with a flange.....	62
5.16	Wing fixture.....	63
5.17	Force sensor mounted between a stinger and the wing.....	63
5.18	GVT test case 1, test case 4 and test case 8.....	64
5.19	Time domain response corresponding to case 1.....	65
5.20	Frequency response from input force to acceleration response for case 1.....	65
5.21	Hankel Singular Values for 32 order model.....	66
5.22	The worst (top) and the best (bottom) fit of the 32 order state-space model.....	67
5.23	Stabilization diagram.....	67
5.24	3D printed wing's experimental (top) and simulated (bottom) 1 st bending mode... 68	
5.25	3D printed wing's experimental (top) and simulated (bottom) 1 st torsion mode.....	69
5.26	ERAU wind tunnel test section.....	71
5.27	Visualization of ERAU wind tunnel section with wing model a) Rendered b) Isometric sectioned and c) Isometric side views.....	72
5.28	Top view of the wing model with dimensions.....	73
5.29	1 st bending at 18.66 Hz.....	74
5.30	1 st torsion at 57.19 Hz.....	74

5.31 $v - g$ plot of F-5 wing, "Durus" material, $E = 1.1 \text{ GPa}$, 2 feet	75
5.32 $v - f$ plot of F-5 wing, "Durus" material, $E = 1.1 \text{ GPa}$, 2 feet	75
5.33 $v - g$ plot of F-5 wing, "Durus" material, $E = 1.1 \text{ GPa}$, 3 feet	76
5.34 $v - f$ plot of F-5 wing, "Durus" material, $E = 1.1 \text{ GPa}$, 3 feet	76
5.35 $v - g$ plot of F-5 wing, "Durus" material, $E = 1.1 \text{ GPa}$, 2 feet, 1.5 mm	78
5.36 $v - g$ plot of F-5 wing, "Durus" material, $E = 1.1 \text{ GPa}$, 2 feet, 2.5 mm	78
5.37 $v - g$ plot of F-5 wing, "Durus" material, $E = 1.1 \text{ GPa}$, 2 feet, 5.0 mm	79

SYMBOLS

m_b	Total body mass
I_b	Mass inertia
V_b	Velocity
Ω_b	Angular velocity
g_E	Gravitational vector
T_{bE}	Transformation matrix
Φ_b^T	Rigid body modal matrix about c.g.
\hat{M}_f	Generalized modal mass matrix
\hat{K}_f	Generalized modal stiffness matrix
$\hat{\Sigma}_f$	Generalized damping matrix
η_f	Vector of elastic modal displacements
Φ_f^T	Flexible modal matrix
P^c	Vector of aerodynamic forces and moments
ϕ	Velocity potential
V_∞	Free stream velocity
\mathbf{v}_b	Velocity generated by vortice
\mathbf{n}_i	Normal vector to the panel i
$(u, v, w)_{ij}$	Velocities induced by vortex j on collocation point i
Γ_j	Circulation
ΔL_i	Lift of the panel i
b_i	Bound vortex length
ρ	Air density
w_{ij}	Induced normalwash at i^{th} panel
c_j	Chord length of the j^{th} panel
K	Kernel function
(x_i, y_i)	Coordinates of the i^{th} collocation point
(ξ_j, σ_j)	Coordinates along the doublet line of the j^{th} panel
ω	Frequency at which the lifting surface is oscillating
V	Free stream velocity
Δp_j	Pressure difference across the doublet at the j^{th} panel
k	Reduced frequency
\bar{q}	Free stream dynamic pressure
S	Diagonal matrix of panel areas
F_{aero}	Aerodynamic force distribution
D	Normalwash matrix
h_i	Heave displacement of i^{th} panel
θ_i	Pitch displacement of i^{th} Panel
M	Mach number
C_L	Lift coefficient

ABBREVIATIONS

3D	Three Dimension(al)
AAW	Active Aeroelastic Wing
ABS	Acrylonitrile Butadiene Styrene
AIC	Aerodynamic Influence Coefficients
AR	Aspect Ratio
CAD	Computer Aided Drawing
CFD	Computational Fluid Dynamics
cm	Centimeter
CSD	Computational Structural Dynamics
DIC	Digital Image Correlation
DLM	Doublet Lattice Method
DoF	Degree(s) of Freedom
ERAU	Embry-Riddle Aeronautical University
FE	Finite Element
FEA	Finite Element Analysis
FEM	Finite Element Method, Finite Element Model
ft	Feet
g	Gram
GPa	Gigapascal
GVT	Ground Vibration Test
Hz	Hertz
in ²	Square inch
kg	Kilogram(s)
lbs	Pound(s)
m	Meter(s)
m/s	Meter(s) per second
m ²	Square meter
mm	Millimeter
MPa	Megapascal
NASA	National Aeronautics and Space Administration
SAnD	Structural Analysis and Design
SISO	Single input, single output
SWBT	Symmetric Wing Bending Torsion
UAV	Unmanned Aerial Vehicle
VLM	Vortex Lattice Method

ABSTRACT

Malik, Ayslan MSAE, Embry-Riddle Aeronautical University, March 2019. Experimental and Computational Aeroelastic Analysis of a 3D Printed Wing Structure.

Correct prediction of aeroelastic response is a crucial part in designing flutter or divergence free aircrafts within a designated flight envelope. The aeroelastic analysis includes specifically tailoring the design in order to prevent flutter (passive control) or eliminate it by applying input on control surfaces (active control). High-fidelity models such as coupled Computational Fluid Dynamics (CFD) - Computational Structural Dynamics (CSD) can obtain full structural and aerodynamic behavior of a deformable aircraft. However, these models are so large that pose a significant challenge from the control systems design perspective. Thus, the development of an aeroelastic modeling software that can be used for further control design is the main motivation of this thesis. In addition, an aeroelastic analysis of a topologically optimized wing geometry will serve as a validation tool of the software. Initially, a 3D printed prototype of the wing is validated against static deformation tests as well as dynamic Ground Vibration Tests (GVT). The developed model is compared against the commercial software Nastran/Patran. Further plans include experimental aerodynamic test of 3D printed wing in the new Embry-Riddle Aeronautical University's (ERAU) wind tunnel to validate the proposed model.

1. Introduction

Aeroelasticity is a phenomenon that requires a thorough analysis of the combination of multiple forces such as aerodynamic, elastic and inertia forces. Contemporary airframes are becoming more flexible which in turn makes the aeroelastic analysis a crucial part of aircraft design (Livne, 2017). Aeroelasticity, generally, can be divided into static aeroelasticity and dynamic aeroelasticity. Static aeroelasticity includes major phenomena such as divergence and aileron reversal. Dynamic aeroelasticity includes the flutter phenomenon (Chinmaya & Venkatasubramani, 2009).

To be more specific an example of undesired aeroelastic phenomena is described. An aerodynamic surface (e.g., wing, canard or tail) experiences aerodynamic force normal to the airstream that increases with the square of speed and the angle of incidence which is the angle between the corresponding aerodynamic surface and the air flow (Chinmaya & Venkatasubramani, 2009). This aerodynamic force which is generally called lift will usually twist the lifting surface with its leading edge up about its elastic axis because the center of pressure is located in front of the elastic axis. This twist of the lifting surface increases the angle of incidence experienced by the corresponding aerodynamic surface which in turn increases the aerodynamic force that increases the twist further and so on until the system reaches an equilibrium condition. Undesired phenomena such as divergence occurs when the given lifting surface is deformed such that the applied aerodynamic load is increased or when the aerodynamic load is moved so as to increase the twisting effect on the structure which deflects the structure further until it fails.

When the aileron is commanded to deflect downward, the upward lift force is

created so that the aircraft can perform, for instance, a rolling maneuver. This additional lift force also creates a pitch-down moment about the elastic axis, since the deflected control surface is located behind the elastic axis. This pitch-down moment causes elastic rotation of the lifting surface section in a nose-down direction inducing down lift. The aileron is considered to be reversed when the induced down lift force exceeds the commanded up lift force created by the aileron. Extensive research was focused on the study of the dynamic phenomena that resulted in development of sophisticated analytical and computational techniques that would ensure that the design is free of flutter or any other undesired aeroelastic phenomena (Livne, 2017). One example of such research works could be NASA Armstrong's Active Aeroelastic Wing (AAW) demonstrated in Figure 1.1 which used active control of the leading edge flaps (NASA Armstrong Fact Sheets - Active Aeroelastic Wing, 2018). In essence, these control surfaces were deployed to eliminate the aileron reversal by compensating the twisting effect of the wing.



Figure 1.1 Nasa Armstrong's Active Aeroelastic Wing (2004).

Having established an understanding of static aeroelastic phenomena an example of

dynamic aeroelastic instability is outlined. Flutter is a dynamic aeroelastic phenomena that is produced by combination of elastic, inertial and unsteady aerodynamic forces that eventually causes airframe's vibration. Generally, flutter is more complex problem because it involves the vibration of the structure. In order to understand flutter phenomenon imagine rectangular unswept wing fixed rigidly on its root chord and mounted in a wind tunnel. If a wing in this configuration is disturbed without any airflow in the wind tunnel, the perturbation is damped by the structural damping of the wing structure. When the airflow speed in the wind tunnel is gradually increased the damping rate, at first, increases as well. However, as the airspeed is increased further a point is reached where the damping decreases rapidly. Critical flutter speed characterizes the condition at which constant steady amplitude is maintained by the interaction of the airflow and the structure. At airspeeds higher than the critical a small vibration in the structure could possibly trigger oscillations with increasing amplitude leading to failure of the structure. The first recorded flutter incident dates back to 1915 and involved Hadley Page's bomber Bi-plane shown in Figure 1.2 with 'violent oscillations' of the tail flutter problem (Chinmaya & Venkatasubramani, 2009). Follow-up inspection showed that the reason for flutter was that the fuselage's torsional mode coupled with independently actuated anti-symmetrical elevators' mode (Lanchester, 1916).



Figure 1.2 Hadley Page Bi-plane O/400 bomber (1915).

For several decades the flutter phenomenon was the primary focus of the research in the field of aeroelasticity (Kehoe, 1995), and it is also the primary focus of this thesis. There are different models for aeroelastic analysis and currently computational fluid dynamics and computational structural dynamics coupling is at highest modeling fidelity level. These models can provide accurate representation of the dynamic as well as aerodynamic behavior of a deformable aircraft (Livne, 2017). However, there are certain limitations to this model which makes it less practical. Firstly, it is so large that it takes considerable amount of time to simulate, so in the design environment where myriad number of simulations are required the usage of this model is still impractical. Secondly, because of the same reason the math models become too involved which poses challenges to a control system designer. Moreover, the interdisciplinary nature of the phenomenon leads to simplifications and several assumptions during formulation of the aeroelastic model therefore requiring experimental validations. Thus, the main objectives of this thesis are:

- 1) Develop a custom software for coupling of aerodynamic and structural wing forces.
- 2) Design an aeroelastic wing experiment for the new ERAU wind tunnel.

General equations related to the development of a custom aeroelastic modeling software are shown as follows:

$$\begin{bmatrix} m_b(\dot{V}_b + \Omega_b \times V_b - T_{bE}g_E) \\ I_b\dot{\Omega}_b + \Omega_b \times (I_b\Omega_b) \end{bmatrix} = \Phi_b^T P^c \quad (1.1)$$

$$\widehat{M}_f \ddot{\eta}_f + \widehat{\Sigma}_f \dot{\eta}_f + \widehat{K}_f \eta_f = \Phi_f^T P^c \quad (1.2)$$

where,

1. m_b : total body mass
2. I_b : mass inertia
3. V_b : velocity
4. Ω_b : angular velocity
5. g_E : gravitational vector
6. T_{bE} : transformation matrix
7. Φ_b^T : rigid body modal matrix about c.g.
8. \widehat{M}_f : generalized modal mass matrix
9. \widehat{K}_f : generalized modal stiffness matrix
10. $\widehat{\Sigma}_f$: generalized damping matrix
11. η_f : vector of elastic modal displacements
12. Φ_f^T : flexible modal matrix
13. P^c : vector of aerodynamic forces and moments

The structure of the aeroelastic modeling software consists of several integral parts. First is aerodynamic finite element method which is an aerodynamic analysis tool and like structural analysis it is based upon finite element approach. Since dynamic aeroelastic phenomenon is analyzed, unsteady aerodynamic forces should be considered.

These forces are generated when the flow is disturbed by the moving structure. The unsteady aerodynamics analysis allows computation of a matrix that correlates the forces acting on the lifting surface due to the displacement of the lifting surface' structure. The elements in this matrix are complex, which account for phase lags between the movement of the structure and the forces. This matrix depends on reduced frequency and Mach number and is computed by Doublet Lattice Method (DLM). Second part of the model is the structural model, which is a structural analysis method that utilizes finite element method. The structural grid is independent of the aerodynamic grid. Since, structural grid points usually do not occupy same spatial coordinates with elements of an aerodynamic grid and degrees of freedom of the structural grid may also differ from the aerodynamic grid, an aero-structure coupling is required which is usually based upon method of splines. This interpolation is a crucial feature because it allows the choice of structural and aerodynamic elements to be based upon independent considerations (Rodden & Johnson, 1994). Both custom Matlab Aeroelastic Code and Nastran/Patran are based on this type structure of aeroelastic modeling software. Prior experimental data and Nastran's Aeroelastic Module which is used on a par with its pre/post processor Patran serve as a source of verification and comparison for the custom code that is developed throughout the thesis work (Matlab Aeroelastic Code).

As the second objective is to design an aeroelastic wing experiment in the new ERAU wind tunnel, the setup is first analyzed via simulations in Nastran. For most of the simulations and experiments with the goal of validation, a specific wing geometry was chosen. This wing geometry corresponds to the Northrop Grumman's F-5 fighter wing. The Computer Aided Drawing (CAD) model of the wing was provided by the Embry-

Riddle Aeronautical University's (ERAU) Structural Analysis and Design (SAnD) Lab. The internal structure of this wing is topologically optimized with a specific geometry and configuration of spars and ribs. General data regarding the geometry of the full-scale wing is summarized in Table 1.1.

Table 1.1

F-5 fighter wing general characteristics

Characteristic	Value
Sweep-back of quarter chord	24°
Leading edge sweep	32°
Aspect ratio	~4
Taper ratio	0.2
Wing area	17.28m ²
Wingspan	8.13m

Simulations in Nastran are verified and validated as well. The structural FEM is verified with static experiment and GVT, for this purpose a smaller scale wing is 3D printed from an ABS plastic. Static experiment is carried out by applying a load on a 3D printed wing prototype and Digital Image Correlation (DIC) is chosen as data acquisition system. After experimental validation of simulations a flutter analysis is carried out in Nastran/Patran environment. The future work would include the validation of the Matlab Aeroelastic Code with a wind tunnel test that would require the manufacturing, specifically 3D printing a large (2ft) wing, and the design of the test setup rig to mount accelerometers on the wing's surface inside wind tunnel test section.

The structure of the thesis is as follows: Chapter 2 describes aerodynamic modeling approach that includes both steady aerodynamics (VLM) and unsteady aerodynamics (DLM). The chapter also includes the validation of both steady and unsteady aerodynamic models. Chapter 3 describes the structural model (FEM) developed for the Matlab Aeroelastic Code. Chapter 4 covers the interpolation between aerodynamic and structural grids and intermediate spline grid. Chapter 5 describes flutter analysis in Nastran/Patran, static and GVT experiments with 3D printed wing and preliminary experimental setup in wind tunnel. Chapter 6 provides concluding remarks and future direction for the work.

2. Aerodynamic Modeling

Aerodynamic modeling is crucial part of aeroelastic analysis and modeling. Derivation of aerodynamic equations starts from more general fluid dynamics equations. These more general equations are usually simplified to represent the most important physical aspects of aerodynamic flow (Shames, 1982; Anderson, 1984; Katz & Plotkin, 1991). Example of such simplifications can be attributed to Lifting Line Theory developed by Ludwig Prandtl in 1920's that was, at that time, one of the first aerodynamic models predicting aerodynamic forces acting on a finite lifting surface (Shames, 1982; Anderson, 1984). Prandtl Lifting Line Theory assumes that the aerodynamic flow is irrotational, inviscid and incompressible. Such flow is also known as potential flow (Shames, 1982; Anderson, 1984). Mathematical implications of such assumptions are represented in the following equations:

From the continuity equation, in an incompressible and inviscid flow:

$$\nabla \cdot \mathbf{v} = 0 \quad (2.1)$$

As the flow is irrotational a velocity potential can be introduced:

$$\mathbf{v} = \nabla \phi \quad (2.2)$$

Thus, as a result velocity potential satisfies Laplace's equation:

$$\nabla^2 \phi = 0 \quad (2.3)$$

Thenceforward, over the last century modeling of aerodynamic flows significantly developed so as to envisage different flow conditions and characteristics that range from subsonic potential flow to a more involved supersonic, viscous, compressible flow that is described by different underlying assumptions applied to Navier-Stokes equations (Shames, 1982; Anderson, 1984).

Time varying nature of unsteady flow is crucial because it affects the mathematical modeling of unsteady aerodynamics used in aeroelastic analysis. When a lifting surface experiences aerodynamic load it is deformed which changes its aerodynamic shape, and in turn alters the flow characteristic around it. This process is not instantaneous, thus unsteady aerodynamic modeling is of primary importance to capture the forces acting on a body in a time varying flow. There are various methods solving unsteady aerodynamics for the purpose of aeroelastic analysis ranging from the highest fidelity level CFD-CSD coupled solvers, which discretize Navier-Stokes equations, to the lowest fidelity level potential flow solvers based on the strip theory and 2-D infinite wing assumption (Livne, 2017).

High fidelity CFD-CSD coupled solvers are capable of capturing accurate structural and dynamic behavior of the lifting surface, yet computationally expensive and involved which renders them as impractical as far as the control system design perspective is concerned (Livne, 2017). Contrarily, aerodynamic models based on strip theory are relatively simple and computationally inexpensive compared to high fidelity models. However, strip theory may lack accuracy required for the aeroelastic analysis (Livne, 2017). Potential flow based panel methods can be considered as middle tier fidelity aerodynamic models which satisfy the requirements of aeroelastic analysis and at the same time not as computationally demanding as high fidelity models while still retaining reasonable accuracy of lifting characteristics of finite wings, and readily applicable to control system design (Katz & Plotkin, 1991). Panel methods such as Vortex Lattice Method (VLM) and Doublet Lattice Method (DLM) are used for the purpose of aerodynamic modeling where the former is used for steady part of the solution and the

latter is essentially unsteady oscillatory extension of the VLM.

2.1 Vortex Lattice Method

The VLM is a potential flow solver that utilizes planar surfaces (panels) to represent lifting surfaces (e.g. wing, canard, tail etc.) (Moran, 1991). According to Kutta-Joukowski theorem the vortices represent lift and are placed on the quarter chord of each panel. Boundary condition of zero normal velocity on the panel surface is satisfied on so called collocation (control) point of each panel that is located at $3/4$ of the chord (Katz & Plotkin, 1991). Described positioning of vortices and collocation points is not a theoretical law but rather a rule of thumb that works well for this method and also it is known as “ $1/4 - 3/4$ rule” (Mason, 1998). *Figure 2.1* demonstrates the placement of the bound vortices and control points.

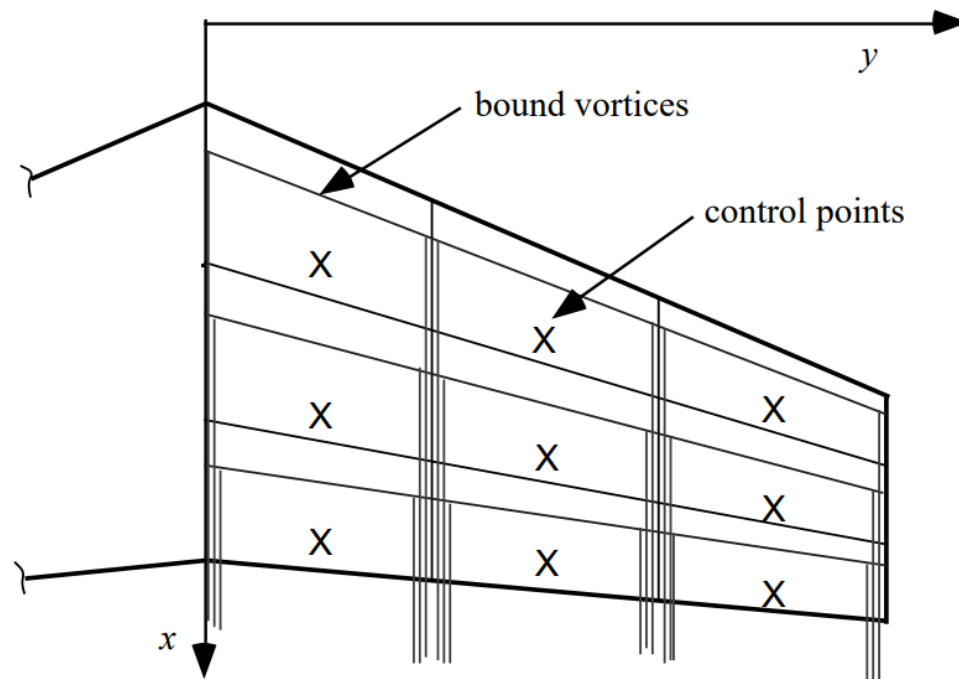


Figure 2.1 Vortex and control points layout (Mason, 1998)

Generally, the procedure for the VLM panel method is as follows:

Firstly, the lifting surface is discretized into lattice of quadrilateral panels.

Generally a collection of panels describing lifting surface is referred to as aerodynamic grid. Secondly, the zero normal flow condition is satisfied on every panel's collocation (control) point. This is defined by the addition of already known free stream velocity \mathbf{V}_∞ and unknown velocities \mathbf{v}_b generated by vortices:

$$(\mathbf{V}_\infty + \mathbf{v}_b) \cdot \mathbf{n} = 0 \quad (2.4)$$

Equation 2.4 is satisfied at every collocation point, and combined with Biot-Savart Law that leads to the following compact formulation of influence coefficients (more detailed derivation is presented in (Katz & Plotkin, 1991)):

$$a_{ij} = (u, v, w)_{ij} \cdot \mathbf{n}_i \quad (2.5)$$

where, \mathbf{n}_i is the normal vector to the panel i and $(u, v, w)_{ij}$ represent velocities induced by vortex j on collocation point i . Combining above Equation 2.5 leads to the following linear system of equations:

$$\begin{bmatrix} a_{11} & a_{12} & \dots & a_{1N} \\ a_{21} & a_{22} & \dots & a_{2N} \\ \vdots & \vdots & \ddots & \vdots \\ a_{N1} & a_{N2} & \dots & a_{NN} \end{bmatrix} \begin{bmatrix} \Gamma_1 \\ \Gamma_2 \\ \vdots \\ \Gamma_N \end{bmatrix} = \begin{bmatrix} -V_\infty \cdot \mathbf{n}_1 \\ -V_\infty \cdot \mathbf{n}_2 \\ \vdots \\ -V_\infty \cdot \mathbf{n}_N \end{bmatrix} \quad (2.6)$$

where Γ_j are unknown circulations. After circulations are calculated the lift can be obtained as follows:

$$\Delta L_i = \rho V_\infty \times \Gamma_i \Delta b_i \quad (2.7)$$

where ΔL_i is the lift of the panel i and b_i is the bound vortex length. In order to calculate the total lift of the lifting surface all panels' lift contributions are summed.

2.1.1. VLM Validation

A specific wing geometry was analyzed in order to validate the VLM code that is based on a code developed by University of Minnesota UAV lab (Kotikalpudi, 2017). This specific geometry was chosen because there are experimental results available for this geometry that can be used to validate against. The wing under consideration has an aspect ratio of 3, quarter chord sweep angle of 45, taper ratio of 0.5 and zero dihedral angle. Panels are distributed in such a way that there are 6 panels in chordwise direction and 8 panels in spanwise direction resulting in 48 panels for half of the wing, and if symmetry is considered – 96. The wing geometry generated in the Matlab Aeroelastic Code's VLM is shown in *Figure 2.2* and wing geometry generated in Tornado VLM is presented in *Figure 2.3*.

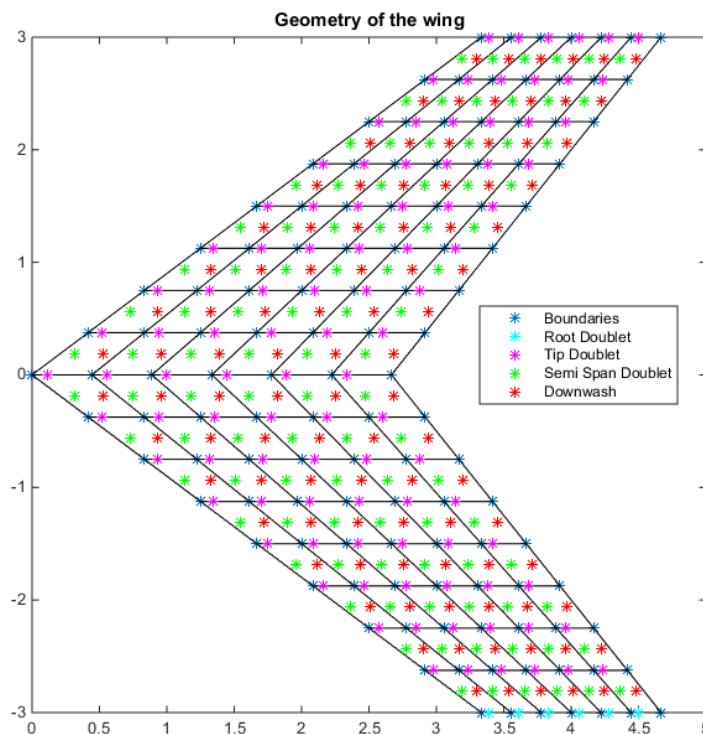


Figure 2.2 Wing geometry in Matlab Aeroelastic Code's VLM

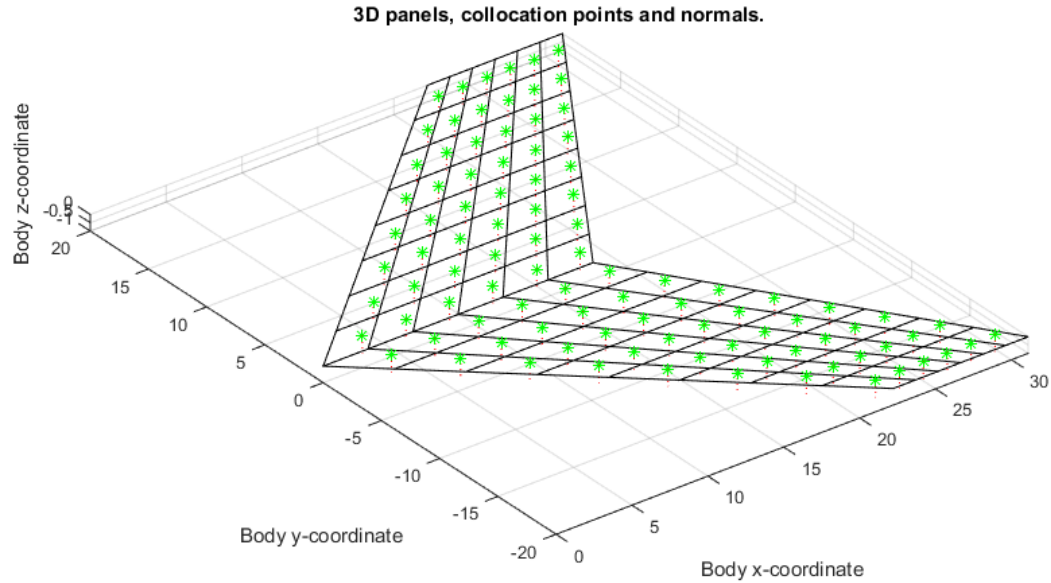


Figure 2.3 Wing geometry in Tornado VLM

In order to validate the Vortex Lattice Method (VLM) the results of the Matlab Aeroelastic code were compared against experimental results and numerical results obtained by Albano-Rodden VLM (Albano & Rodden, 1969) as well as Tornado VLM developed by Department of Aeronautics at the KTH Royal Institute of Technology (Melin, 2000). Flight conditions are as follows: the angle of attack is 4 degrees and the Mach number is 0.8. Particularly, the pressure coefficients at the root chord, shown in *Figure 2.4*, and tip chord, demonstrated in *Figure 2.5*, of a tapered and swept wing at an incidence in a steady flow were compared.

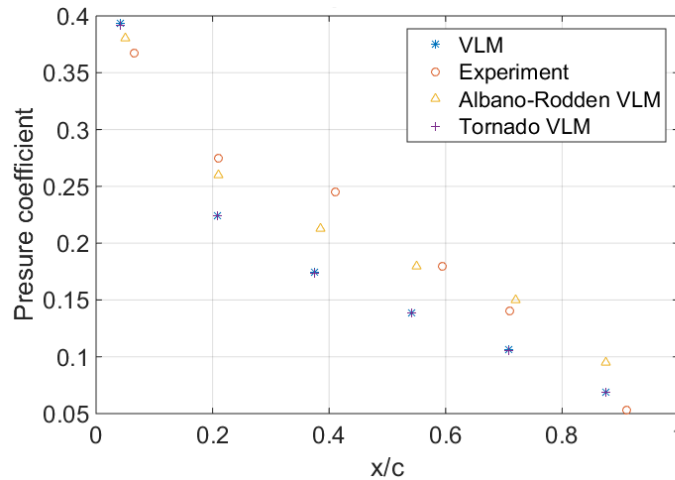


Figure 2.4 Comparison of pressure coefficient at the root chord of the wing

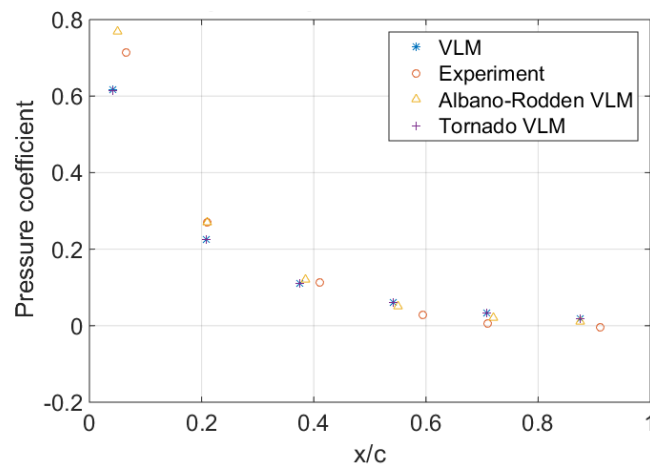


Figure 2.5 Comparison of pressure coefficient at the tip chord of the wing

The results indicate that the developed VLM overestimate the pressure at the leading edge and underestimate it further down the chord line in the case of root chord, which can be observed in *Figure 2.4*. As far as tip chord is concerned (*Figure 2.5*) it can be inferred that the developed VLM vice-versa underestimate the pressure at the leading edge and slightly overestimate it starting from the half chord. Moreover, it is crucial to note that the results obtained by VLM almost identically match the results obtained using Tornado VLM.

2.2 Doublet Lattice Method

Essentially, DLM can be considered as a panel method relying on potential flow assumption with unsteady oscillatory extension of the steady VLM discussed in section 2.1 (Albano & Rodden, 1969). The VLM is extended to account for oscillatory doublets of constant strength to the bound vortex along the quarter-chord of each box. Similarly to VLM, the points located at $3/4$ of any given panel's chord are normalwash calculation points, also known as collocation points (Katz & Plotkin, 1991; Albano & Rodden, 1969). Normalwash is the normal flow to the panel's surface normalized with respect to the freestream velocity (Katz & Plotkin, 1991; Albano & Rodden, 1969). Both doublet lines and freestream flow induce normalwash. The DLM utilizes the normalwash distribution to calculate the pressure distribution across panels that describe the lifting surface.

The relation between normalwash distribution and pressure distribution is produced in an involved process of derivation which includes several simplifying approximations and is shown in detail in (Albano & Rodden, 1969; Rodden, Taylor & McIntosh, 1998). Thus, a concise overview pertinent to the utilization of the DLM to aeroelasticity is presented henceforth.

As it was mentioned previously the main objective of the DLM is to relate the normalwash distribution due to free stream generated by doublet lines to a corresponding pressure distribution acting on the lifting surface undergoing oscillatory motion with a specific frequency. In order to accomplish this goal as a first step the lifting surface is discretized to a lattice similar to the aerodynamic grid used in VLM. However, in this case a doublet line is placed on the quarter chord of each panel.

The second step is to construct the downwash matrix D that is obtained by

computing the normalwashes induced by each doublet line at all collocation points on the lifting surface. The normalwash produced at the i^{th} collocation point due to the doublet line on j^{th} panel in terms of pressure distribution is given as a following integral:

$$w_{ij} = \frac{c_j}{8\pi} \int_{-\frac{L}{2}}^{\frac{L}{2}} K(x_i, y_i, \xi_j(l), \sigma_j(l), \omega, V) \Delta p_j dl \quad (2.8)$$

where,

1. w_{ij} : induced normalwash at i^{th} panel
2. c_j : chord length of the j^{th} panel
3. K : Kernel function relating the normalwash produced by an infinitesimal acceleration doublet to the pressure difference across it
4. (x_i, y_i) : coordinates of the i^{th} collocation point at which normalwash is computed
5. (ξ_j, σ_j) : coordinates along the doublet line of the j^{th} panel
6. ω : frequency at which the lifting surface is oscillating
7. V : free stream velocity
8. Δp_j : pressure difference across the doublet at the j^{th} panel

Total normalwash at the i^{th} panel can be calculated by summing contributions of every panel as follows:

$$w_{ij} w_i = \sum_{j=1}^{j=N} D_{ij} \Delta p_j \quad (2.9)$$

$$D_{ij} = \frac{c_j}{8\pi} \int_{-\frac{L}{2}}^{\frac{L}{2}} K(x_i, y_i, \xi_j(l), \sigma_j(l), \omega, V) \quad (2.10)$$

where N is the total number of panels describing the lifting surface. The resulting

normalwash w_i is a harmonic function because the pressure distribution Δp_j is harmonic function as well. The Equations 2.9-2.10 can be re-written in matrix form as follows:

$$\bar{w} = D\bar{p} \quad (2.11)$$

where \bar{w} denotes a vector of $N \times 1$ dimension containing all total induced normalwash at each panel produced by doublet lines at each panel, D represents the normalwash matrix of $N \times N$ dimension, and \bar{p} is the pressure difference vector of $N \times 1$ dimension that contains pressure difference across each panel. It is worth to mention that the D_{ij} depends only on the geometry of the lifting surface and known flow condition. Thus, the D matrix can be obtained by integrating the kernel function K along each doublet line. The detailed process of integration can be found in (Albano & Rodden, 1969; Watkins, Woolston & Cunningham, 1959). The crucial aspect of the formulation is that the equations given in (Albano & Rodden, 1969; Watkins, Woolston & Cunningham, 1959) allow the usage of non-dimensional parameter called reduced frequency that combines free stream velocity, oscillating frequency and given reference chord presented as follows:

$$k = \frac{\omega \bar{c}}{2V} \quad (2.12)$$

Thus, for a given geometry of the lifting surface the D matrix becomes a function of solely reduced frequency. As shown previously, the D matrix maps the pressure difference across the panels produced by respective doublet lines to the induced downwash at each panel's collocation point. Since the pressure vector is unknown, a further step is taken by inverting the D matrix. The inverted D matrix is also known as Aerodynamic Influence Coefficients (AIC) matrix (Kotikalpudi, 2017). The equations solving for the pressure difference vector are given as:

$$\bar{p} = D^{-1}\bar{w} \quad (2.13)$$

$$k = \frac{\omega\bar{c}}{2V} \quad (2.14)$$

The next step is to apply zero net normal flow boundary condition which is a physical constraint stating that there cannot be any flow passing perpendicularly to the discretized panels (Kotikalpudi, 2017). Ideally this condition should be satisfied across the entire surfaces of all panels, however, in practice it is satisfied on the collocation points (Kotikalpudi, 2017). In the model the boundary condition is satisfied by relating the induced normalwash vector \bar{w} produced by the doublet lines to the normalwash distribution vector \bar{w}_∞ due to the free stream as follows:

$$\bar{w} + \bar{w}_\infty = 0 \quad (2.15)$$

Thus, the pressure difference can be found using the normalwash distribution vector due to the free stream:

$$\bar{p} = -[AIC(k)]\bar{w}_\infty \quad (2.16)$$

Using the Equation 2.16 the pressure distribution of an oscillating lifting surface can be found from the free stream normalwash distribution. \bar{w}_∞ vector is calculated from the given flow condition and the motion of the lifting surface. For small angles the normalwash vector \bar{w}_∞ is identical to the angle of attack. Vectors \bar{p} and \bar{w}_∞ are both harmonic functions in oscillating frequency ω .

It can be observed that the vector \bar{w}_∞ contains the normalwash of each individual panel. This implies that if an elastic deformation of a given lifting surface can be approximated by the motion of the discretized panels, the corresponding normalwash vector \bar{w}_∞ can be computed (Kotikalpudi, 2017). Consequently, Equation 2.16 can be readily used to obtain the pressure distribution across panels corresponding the elastic

deformation of the lifting surface (Kotikalpudi, 2017). The aerodynamic force distribution can be calculated as follows:

$$F_{aero}(k) = \bar{q}S\bar{p} \quad (2.17)$$

$$F_{aero}(k) = \bar{q}S[AIC(k)]\bar{w} \quad (2.18)$$

where \bar{q} is the free stream dynamic pressure and S is a diagonal matrix of panel areas (Kotikalpudi, 2017). The obtained aerodynamic force acts at the midpoint of the doublet line at each panel.

The DLM is generally more involved than the VLM, and thus involves more assumptions and approximations. The implications of such approximations is that at zero oscillating frequency the DLM result is not as accurate as the result obtained by VLM (Katz & Plotkin, 1991; Albano & Rodden, 1969; Rodden, Taylor & McIntosh, 1998). Therefore, for the same aerodynamic grid in order to improve the accuracy of the DLM result it is suggested to superimpose unsteady solution of the DLM to the steady solution of the VLM as given in (Rodden, Taylor & McIntosh, 1998).

In order to incorporate steady solution of the VLM into the unsteady part of the DLM solution it is required to obtain the incremental downwash matrix that represents solely unsteady effects. Incremental downwash matrix is found by obtaining the downwash matrix twice using the DLM, first, it is calculated at the given frequency and subsequently it is computed at zero frequency. This is demonstrated in the following Equation 2.19:

$$D_{unsteady}(k) = D_{\omega}(k) - D_0 \quad (2.19)$$

where $D_{unsteady}$ is the incremental downwash matrix that represents only the unsteady part of the DLM solution, D_{ω} is the downwash matrix computed at the given frequency ω

and D_0 is the downwash matrix calculated at zero frequency (Kotikalpudi, 2017). Note that the downwash matrix at zero frequency D_0 is not a function of reduced frequency k since by setting the oscillating frequency to zero the reduced frequency becomes zero as well.

Total solution is obtained by combining unsteady part of the DLM solution which is the incremental downwash matrix $D_{unsteady}$ and steady part is provided by the VLM solution, in an essence the VLM solution compensates the subtracted D_0 and bolsters the accuracy of the result. The steady part is obtained as shown in section 2.1. It is important to mention that downwash matrices are compatible only if the same aerodynamic grid is used for both the computation of incremental downwash matrix using the DLM and for obtaining steady state downwash matrix using the VLM. Total downwash matrix is obtained as follows:

$$D_{total}(k) = D_{unsteady}(k) + D_{VLM} \quad (2.20)$$

where $D_{total}(k)$ is the total downwash matrix that consists of both steady state downwash matrix D_{VLM} computed using the VLM and unsteady incremental downwash matrix $D_{unsteady}$. The improved AIC matrix is given as follows:

$$[AIC(k)] = D_{total}^{-1}(k) \quad (2.21)$$

As it was mentioned earlier, in order to use the DLM in aeroelastic analysis it is necessary to express the free stream normalwash vector \bar{w}_∞ so that it accounts for the elastic deformation of a lifting surface (Kotikalpudi, 2017). This topic is discussed in detail in the following DLM validation section.

2.2.1. DLM Validation

The DLM is verified with experimental data and previous DLM codes. The DLM

code used in this thesis is based on a work of University of Minnesota UAV Lab (Kotikalpudi, 2017).

Firstly, a lift distribution on a rectangular wing with aspect ratio of 3 oscillating in bending mode is used as a source of validation. Experimental measurements of lift distribution are provided by (Lessing, Troutman & Menees, 1960). Dimensional sketch of the model is given in *Figure 2.6*.

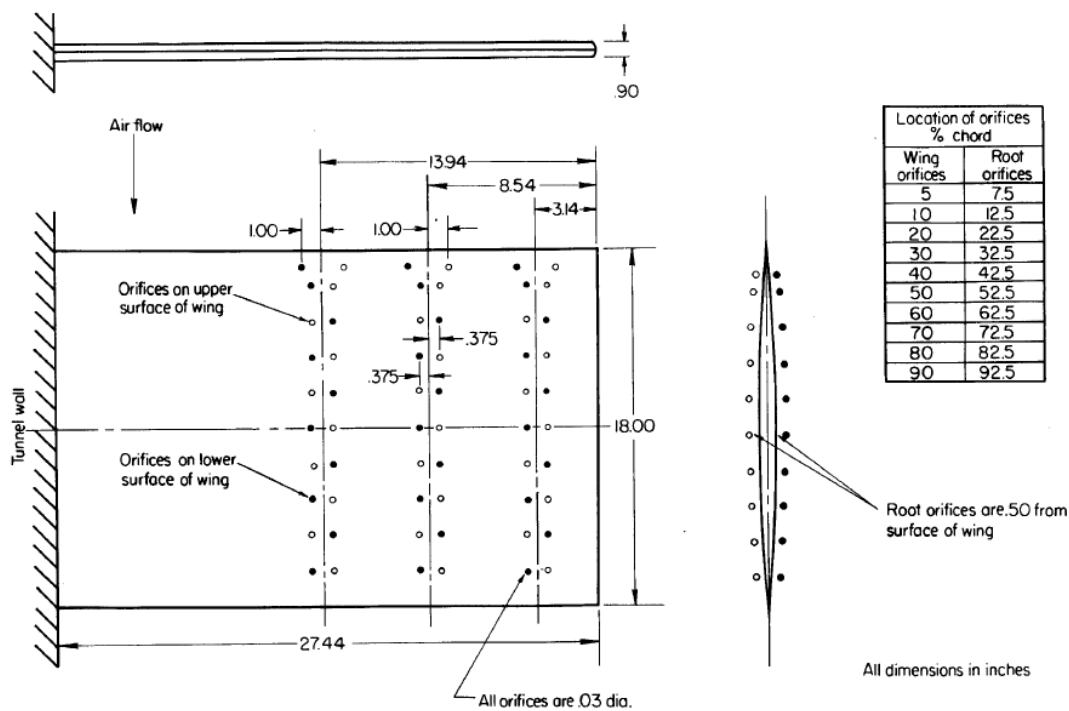


Figure 2.6 Sketch of experimental model (Lessing, Troutman & Menees, 1960)

Corresponding geometry generated in the DLM code is given in *Figure 2.7*

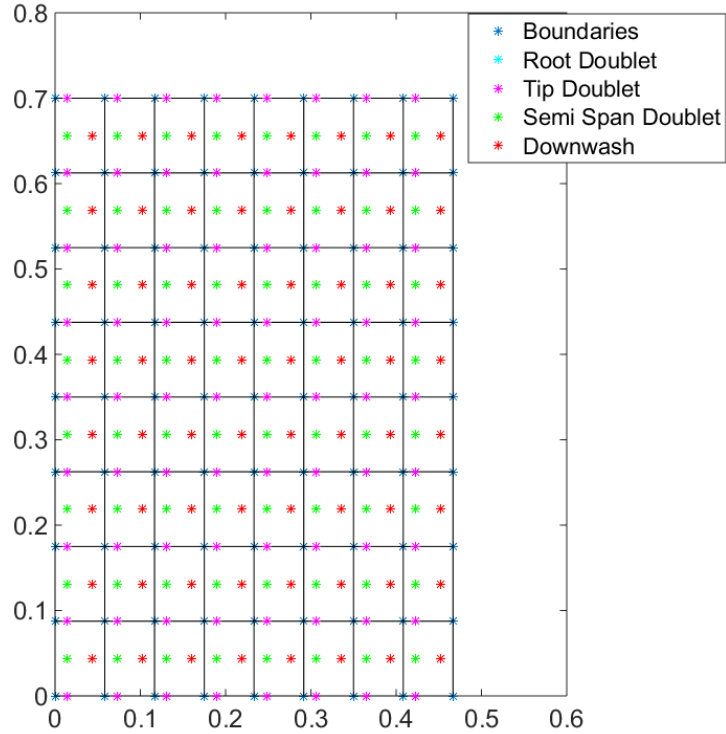


Figure 2.7 Geometry of the model generated in the DLM code

The wing is oscillating in a bending mode that can be described by Equation 2.22:

$$\bar{h} \approx 0.1804|(y/s)| + 1.702(y/s)^2 - 1.136|(y/s)|^3 + 0.253(y/s)^4 \quad (2.22)$$

where, \bar{h} is the heave (vertical displacement) of the lifting surface, y is the span-wise coordinate, s is the span of the lifting surface, in this case it is the span of the wing. In the case of the DLM code y takes discrete values since the lifting surface (wing) is discretized to 8 panels chord-wise and 8 panels span-wise. For a given specific case y becomes a vector and takes the span-wise coordinates of the downwash points. Thus, \bar{h} becomes a vector as well allowing the usage of the DLM techniques described in section 2.2.

The deformation vector \bar{h} that describes the bending of the wing cannot be directly used in aeroelastic analysis, as it was mentioned before the elastic deformation of the lifting surface given by the vector \bar{h} should be first expressed in the form the free stream

normalwash vector \bar{w}_∞ so that Equation 2.23 can be used to obtain the pressure distribution:

$$\bar{p} = -[AIC(k)]\bar{w}_\infty \quad (2.23)$$

The next step is, thus, to calculate the normalwash on panels due to their corresponding heave and/or pitch motion. Pitch motion is considered in the model to make it more general. Special matrices called differentiation matrices D_1 and D_2 are constructed in order to relate the motion of the panels to their corresponding normalwashes (Kier & Looye, 2009). The differentiation matrix D_1 maps the panels' displacement to the downwash at the collocation point, and D_2 maps the panels' velocity to the downwash at the same point. Equations 2.24-2.25 represent the relation of motion and corresponding normalwash:

$$u_{aero}^i = \begin{bmatrix} \theta_i \\ h_i \end{bmatrix} \quad (2.24)$$

$$w_i = D_{1i}u_{aero}^i + D_{2i}\dot{u}_{aero}^i \quad (2.25)$$

where, u_{aero}^i is the aerodynamic degrees of freedom (DoF) of, θ_i is the pitch displacement, h_i is the heave displacement, w_i is the downwash at collocation point, D_{1i} is the displacement differentiation matrix, D_{2i} is the velocity differentiation matrix, \dot{u}_{aero}^i is the velocity of the i^{th} panel's DoF. It should be noted that the heave displacement does not produce any downwash at the collocation point; however the pitch displacement produces the equivalent amount of downwash for small angles because the rotation of the panel about its pitch axis results in perpendicular flow at the collocation point (Kotikalpudi, 2017). Also, both heave velocity \dot{h}_i and pitch rate $\dot{\theta}_i$ induce downwash at the collocation point given by $-\dot{h}_i/V$ and $\dot{\theta}_i c_i/4V$ respectively, where c_i is the chord

length of i^{th} panel (Kier & Looye, 2009). The normalwash is, thus, formulated as follows:

$$D_{1i} = [1 \quad 0] \quad (2.26)$$

$$D_{2i} = \frac{2}{\bar{c}} \begin{bmatrix} c_i & \\ 4 & -1 \end{bmatrix} \quad (2.27)$$

$$w_i = D_{1i}[\theta_i \quad h_i]^T + D_{2i}[\dot{\theta}_i \quad \dot{h}_i]^T \frac{\bar{c}}{2V} \quad (2.28)$$

The differentiation matrix D_{2i} is normalized with respect to the reference chord \bar{c} so that $\bar{c}/2V$ factor is isolated which later is combined with oscillating frequency ω in order to be expressed as reduced frequency k . Both θ_i and h_i are harmonic functions of oscillating frequency ω , thus $\dot{\theta}_i$ and \dot{h}_i can be expressed as follows:

$$\theta_i = \theta_0 e^{i\omega t} \quad (2.29)$$

$$h_i = h_0 e^{i\omega t} \quad (2.30)$$

$$\dot{\theta}_i = i\omega \theta_i \quad (2.31)$$

$$\dot{h}_i = i\omega h_i \quad (2.32)$$

The normalwash can be rewritten as:

$$w_i = (D_{1i} + ikD_{2i})[\theta_i \quad h_i]^T \quad (2.33)$$

The differentiation matrices D_{1i} and D_{2i} are computed for all panels and combined in block-diagonal manner in the DLM code so that the total differentiation matrices D_1 and D_2 are obtained.

In the case of the validation, the wing is oscillating in bending mode and thus its i^{th} panel has heave h_i and zero pitch θ_i . Thus, the normalwash on i^{th} panel can be expressed as follows:

$$w_i^{val} = (ikD_{2i})[0 \quad h_i]^T \quad (2.34)$$

$$D_{2i} = \frac{2}{\bar{c}} \begin{bmatrix} \frac{c_i}{4} & -1 \end{bmatrix} \quad (2.35)$$

$$w_i^{val} = ik \frac{2}{\bar{c}} \begin{bmatrix} \frac{c_i}{4} & -1 \end{bmatrix} [0 \quad h_i]^T \quad (2.36)$$

$$w_i^{val} = -ik \frac{2}{\bar{c}} h_i \quad (2.37)$$

It can be noticed that the differentiation matrix D_{1i} is absent since it is only related to pitch θ , which is zero in the case of a lifting surface oscillating in bending mode. The pressure acting on the panels can be computed using Equation 2.28:

$$\bar{p} = -[AIC(k)]w^{val} \quad (2.38)$$

The result of pressure distribution on the root chord is given in *Figure 2.8* and the pressure distribution on the tip chord is shown in *Figure 2.9*. Mach number M is 0.24 and the reduced frequency k is set to 0.47 to match the experimental flight condition.

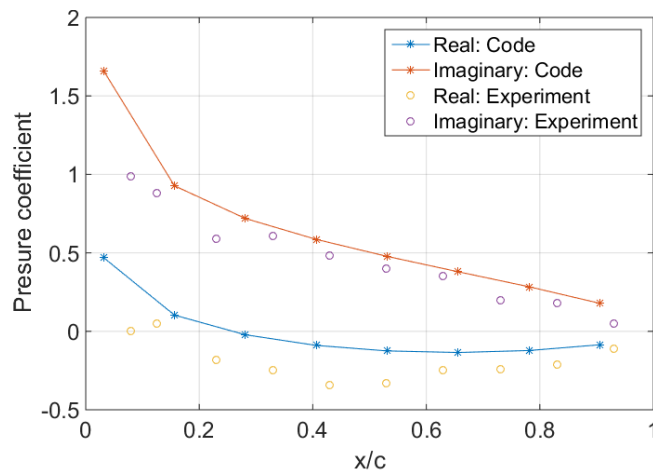


Figure 2.8 Root chord pressure distribution, bending mode

It can be observed from *Figure 2.8* that the DLM slightly overestimate the

imaginary and real values of the pressure distribution.

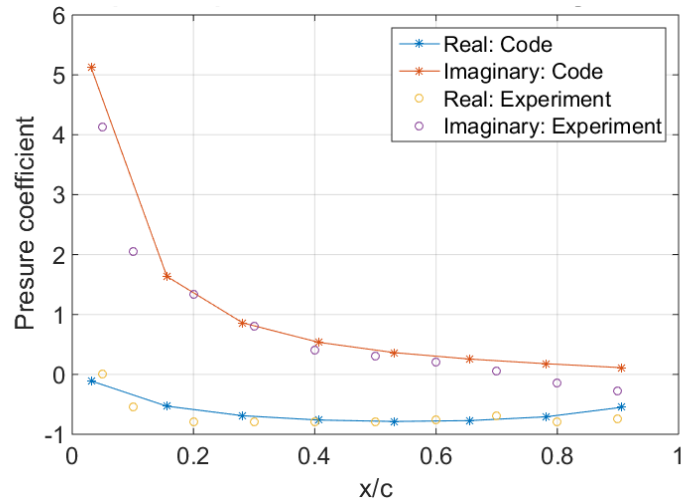


Figure 2.9 Tip chord pressure distribution, bending mode

Figure 2.9 demonstrates that the code is in good agreement with the experimental results for the case of tip chord pressure distribution.

The custom DLM code is also verified with other DLM codes, namely N5KQ and N5KA where former code uses more accurate quartic approximation in the kernel numerator and the latter utilizes parabolic approximation (Rodden, Taylor, McIntosh & Baker, 1999). In this case, authors studied the effect of panel's aspect ratio (AR) on rectangular wings that are pitching about their mid-chord at $M = 0.8$. The AR of the wing is 2 and it is divided into 10 equal span-wise strips, after that the number of chord-wise panels is varied from 5 to 100 that, in turn, varies the ARs of panels from 0.5 to 10.0. Moreover, the reduced frequencies are varied as well from $k = 0.1$ to 2.0. It should be noted that the normalwash vector was calculated differently in this case because the panels describing lifting surface are pitching about their respective mid-chords. The results for lift coefficient C_L are presented below in Table 2.1 where both imaginary and real values are given.

Table 2.1

Comparison of lift coefficients for pitching wing with $AR = 2.0$, 10 panels span-wise, varying number of chord-wise panels and $M = 0.8$

k	Chord-wise panels	N5KQ		N5KA		Custom DLM	
		Real	Imaginary	Real	Imaginary	Real	Imaginary
0.1	5	2.968	0.3626	2.968	0.3626	2.9681	0.3509
0.1	10	2.968	0.3565	2.975	0.3653	2.9832	0.3462
0.1	20	2.971	0.3563	2.977	0.3657	2.9881	0.3439
0.1	50	2.972	0.3560	2.978	0.3658	2.9893	0.3433
0.1	100	2.972	0.3560	2.978	0.3658	2.9895	0.3433
0.5	5	3.638	1.739	3.638	1.739	3.3094	1.6609
0.5	10	3.770	1.724	3.810	1.731	3.5659	1.5385
0.5	20	3.859	1.712	3.870	1.724	3.6526	1.4839
0.5	50	3.898	1.706	3.885	1.723	3.6732	1.4699
0.5	100	3.902	1.705	3.887	1.722	3.6756	1.4684
1.0	5	4.492	1.823	4.492	1.823	3.6661	2.6431
1.0	10	4.768	1.528	4.820	1.479	4.5425	2.3065
1.0	20	4.901	1.313	4.920	1.338	4.8250	2.1146
1.0	50	4.948	1.212	4.930	1.303	4.8901	2.0628
1.0	100	4.953	1.200	4.932	1.300	4.8974	2.0569
2.0	5	4.652	2.380	4.652	2.380	2.7568	4.1813
2.0	10	5.396	1.814	5.461	1.729	5.2472	2.0019
2.0	20	5.720	1.393	5.681	1.449	5.7793	1.1570
2.0	50	5.840	1.194	5.730	1.378	5.8561	0.9452

k	Chord-wise panels	N5KQ		N5KA		Custom DLM	
		Real	Imaginary	Real	Imaginary	Real	Imaginary
2.0	100	5.854	1.170	5.735	1.371	5.8636	0.9216

Figure 2.10 through Figure 2.17 show the real and imaginary C_L of custom DLM code, which is shown in blue line, compared with the real and imaginary C_L of N5KQ (shown in red) and N5KA (shown in cyan) as the number of chord-wise panels is increased from 5 to 100.

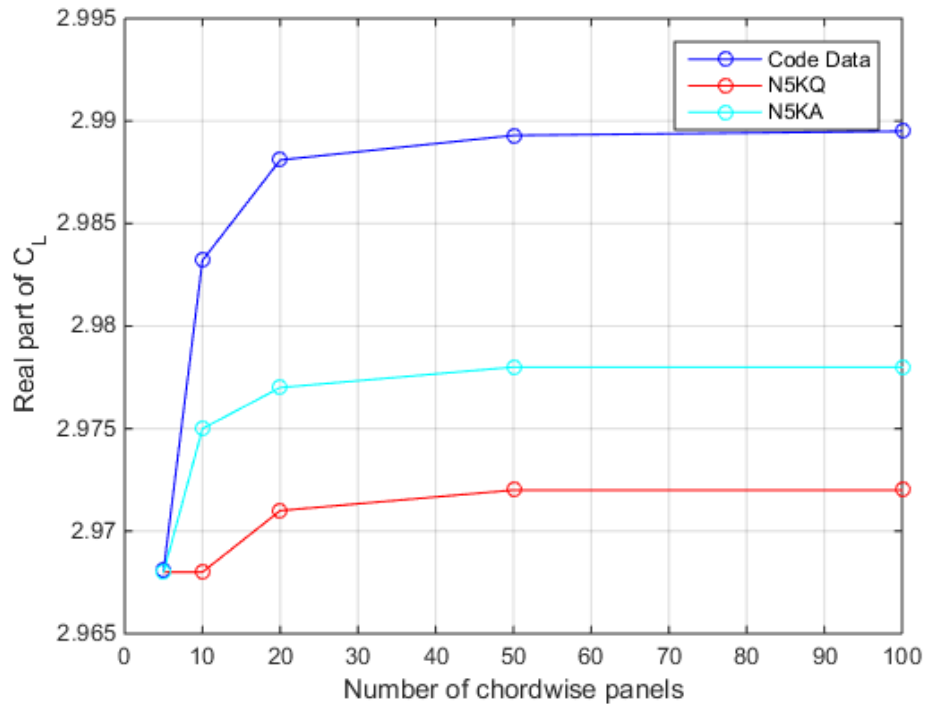


Figure 2.10 Comparison of C_L (real) for rectangular AR = 2 wing, M = 0.8, reduced frequency $k = 0.1$

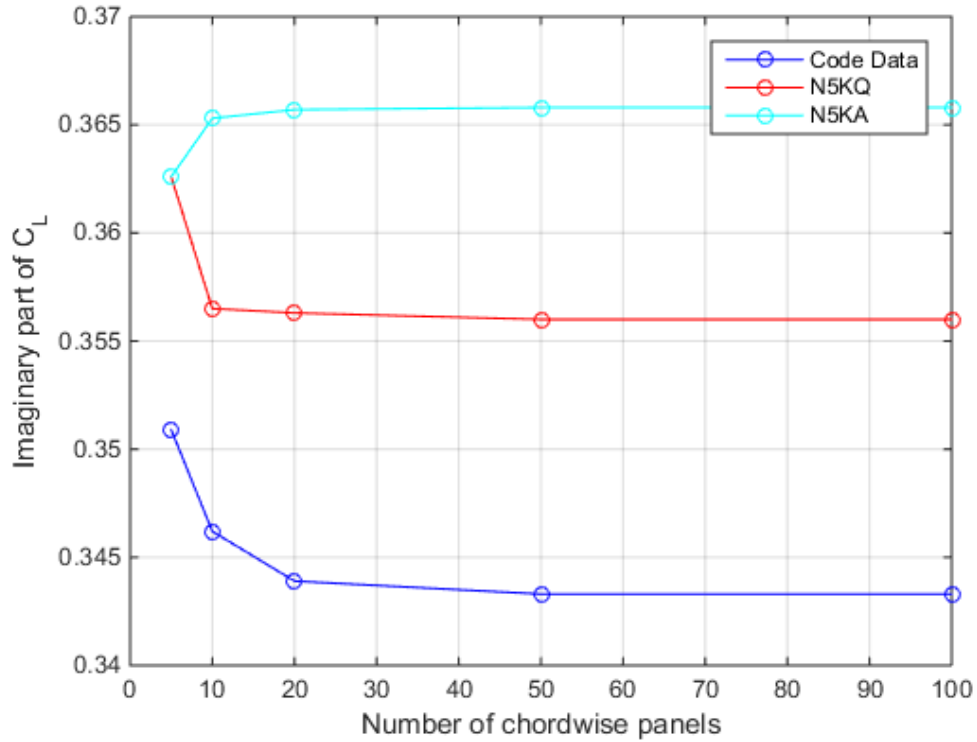


Figure 2.11 Comparison of C_L (imaginary) for rectangular $AR = 2$ wing, $M = 0.8$, reduced frequency $k = 0.1$

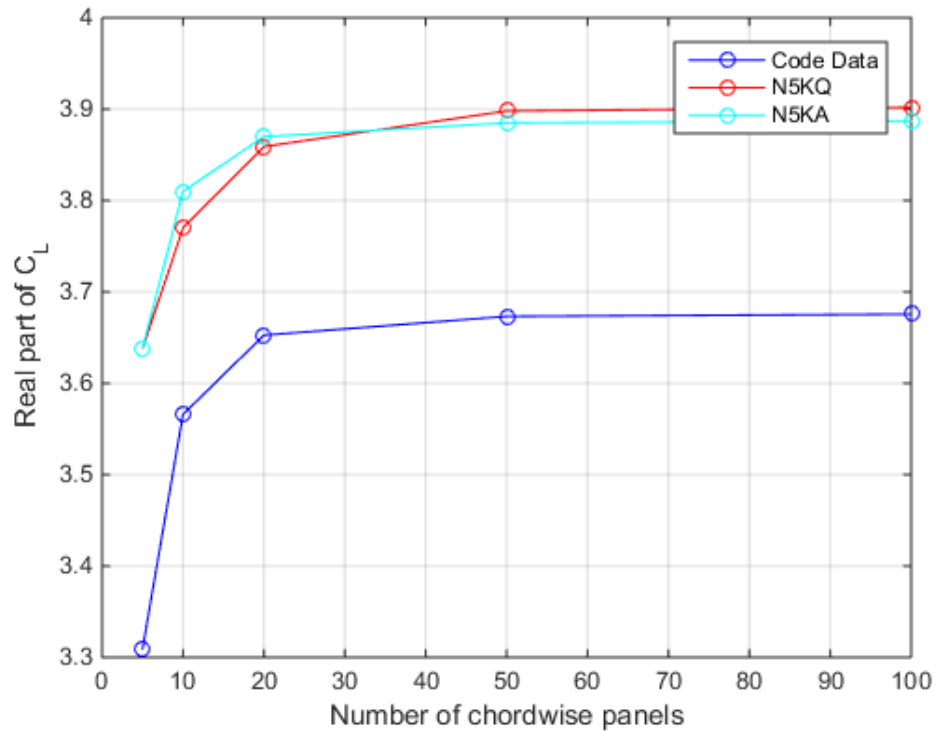


Figure 2.12 Comparison of C_L (real) for rectangular $AR = 2$ wing, $M = 0.8$, reduced frequency $k = 0.5$

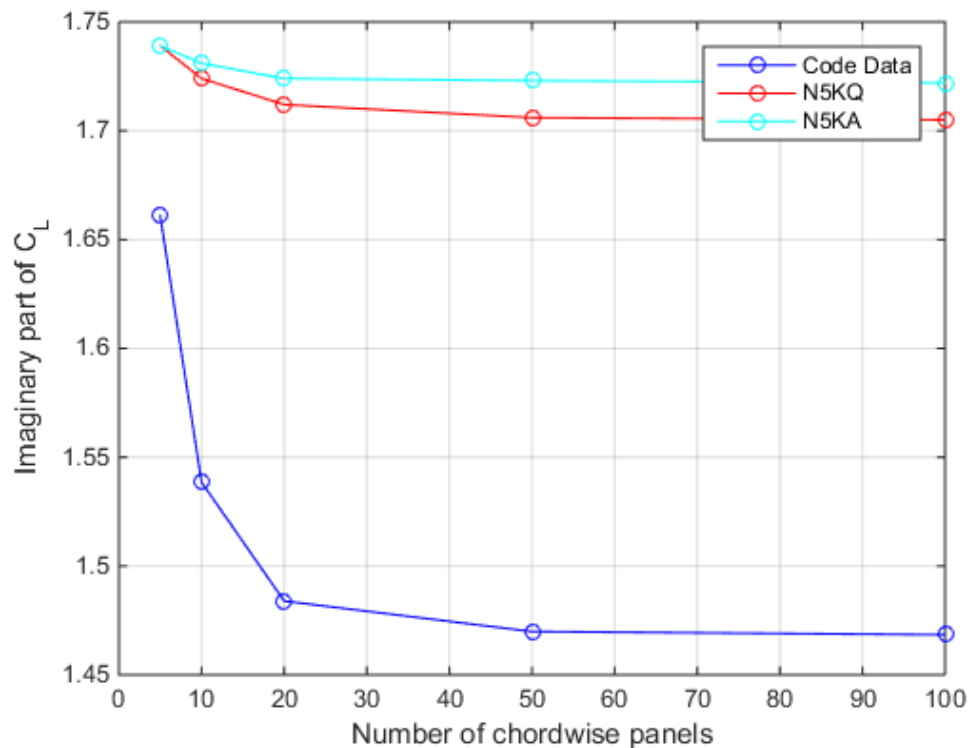


Figure 2.13 Comparison of C_L (imaginary) for rectangular $AR = 2$ wing, $M = 0.8$, reduced frequency $k = 0.5$

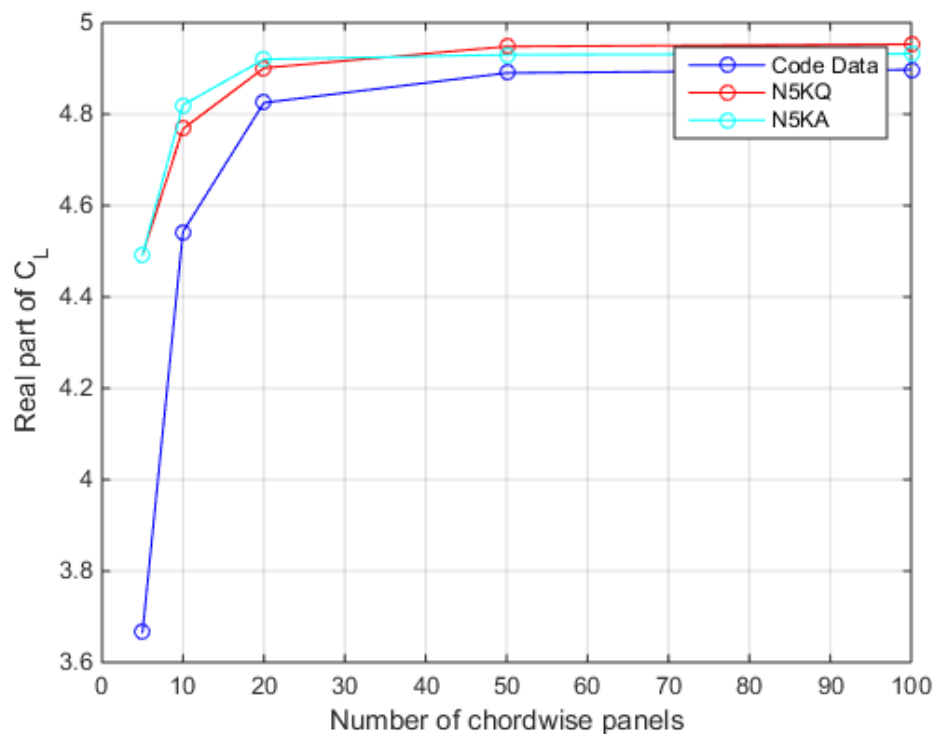


Figure 2.14 Comparison of C_L (real) for rectangular $AR = 2$ wing, $M = 0.8$, reduced frequency $k = 1.0$

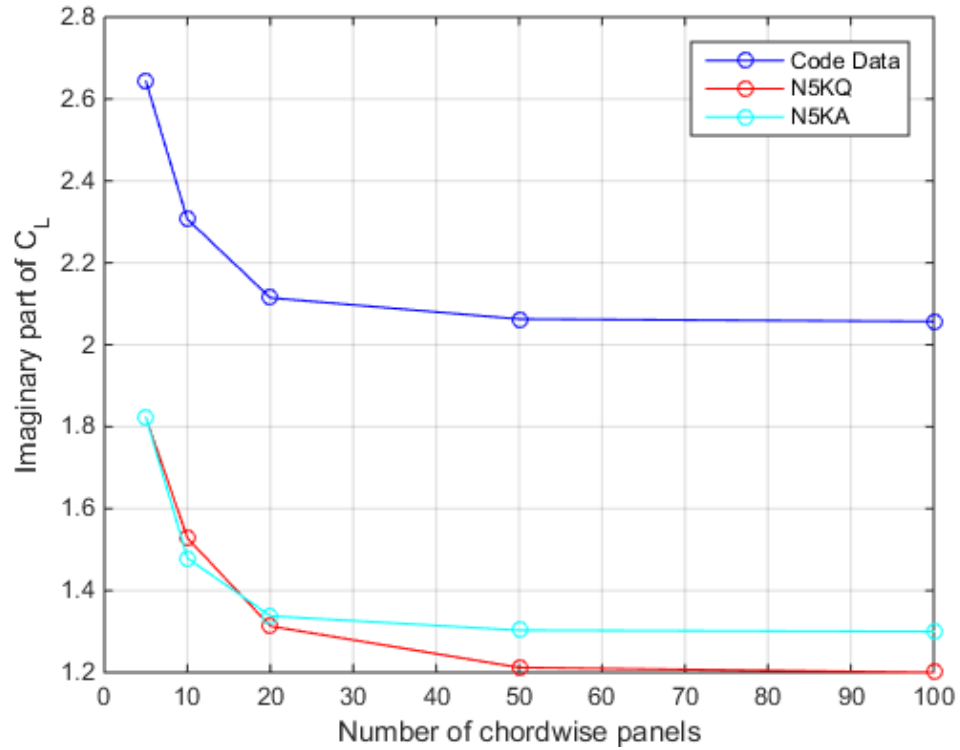


Figure 2.15 Comparison of C_L (imaginary) for rectangular $AR = 2$ wing, $M = 0.8$, reduced frequency $k = 1.0$

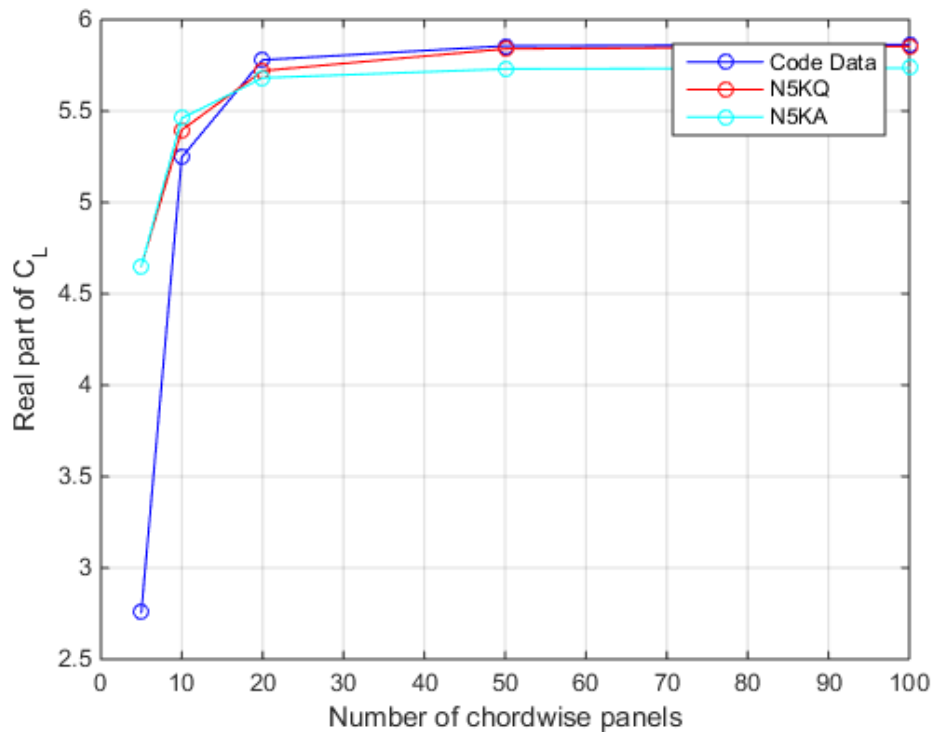


Figure 2.16 Comparison of C_L (real) for rectangular $AR = 2$ wing, $M = 0.8$, reduced frequency $k = 2.0$

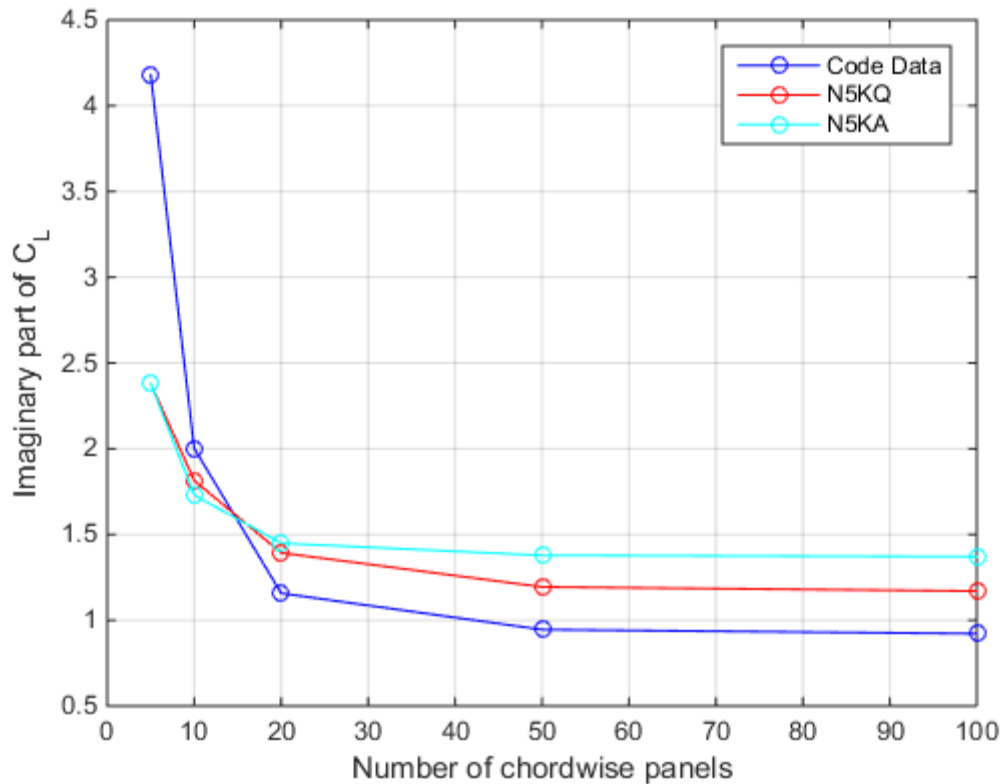


Figure 2.17 Comparison of C_L (imaginary) for rectangular $AR = 2$ wing, $M = 0.8$, reduced frequency $k = 2.0$

The results indicate that the custom DLM code is in good agreement with other developed codes, and its imaginary and real parts seem to converge for the same number of chord-wise panels, however, it should be noted that for high reduced frequencies starting from $k = 0.5$ the imaginary part is slightly off as it can be seen in *Figure 2.13*, *Figure 2.15* and *Figure 2.17*. Apart from that, the real part of the C_L almost matches the values of other DLM codes through the whole range of reduced frequencies as shown in *Figure 2.10*, *Figure 2.12*, *Figure 2.14* and *Figure 2.16*.

3. Structural Modeling

In order to describe the structure of the wing a Finite Element Method (FEM) is utilized. Since the aerodynamic model allows the panels to pitch and heave, triangular plate bending element is chosen so that the structural grid describing the lifting surface can translate and rotate as well to account for heave and pitch motion introduced by the aerodynamic modeling.

The FEM code developed for the Matlab Aeroelastic Code is based on several models presented in (Singiresu, 2017). Since triangular bending element is considered, there are 3 nodes per element, and each node has 3 DoF which sums to 9 DoF per element. The DoF of triangular bending element are shown in *Figure 3.1*.

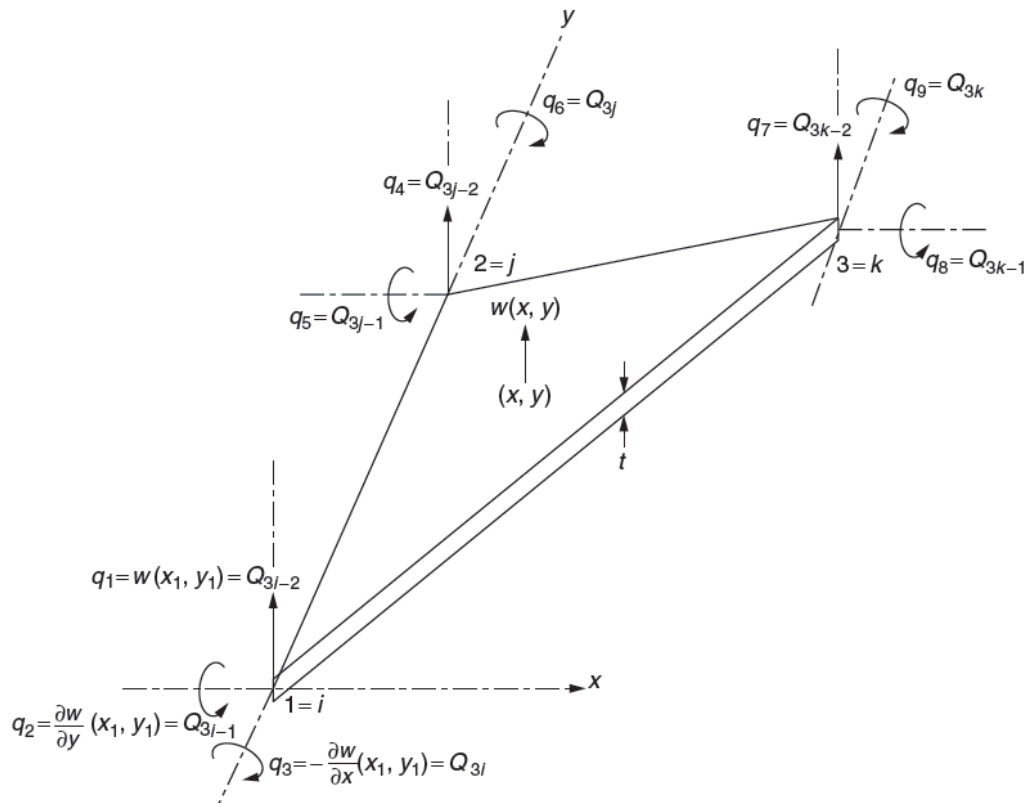


Figure 3.1 Nodal DoF of a triangular plate in bending (Singiresu, 2017)

In *Figure 3.1* a single element with 3 nodes is presented. Each node has 3 DoF:

q_1 , which is the vertical (transverse) translation in z , q_2 , which is the slope (rotation) in x and q_3 , which is the slope (rotation) in y . The magnitude of the translation of the first node is given by $w(x_1, y_1)$, similarly the rotation in x axis is given by $\frac{\partial w}{\partial y}(x_1, y_1)$ and the rotation in y is shown as $-\frac{\partial w}{\partial x}(x_1, y_1)$. The thickness of the plate is denoted by t .

Since, there are 9 displacement DoF per element, the assumed polynomial for the displacement function $w(x, y)$ should also contain nine constant terms (Singiresu, 2017). The chosen displacement model is the nonconforming element (T-9) (Tocher, 1962) and is given as:

$$w(x, y) = \alpha_1 + \alpha_2 x + \alpha_3 y + \alpha_4 x^2 + \alpha_5 xy + \alpha_6 y^2 + \alpha_7 x^3 + \alpha_8(x^2 y + xy^2) + \alpha_9 y^3 \quad (3.1)$$

$$w(x, y) = [\eta] \bar{\alpha} \quad (3.2)$$

$$[\eta] = [1 \quad x \quad y \quad x^2 \quad xy \quad y^2 \quad x^3 \quad (x^2 y + xy^2) \quad y^3] \quad (3.3)$$

$$\bar{\alpha} = \begin{bmatrix} \alpha_1 \\ \alpha_2 \\ \vdots \\ \alpha_9 \end{bmatrix} \quad (3.4)$$

The constants $\alpha_1, \alpha_2, \dots, \alpha_9$ from the vector $\bar{\alpha}$ are determined from the nodal conditions:

$$w(x, y) = q_1, \quad \frac{\partial w}{\partial y}(x, y) = q_2, \quad -\frac{\partial w}{\partial x}(x, y) = q_3 \quad \text{at } (x_1, y_1) = (0, 0) \quad (3.5)$$

$$w(x, y) = q_4, \quad \frac{\partial w}{\partial y}(x, y) = q_5, \quad -\frac{\partial w}{\partial x}(x, y) = q_6 \quad \text{at } (x_2, y_2) = (0, y_2) \quad (3.6)$$

$$w(x, y) = q_7, \quad \frac{\partial w}{\partial y}(x, y) = q_8, \quad -\frac{\partial w}{\partial x}(x, y) = q_9 \quad \text{at } (x_3, y_3) \quad (3.7)$$

Note that the local coordinates are chosen in such a way that the origin is placed at node 1, thus $(x_1, y_1) = (0, 0)$, the local y axis is the line connecting the nodes 1 and 2,

and the local x axis is pointing towards the node 3 which is demonstrated in *Figure 3.1*.

Single element's DoF can be put in matrix form as:

$$\bar{q} = \begin{bmatrix} q_1 \\ q_2 \\ \vdots \\ q_9 \end{bmatrix} = [\tilde{\eta}] \bar{\alpha} \quad (3.8)$$

where,

$$[\tilde{\eta}] = \begin{bmatrix} 1 & 0 & 0 & 0 & 0 & 0 & 0 & 0 & 0 \\ 0 & 0 & 1 & 0 & 0 & 0 & 0 & 0 & 0 \\ 0 & -1 & 0 & 0 & 0 & 0 & 0 & 0 & 0 \\ 1 & 0 & y_2 & 0 & 0 & y_2^2 & 0 & 0 & y_2^3 \\ 0 & 0 & 1 & 0 & 0 & 2y_2 & 0 & 0 & 3y_2^2 \\ 0 & -1 & 0 & 0 & -y_2 & 0 & 0 & -y_2^2 & 0 \\ 1 & x_3 & y_3 & x_3^2 & x_3 y_3 & y_3^2 & x_3^3 & (x_3^2 y_3 + x_3 y_3^2) & y_3^3 \\ 0 & 0 & 1 & 0 & x_3 & 2y_3 & 0 & (2x_3 y_3 + x_3^2) & 3y_3^2 \\ 0 & -1 & 0 & -2x_3 & -y_3 & 0 & -3x_3^2 & (-y_3^2 + 2x_3 y_3) & 0 \end{bmatrix} \quad (3.9)$$

Any point on the element experiences transverse w (in z -axis) and in-plane u (in x -axis) and v (in y -axis) displacements. Thus, the strain-displacement relations can be expressed as:

$$\varepsilon_{xx} = \frac{\partial u}{\partial x} = -z \frac{\partial^2 w}{\partial x^2} \quad (3.10)$$

$$\varepsilon_{yy} = \frac{\partial v}{\partial y} = -z \frac{\partial^2 w}{\partial y^2} \quad (3.11)$$

$$\varepsilon_{xy} = \frac{\partial u}{\partial y} + \frac{\partial v}{\partial x} = -2z \frac{\partial^2 w}{\partial x \partial y} \quad (3.12)$$

The strains can be expressed in matrix form as:

$$\bar{\varepsilon} = [\tilde{B}] \bar{\alpha} = [B] \bar{q} \quad (3.13)$$

where,

$$[\tilde{B}] = -z \begin{bmatrix} 0 & 0 & 0 & 2 & 0 & 0 & 6x & 2y & 0 \\ 0 & 0 & 0 & 0 & 0 & 2 & 0 & 2x & 6y \\ 0 & 0 & 0 & 0 & 2 & 0 & 0 & 4(x+y) & 0 \end{bmatrix} \quad (3.14)$$

$$[B] = [\tilde{B}][\tilde{\eta}]^{-1} \quad (3.15)$$

The element stiffness matrix in local coordinates can be expressed as:

$$[k^e] = \iiint_{V^e} [B]^T [D] [B] dV \quad (3.16)$$

where, V^e is the volume of the element and $[D]$ is the flexural rigidity matrix given by:

$$[D] = \frac{E}{(1-\nu^2)} \begin{bmatrix} 1 & \nu & 0 \\ \nu & 1 & 0 \\ 0 & 0 & \frac{1-\nu}{2} \end{bmatrix} \quad (3.17)$$

The transverse displacement is expressed as:

$$w(x, y) = ([\eta][\tilde{\eta}]^{-1})\bar{q} \quad (3.18)$$

The in-plane displacements are expressed as:

$$u = -z \cdot \frac{\partial w}{\partial x} \quad (3.19)$$

$$v = -z \cdot \frac{\partial w}{\partial y} \quad (3.20)$$

Combined translational displacements can be shown as:

$$\begin{Bmatrix} u(x, y) \\ v(x, y) \\ w(x, y) \end{Bmatrix} = \begin{bmatrix} -z \cdot \frac{\partial [\eta]}{\partial x} \\ -z \cdot \frac{\partial [\eta]}{\partial y} \\ [\eta] \end{bmatrix} [\tilde{\eta}]^{-1} \bar{q} = [N_1][\tilde{\eta}]^{-1} \bar{q} = [N] \bar{q} \quad (3.21)$$

$[N_1]$

$$= \begin{bmatrix} 0 & -z & 0 & -2xz & -yz & 0 & -3x^2z & -z(y^2 + 2xy) & 0 \\ 0 & 0 & -z & 0 & -xz & -2yz & 0 & -z(2xy + x^2) & -3y^2z \\ 1 & x & y & x^2 & xy & y^2 & x^3 & (x^2y + xy^2) & y^3 \end{bmatrix} \quad (3.22)$$

The consistent mass matrix can be evaluated as:

$$[m^e] = \iiint_{V^e} \rho [N]^T [N] dV \quad (3.23)$$

$$= \iiint_{V^e} \rho ([\tilde{\eta}]^{-1})^T [N_1]^T [N_1] [\tilde{\eta}]^{-1} dV \quad (3.24)$$

3.1 FEM Validation

The developed FEM is validated with the results provided by (Clough, 1965). The setup is shown in *Figure 3.2*.

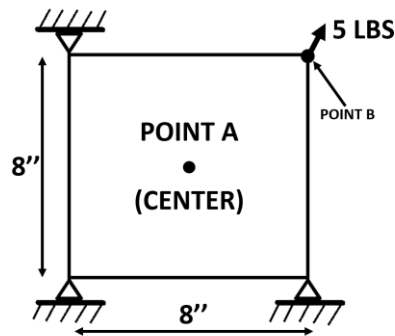


Figure 3.2 Square plate schematic

The square plate is simply supported at three corners and subjected to a vertical load at the fourth corner as shown in *Figure 3.2*. The plate is square with a side of 8 inches and its thickness t is 1 inch, the elastic modulus E is $10,000 \text{ lbs/in}^2$ and Poisson's ratio is 0.3. Transverse load is applied on Point B and its magnitude is 5 *lbs*. Displacements at Point A (center) and Point B are recorded.

The FEA was also carried out in Nastran so that the results of the FEM code can be verified with the output of Nastran. The analysis was performed with different mesh sizes with increasing numbers of elements per side from $N_e = 4$ to $N_e = 24$.

Table 3.1 demonstrates the displacements of point A and point B shown in *Figure 3.2*. The "Experiment" column in Table 3.1 depicts the displacements of point A and B

obtained experimentally by (Clough, 1965). It is important to mention that structural grids generated in Nastran are identical to the ones generated in the Matlab FEM code. The “Nastran” and “Matlab” columns in Table 3.1 show the displacements of nodes corresponding to the central point A and corner point B shown in *Figure 3.2* generated using Nastran code and Matlab code respectively.

Table 3.1

Displacements of point A and B

Mesh Size	Point	Nastran	Matlab	Experiment
N = 4	A	0.06912453	0.0672	0.0624
	B	0.2764981	0.2690	0.24960
N = 8	A	0.07034770	0.0646	0.0624
	B	0.2813908	0.2583	0.24960
N = 12	A	0.07165316	0.0638	0.0624
	B	0.2866126	0.2551	0.24960
N = 16	A	0.07259741	0.0634	0.0624
	B	0.2903896	0.2536	0.24960
N = 20	A	0.07326044	0.0632	0.0624
	B	0.2930418	0.2528	0.24960
N = 24	A	0.07373901	0.0631	0.0624
	B	0.2949560	0.2522	0.24960

Figure 3.3 and Figure 3.4 show the data in Table 3.1 as the mesh size is varied from $N_e = 4$ to $N_e = 24$.

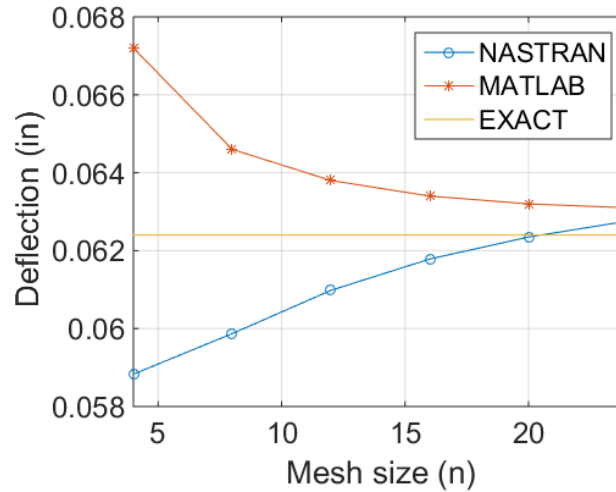


Figure 3.3 Deflection of Point A (center)

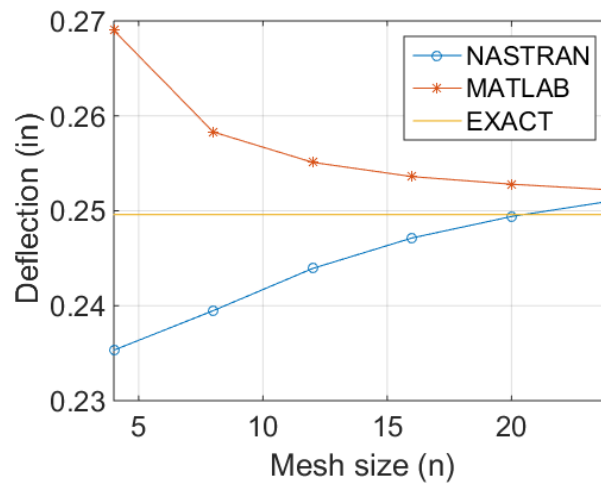


Figure 3.4 Deflection of Point B (corner)

It can be observed from Figure 3.3 and Figure 3.4 that the Matlab code's result is converging very close to the experimental value similarly to the Nastran's output which is converging to a value slightly closer to the experimental value for the same number of elements per side.

4. Grid Interpolation

As it was discussed in section 2.2, the DLM provides the aerodynamic force distribution on an aerodynamic grid describing a lifting surface at a given frequency and for a given normalwash distribution. However, in order to obtain the normalwash distribution corresponding to a lifting surface's elastic deformation the aerodynamic model should interact with the structural model. Moreover, the effect of aerodynamic forces on the structural grids should be computed as well.

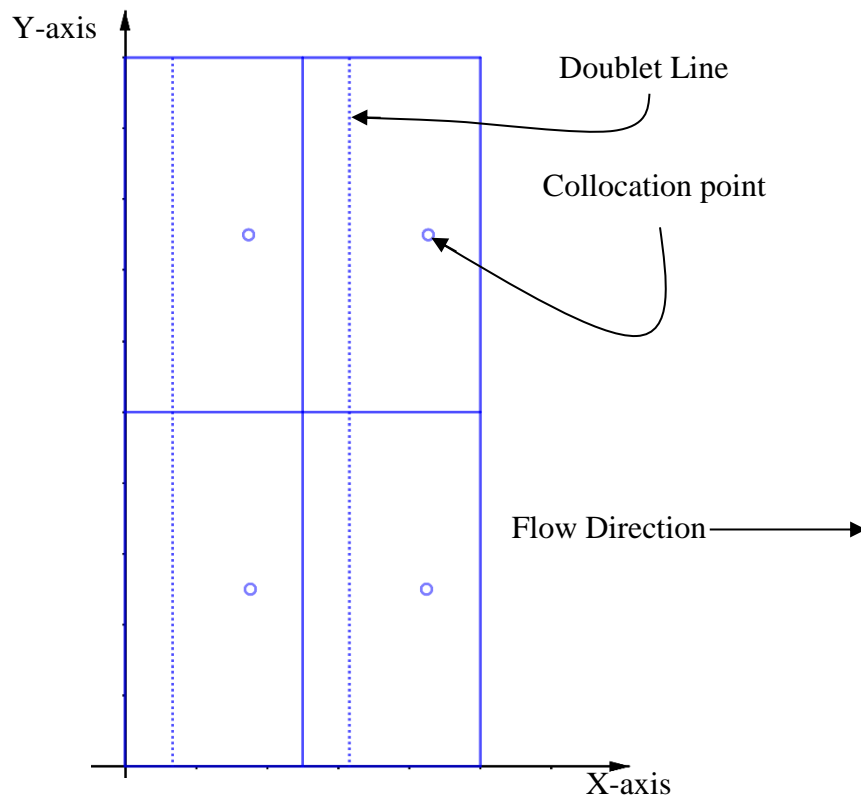


Figure 4.1 Example of 2x2 aerodynamic grid

Figure 4.1 demonstrates an aerodynamic grid with collocation points (shown as blue circles) and doublet lines (shown as dashed blue lines) that has 4 panels in total. Panel boundaries are represented as solid blue lines. The flow direction is also shown in *Figure 4.1*. The next step is to superimpose FEM on the aerodynamic grid which is

demonstrated in *Figure 4.2*. It should be noted that the selected FEM has triangular elements, and in this demonstration every aerodynamic grid's element has corresponding 4 triangular bending elements (boundaries of FEM are shown in black dashed lines) which can be seen in *Figure 4.2*. Black dots represent structural grid's nodes.

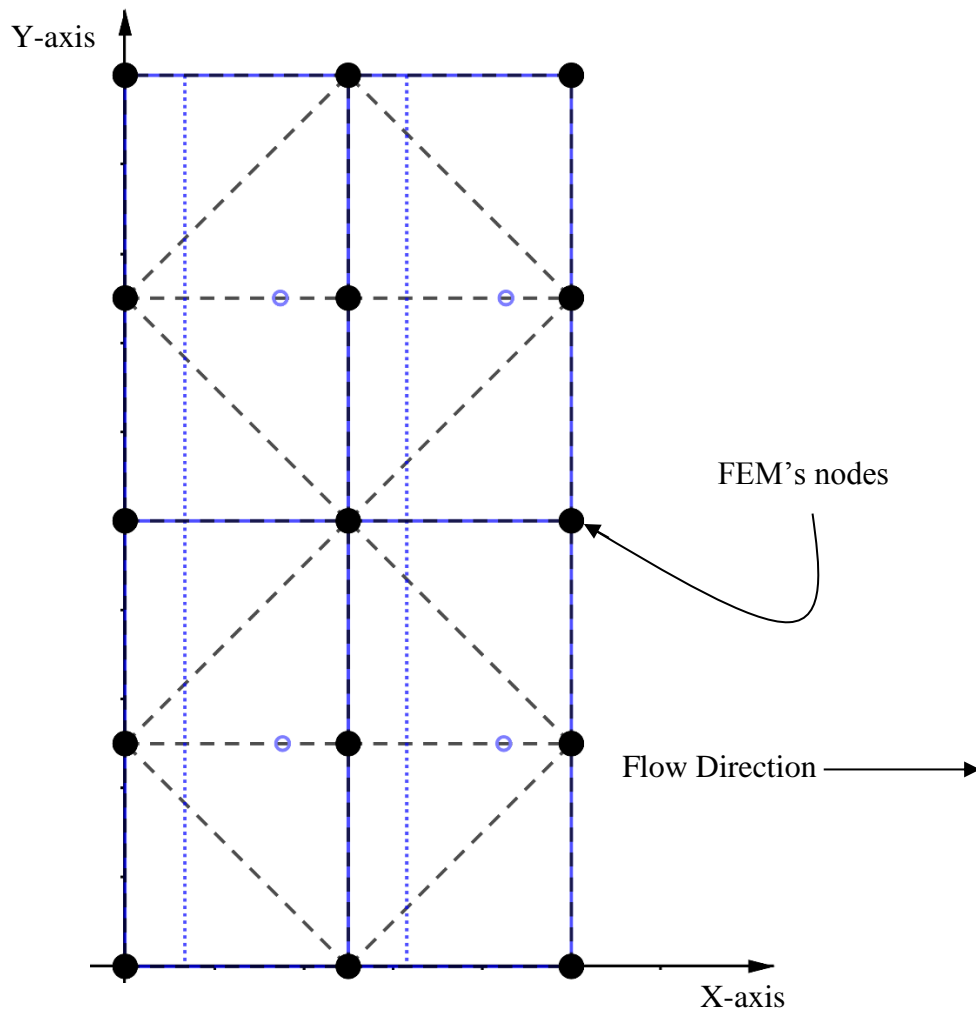


Figure 4.2 FEM superimposed on 2x2 aerodynamic grid

FEM grid superimposed on aerodynamic grid can be observed in *Figure 4.2*. The FEM elements are triangular and their boundaries are shown in black dashed lines, the nodes of the structural grid are presented as black solid circles. As it was mentioned back in Chapter 3, the structural elements are triangular bending elements which have 3 DoF per node, which means that there are 9 DoF per structural element. The aerodynamic

grid, however, has 2 DoF per panel (element): pitch about centerline parallel to the y-axis and heave. Since the FEM was validated in section 3.1 the next step is to interconnect the aerodynamic grid with structural grid so that structural DoF are projected to the aerodynamic grid and the normalwash vector can be computed for a given elastic deformation. This is achieved by using grid interpolation technique that can relay information from FE grid to the aerodynamic grid and vice-versa. Generally, the elastic deformation provided by the FE grid is relayed to the aerodynamic grid so that the normalwash vector is computed. In the other direction, the aerodynamics forces are transmitted to the structural grid using the same grid interpolation. Considering linear interpolation, this can be described by the following transformation matrices:

$$u_{aero} = T_{as}u_{struc} \quad (4.1)$$

$$F_{struc} = T_{sa}\mathcal{F}_{aero} \quad (4.2)$$

where, u_{aero} is aerodynamic panels' DoF, u_{struc} is the structural nodes' DoF, F_{struc} is the force applied on the structural grid, \mathcal{F}_{aero} is the force acting on the aerodynamic grid, T_{as} is the transformation matrix that gives aerodynamic panels' DoF displacements or forces given structural grid's displacement or forces, T_{sa} is the opposite transformation matrix (Kotikalpudi, 2017). It is important to note that the \mathcal{F}_{aero} is a vector that consists of lift and pitching moments of each panel about their midpoints, and it can be expressed as:

$$\mathcal{F}_{aero}^i = \begin{bmatrix} F_i \\ M_i \end{bmatrix} = \begin{bmatrix} 1 \\ c_i \\ 4 \end{bmatrix} F_{aero}^i = T_{\mathcal{F}}^i F_{aero}^i \quad (4.3)$$

where, \mathcal{F}_{aero}^i vector consisting of force acting on i^{th} panel's midpoint and moment about its midpoint, whereas F_{aero}^i is the force acting on i^{th} panel' quarter-chord (Kotikalpudi,

2017). The transformation matrix $T_{\mathcal{F}}$ can be constructed in diagonal manner to account for all panels.

Also, the transformation matrices are transpose of one another:

$$T_{as} = T_{sa}^T \quad (4.4)$$

This is true because the interpolation of aerodynamic forces on to the structural grid requires structural equivalence, which implies that the load vectors F_{struct} and \mathcal{F}_{aero} deform the structure identically (Rodden 1959; Rodden & Johnson, 1994). From structural equivalence, it can be shown that:

$$\delta u_{struct}^T F_{struct} = \delta u_{aero}^T \mathcal{F}_{aero} \quad (4.5)$$

and,

$$\delta u_{aero} = T_{as} \delta u_{struct} \quad (4.6)$$

$$\delta u_{aero}^T = \delta u_{struct}^T T_{as}^T \quad (4.7)$$

thus,

$$\delta u_{struct}^T [F_{struct} - T_{as}^T \mathcal{F}_{aero}] = 0 \quad (4.8)$$

$$F_{struct} = T_{as}^T \mathcal{F}_{aero} \quad (4.9)$$

It can be seen that the T_{as}^T actually equals to T_{sa} as shown. Thus, it is required to find transformation in one direction only (Kotikalpudi, 2017).

In order to obtain such transformation surface spline theory for thin surfaces is utilized. The surface splines used in this thesis are based on the work of (Harder & Desmarais, 1972). This method is a mathematical tool that interpolates between grids using infinite thin plate deformation equations. However, this is a two-step process since firstly the structural deformations have to be represented as deformations on infinite thin plate and secondly using the surface spline method these deformations are interpolated to

match with aerodynamic panels' DoF. Similar technique is used in Nastran which is discussed in detail in (Rodden & Johnson, 1994).

An infinite thin plate has only 1 DoF since it can only deform in the direction normal to its surface (Kotikalpudi, 2017). Thus, it is required to represent the deformation of structural grid that has 3 DoF per node purely as 1 DoF heave deformations. This is done by constructing spline grid. *Figure 4.3* demonstrates the spline grid superimposed on FE grid and aerodynamic grid. The nodes of spline grid are shown as red solid circles, and its boundaries that match with FE grid's boundaries are shown in red dashed lines and solid red line show additional nodes that are added to each structural grid's node.

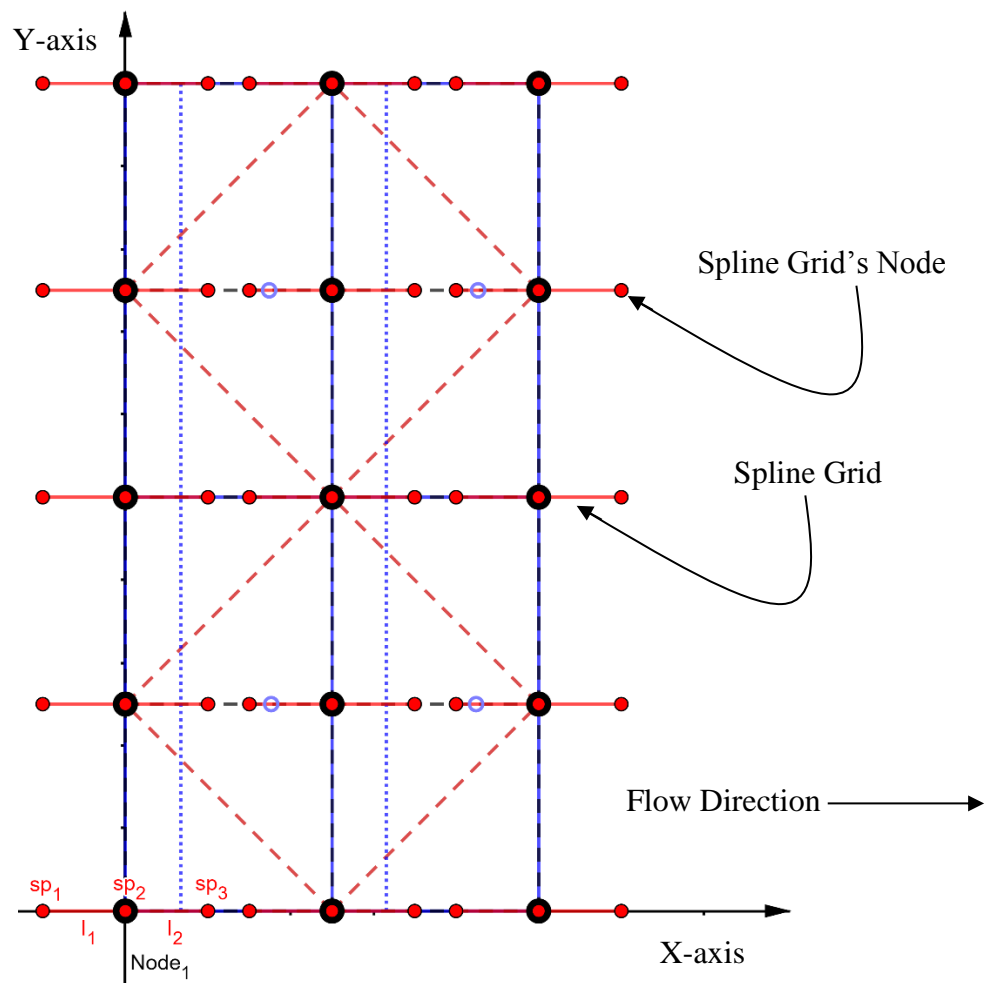


Figure 4.3 Spline grid

The DoF of $Node_1$ shown in *Figure 4.3* can be represented as heave motion of spline nodes attached to the structural grid's $Node_1$:

$$\begin{bmatrix} h_{sp_1} \\ h_{sp_2} \\ h_{sp_3} \end{bmatrix} = \begin{bmatrix} 1 & 0 & l_1 \\ 1 & 0 & 0 \\ 1 & 0 & -l_2 \end{bmatrix} \begin{bmatrix} h_{Node_1} \\ \theta_{Node_1} \\ \beta_{Node_1} \end{bmatrix} \quad (4.10)$$

where h_{sp_i} is the heave displacement of spline grid's i^{th} node, l_1 is the distance between sp_1 grid and sp_2 grid, l_2 is the distance between sp_2 grid and sp_3 grid, h_{Node_1} is the heave displacement (z-axis translation) of $Node_1$, θ_{Node_1} is the bending (rotation about x-axis) of $Node_1$, β_{Node_1} is the twist (rotation in y-axis) of $Node_1$. The total transformation matrix between structural grid and spline grid is formed by obtaining spline grid's DoF for each node of structural grid, so that it can be expressed as:

$$u_{spline} = T_{spline} u_{struc} \quad (4.11)$$

where u_{spline} contains the deformations of spline grid which consists of purely heave motion. After the deformation of spline grid is obtained the deformations at the locations of aerodynamic panel midpoints can be found using the infinite surface spline theory (Kotikalpudi, 2017). This interpolation between spline grid and aerodynamic grid can be expressed as T_{ips} , so that the interpolation between structural grid and aerodynamic grid can be expressed as:

$$T_{as} = [T_{ips}][T_{spline}] \quad (4.12)$$

The detailed derivation of T_{ips} matrix is shown in (Rodden & Johnson, 1994; Harder & Desmarais, 1972). It is important to note that this approach is general in a way that it allows having independent structural and aerodynamic grids.

5. Analysis of the F-5 wing

The F-5 wing was analyzed in Nastran environment and the analysis included modal, flutter and static. Moreover, a static experiment and GVT was conducted to validate the FE model of the wing. The flutter analysis was performed in Nastran/Patran environment. Patran was used as a graphical user interface to setup the analysis by specifying the geometry, mesh, properties of material, loads, boundary conditions and flight condition. Since, the flutter analysis is of interest aeroleastic module built-in within Nastran was used.

As it was mentioned in introductory section 1, a specific wing geometry was chosen for aeroelastic analysis which is Northrop Grumman's F-5 fighter wing. The FE model of the wing was provided by the Embry-Riddle Aeronautical University's (ERAU) Structural Analysis and Design (SAnD) Lab (Tamijani et al., 2018; Locatelli et al., 2013). General characteristics of the wing are listed in Table 1.1. The rendering of the wing geometry is presented in *Figure 5.1*.

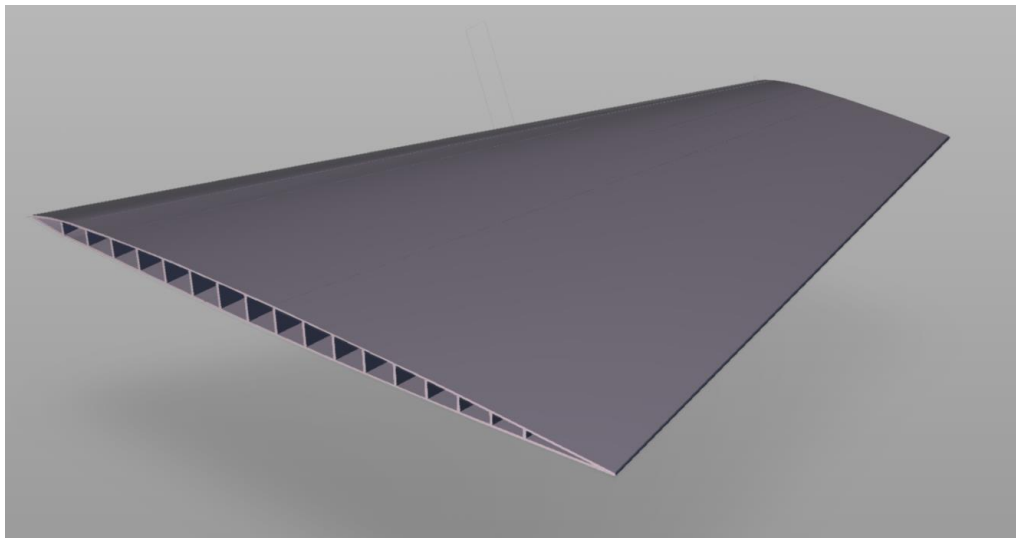


Figure 5.1 Rendering of the F-5 wing

The internal structure of the wing is topologically optimized which is demonstrated

in *Figure 5.2* and *Figure 5.3*.

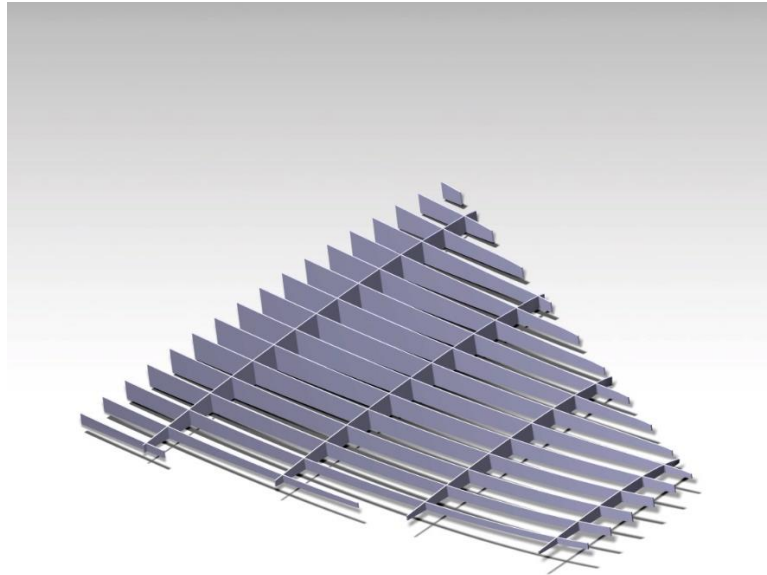


Figure 5.2 Wing internal structure (rib-spar geometry)

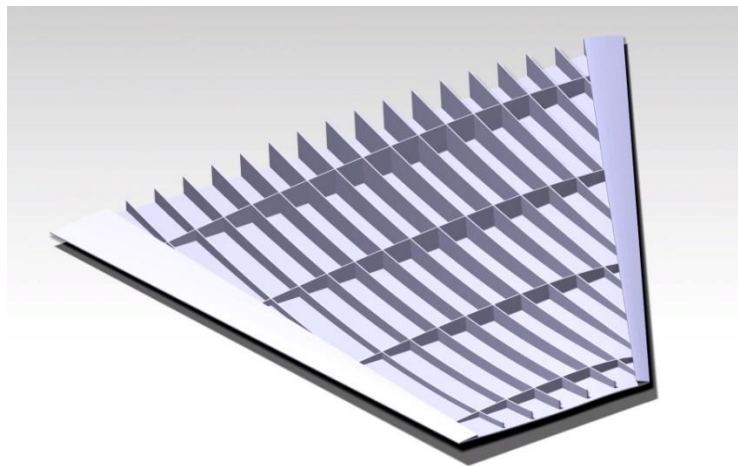


Figure 5.3 Wing box with hidden top surface

5.1 Static experiment of 3D printed wing prototype

Prior to flutter analysis, a static experiment was carried out in “Structures” lab at ERAU to validate the FE model made in Nastran. A small version of the wing was 3D printed in ERAU 3D printing workshop using “Makerbot Replicator 2X” 3D printer

(MakerBot Industries, New York, USA). Important issue that was considered prior to the experiment was the mechanical properties of the printing material. Since the wing has complex internal structure (*Figure 5.2, Figure 5.3*) and it was planned to analyze the displacement of the wing structure under static load, it was required that the printing material and the final structure had uniform modulus of elasticity. In other words, it was desired that the printing material had the same modulus of elasticity throughout the whole structure. Another issue was that there are enclosed spaces between spars, ribs, top and bottom surface as shown in *Figure 5.3*, so that if support material was used it would have been trapped within the enclosures changing the properties of the final printed structure. Furthermore, because of the same reason it would have been challenging to remove the support material from those enclosures once the manufacture is complete. Thus, it was decided that the structure of the wing is manufactured vertically and without support material. Dimensions of the manufactured wing was limited by the dimensions of “Makerbot Replicator 2X” 3D printer which is 24.6 cm x 16.3 cm x 15.5 cm (MakerBot Industries, 2018). As the wing was manufactured vertically, and, geometrically, the half-span of the wing is the largest dimension of the model it was decided to use the maximum allowable vertical print dimension of the “Makerbot Replicator 2X” 3D printer that resulted in the actual span-wise dimension of the wing to be 153 mm as shown in *Figure 5.4*.

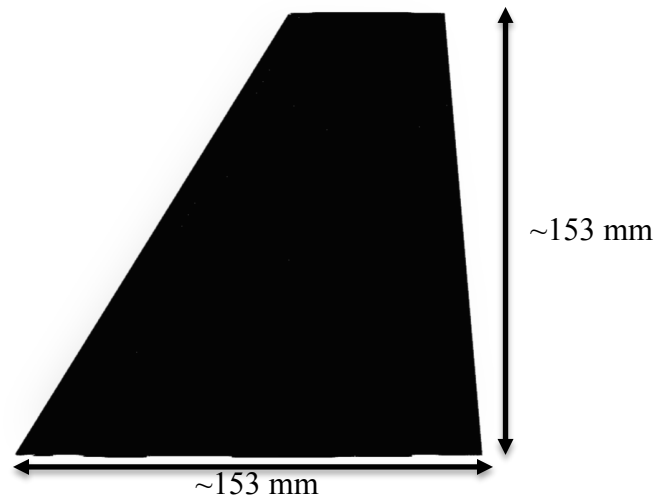


Figure 5.4 Top view with dimensions of the 3D printed wing

The material was chosen from the list of offered materials provided by ERAU 3D printing workshop. The wing was printed from “HATCHBOX” Acrylonitrile Butadiene Styrene (ABS) 3D printer filament with elastic modulus of $E = 1.8 \text{ GPa}$. For the static analysis the wing was fixed along the root chord as can be seen in *Figure 5.5* and the load was applied at the center of the tip chord. The same boundary conditions were equally applied to the FE model shown in *Figure 5.6*.



Figure 5.5 3D printed F-5 wing fixture

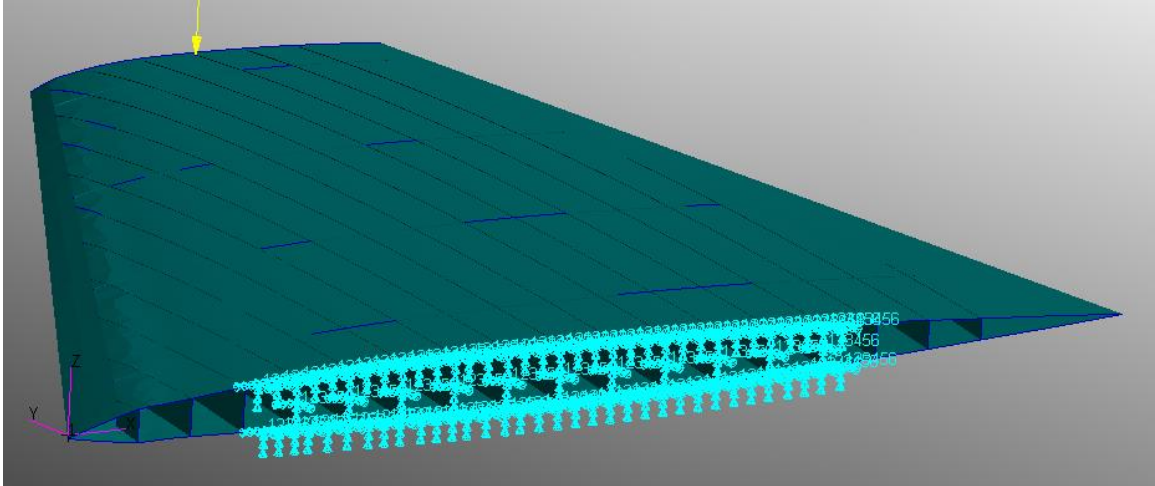


Figure 5.6 FE model's boundary conditions

Loads were applied on the 3D printed wing so that the wing itself was not damaged. This was achieved by adhering double-coated foam squares on the lower surface of the wing and gluing “L” shaped aluminum extrusion to the foam square using cyanoacrylate based glue. The load was varied by adding weights to a plastic bag that was mounted on the “L” extrusion as shown in *Figure 5.5*.

The displacement of the tip chord trailing edge point was recorded for varying loads for both the experiment and simulation in Nastran and the data is presented in Table 5.1.

Table 5.1

Displacement of tip chord trailing edge point

Load (g)	Displacement (mm)	
	Experiment	Nastran
200	2	1.52
300	3.5	2.28
400	4.2	3.05
900	6.8	6.848

Load (g)	Displacement (mm)	
	Experiment	Nastran
1000	7.7	7.61
1300	9	9.93
1500	10.5	11.45
1800	13.2	13.738
2000	15.5	15.22

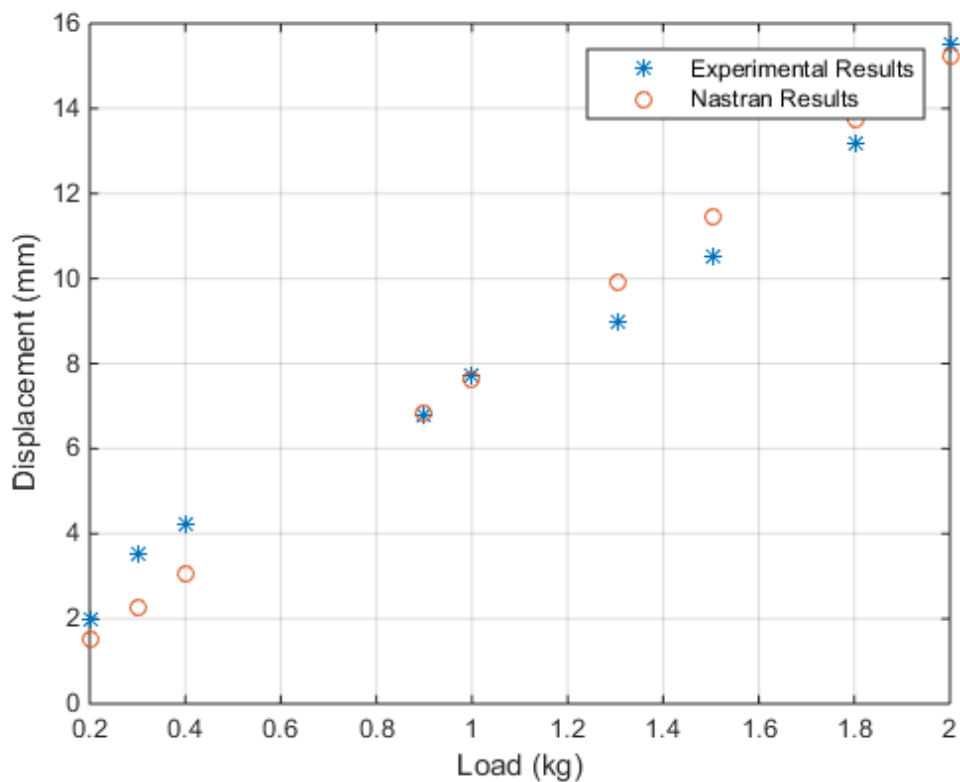


Figure 5.7 Displacement of tip chord trailing edge point as a function of load

Experimental results of the static experiment and the results of Nastran are in good agreement as demonstrated in *Figure 5.7*, thus, bolstering the confidence in further aeroelastic analysis within the Nastran's aeroelastic module.

5.2 Static test of 3D printed wing using DIC

A different static experiment utilizing DIC as the data acquisition tool was performed. The specimen in this case was the same 3D printed wing that was used for a static experiment described in section 5.2. However, this time DIC was used to obtain the map of z-axis displacements of the upper surface of the 3D printed wing.

The VIC-3D system based on the principle of Digital Image Correlation was used to measure the displacement. The VIC-3D system requires an applied random speckle pattern on a specimen and a calibration procedure since two cameras are used to capture 3-Dimensional measurements of displacements.

Since the 3D printed wing was printed from black ABS plastic a white spray paint was applied on the top surface of the wing as it is shown in *Figure 5.8*. The cameras were positioned vertically pointing downwards as it is demonstrated in *Figure 5.8* and at a proper distance so that cameras' resolution is fully utilized.

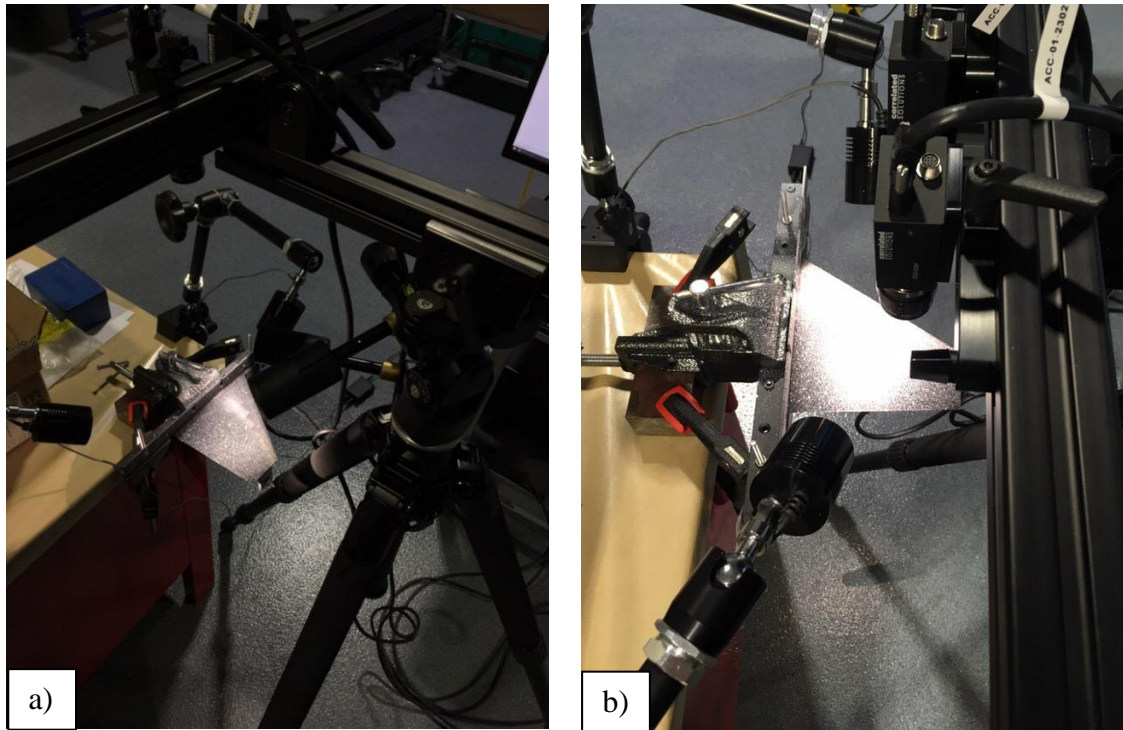


Figure 5.8 Static test, DIC setup with (a) a speckle pattern and (b) position of cameras

The load was applied and varied similarly as in section 5.2 by means of adding weights to a plastic bag that was mounted on the “L” extrusion as shown in *Figure 5.5*.

Table 5.2

Static tests performed with VIC-3D

Test Number	Load (g)	Maximum displacement in z-axis (mm)		Absolute Error (mm)
		VIC-3D	Nastran	
1	0	0	0	0
2	100	0.525	0.76	0.235
3	150	0.83	1.14	0.31
4	200	1.105	1.52	0.415
5	250	1.38	1.9	0.52

Test Number	Load (g)	Maximum displacement in z-axis (mm)		Absolute Error (mm)
		VIC-3D	Nastran	
6	300	1.68	2.28	0.6
7	350	1.97	2.66	0.69
8	400	2.25	3.04	0.79
9	450	2.54	3.42	0.88
10	500	2.82	3.8	0.98
11	550	3.12	4.18	1.06
12	600	3.4	4.56	1.16
13	650	3.74	4.94	1.2
14	700	4	5.32	1.32
15	750	4.3	5.7	1.4
16	800	4.58	6.08	1.5
17	850	4.86	6.46	1.6
18	900	5.25	6.84	1.59
19	950	5.5	7.22	1.72
20	1000	5.8	7.6	1.8

As it is shown in Table 5.2 several tests were carried out with loads varying from 100 to 1000 grams and for all test cases the Nastran simulation result showed slightly larger value of deformation. It can be noticed that the first test has a load of zero grams and the reason why first test's load is zero grams is that the consequent tests with nonzero

loads are compared to the first no-load case that acts as a reference so that z-axis displacements are obtained rather than z-axis position map of the top surface. The first no-load case is demonstrated in *Figure 5.9*. It can be observed that the whole surface is colored in green which demonstrates that this test is the reference no-load case with zero z-axis displacements.

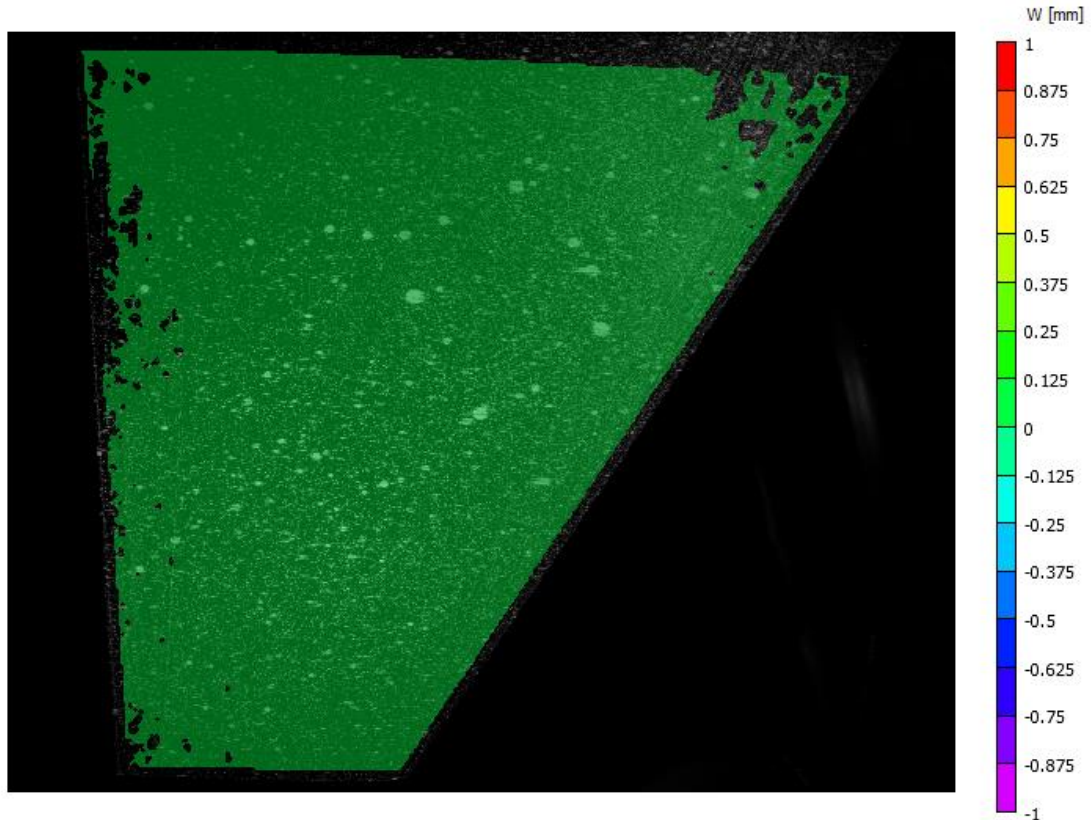


Figure 5.9 DIC test 1, no-load

The results obtained using VIC-3D were compared to Nastran simulation and are in *Figure 5.10* through *Figure 5.13* below for several load cases.

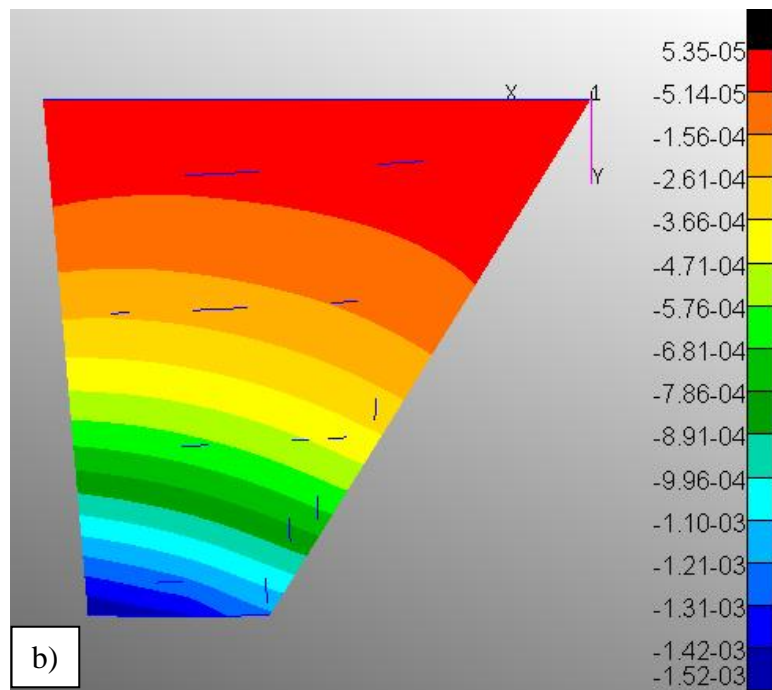
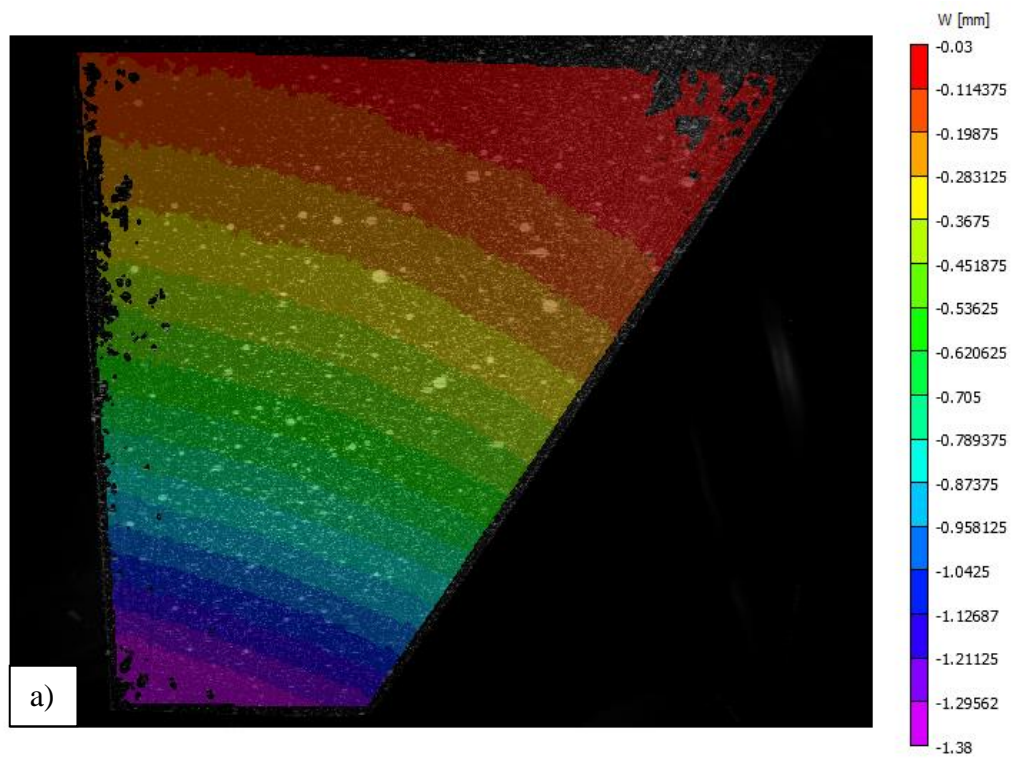


Figure 5.10 250-gram load case with (a) VIC-3D results and (b) Nastran results

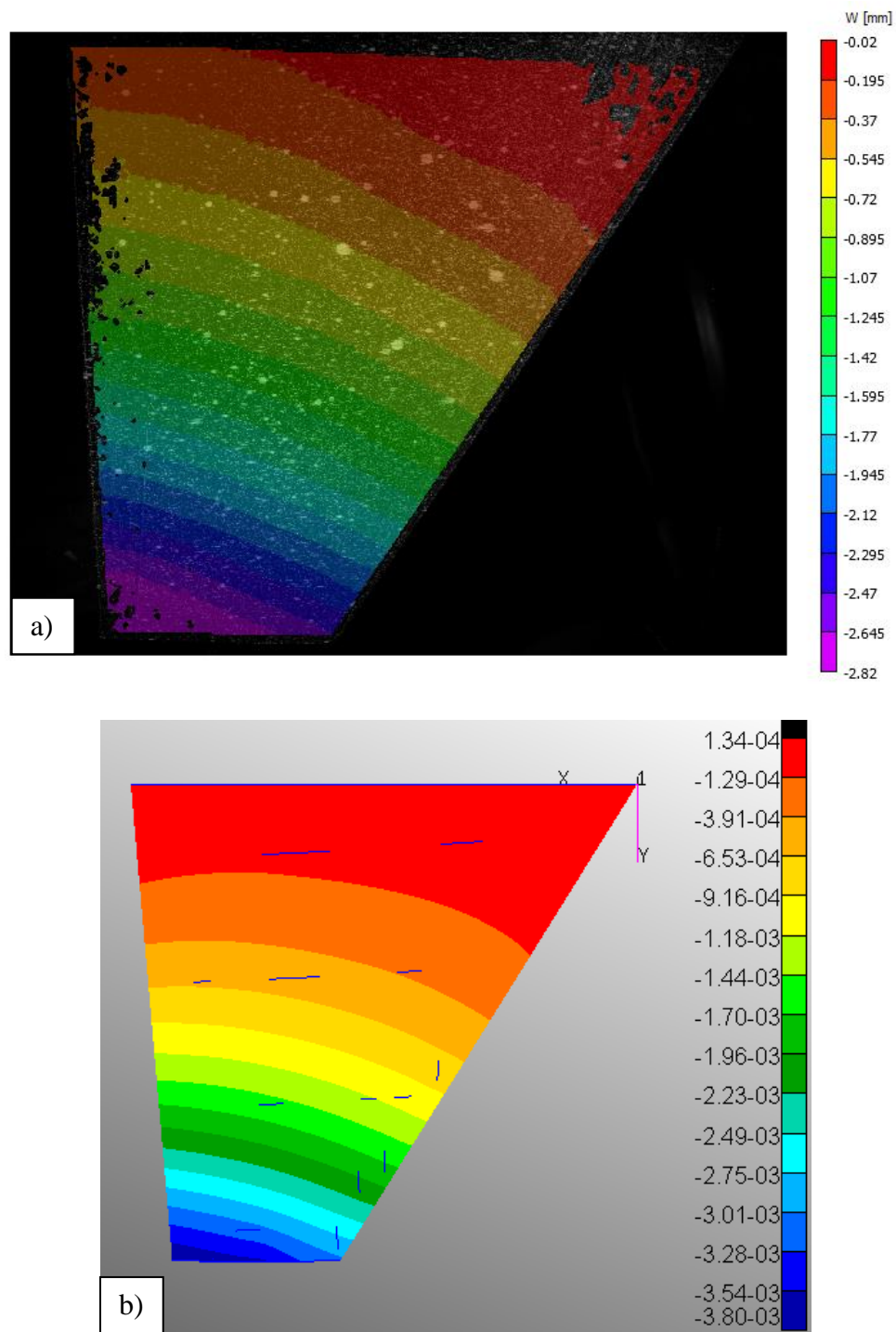


Figure 5.11 500-gram load case with (a) VIC-3D results and (b) Nastran results

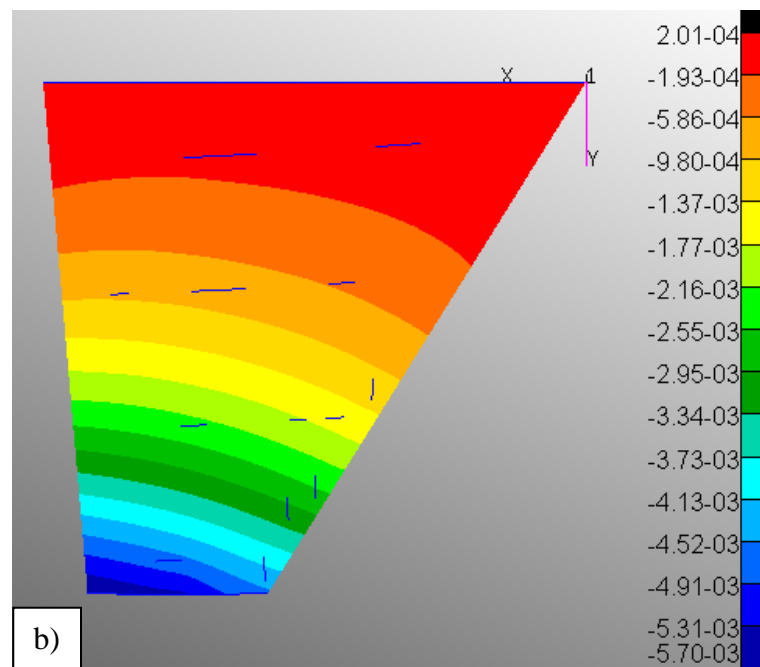
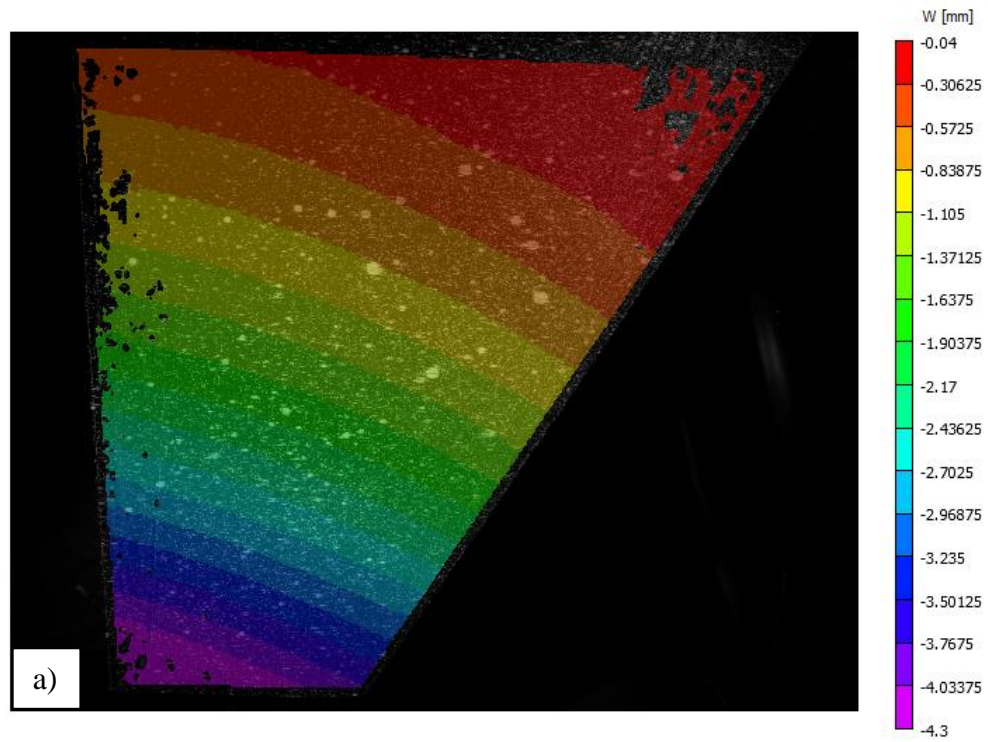


Figure 5.12 750-gram load case with (a) VIC-3D results and (b) Nastran results

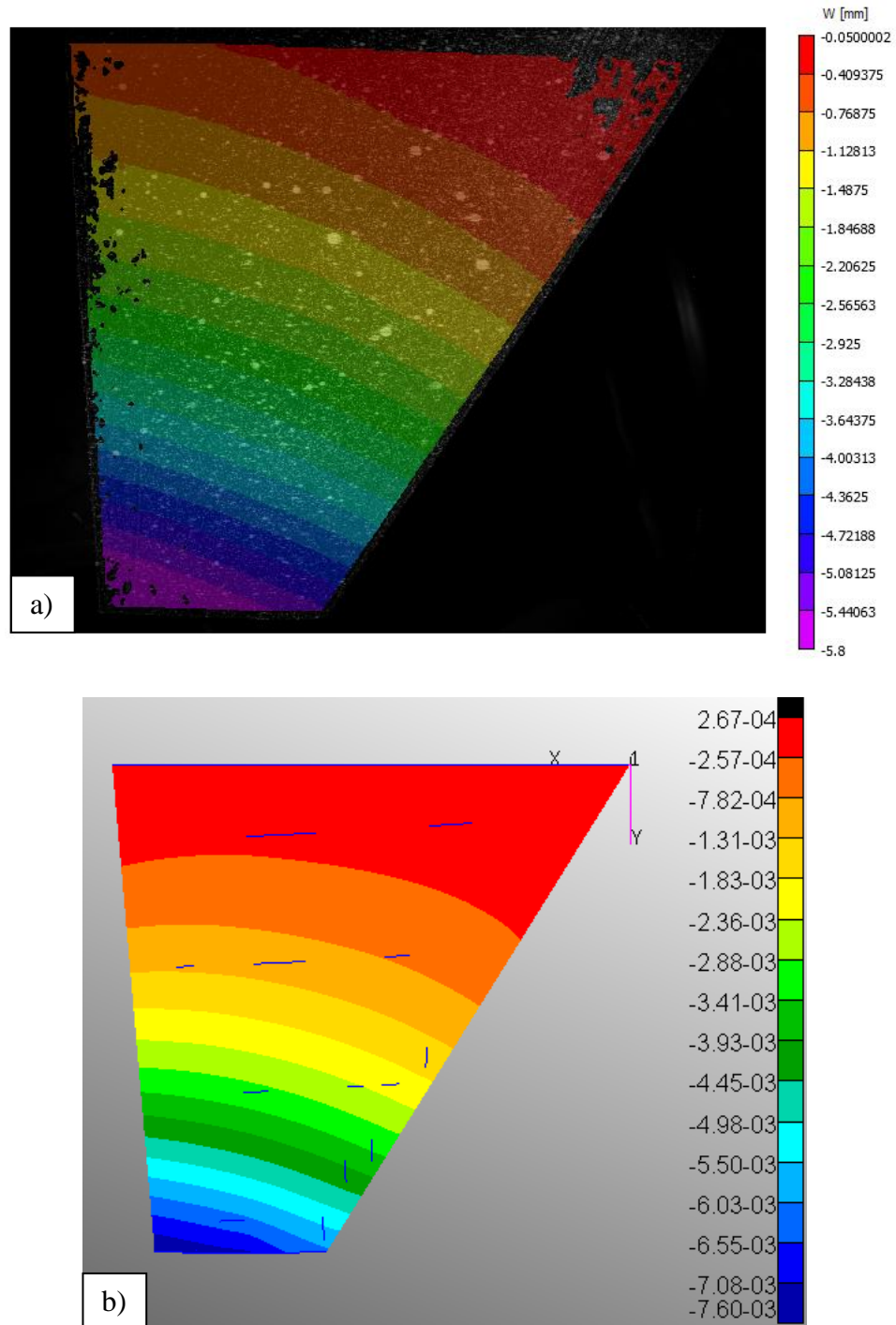


Figure 5.13 1000-gram load case with (a) VIC-3D results and (b) Nastran results

The comparison between FEM and experiment indicates that the Nastran slightly overestimates the z-axis displacement for every load case as it is demonstrated in a summarized data plot given in Figure 5.14. Nevertheless, the displacement patterns look

similar with some differences in the area close to the fixed root chord, which could be attributed to the fact that Nastran uses linear approximation for the displacements.

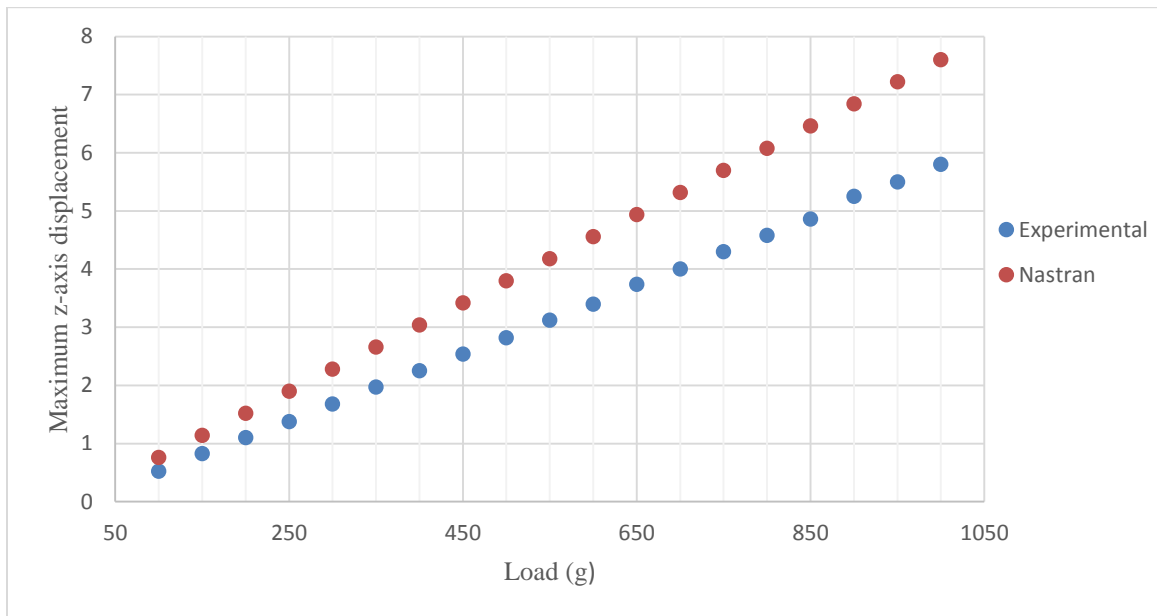


Figure 5.14 Maximum z-axis displacement as a function of load

The discrepancy between the slopes of FEM and experiment shown in *Figure 5.14* is attributed to the fact that in Nastran simulations a certain value of elastic modulus was used (1.8 GPa). However, the elastic modulus of the 3D printed part can be affected by the manufacturing conditions.

5.3 Ground Vibration Test of the 3D printed wing

In addition to the static test a GVT test was carried out with the 3D printed wing. The test was conducted using dynamic shaker Modal Exciter 2060E which can apply forces up to 267 N at frequencies between 1-6000 Hz.

For the purpose of this test a modified wing with a flange demonstrated in *Figure 5.15* was 3D printed so that a more accurate fixed root boundary condition can be achieved.



Figure 5.15 3D printed wing with a flange

The wing was fixed horizontally via clamps as it is demonstrated in *Figure 5.16*.

The shaker was connected to the structure from below with a stinger. A PCB 208C01 force sensor was also mounted between the stinger and the wing to measure the excitation force as shown in *Figure 5.17*. The force sensor is capable of measuring forces of ± 45 N within a frequency range of 0.01-36000 Hz with a sensitivity of 112.41 mV/N.

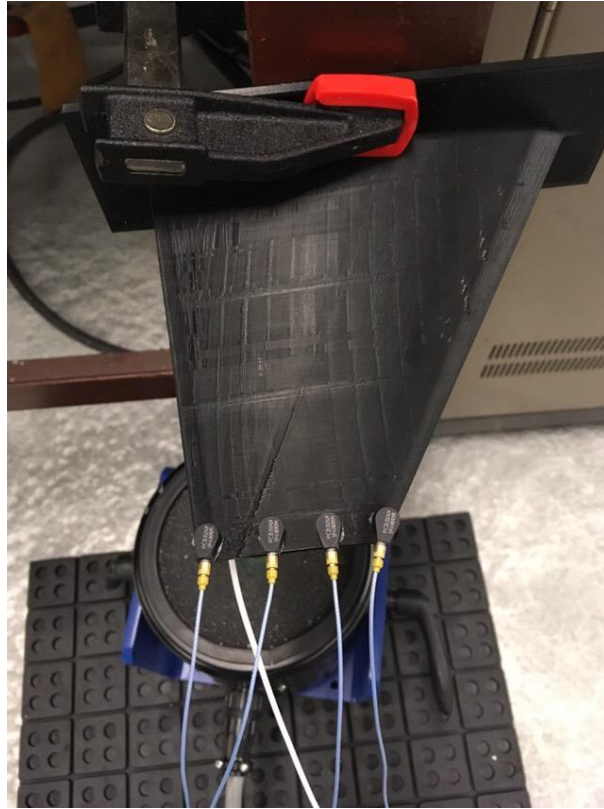


Figure 5.16 Wing fixture

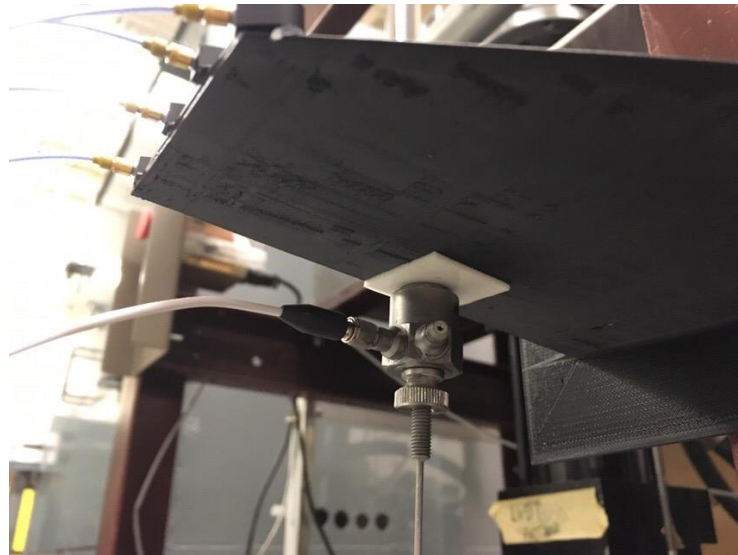


Figure 5.17 Force sensor mounted between a stinger and the wing

In order to measure the acceleration signals four PCB 352A24 miniature lightweight accelerometers were used. Utilized accelerometers are capable of measuring

accelerations of $\pm 490 \text{ m/s}^2$ within a frequency range of 1-8000 Hz and with $10.2 \text{ mV}/(\text{m/s}^2)$ sensitivity. The data from accelerometers and force sensors was sampled at 2048 Hz frequency. The accelerometers were placed on the top surface of the wing structure and were advanced span-wise towards root chord for each test case which is demonstrated below in *Figure 5.18*.

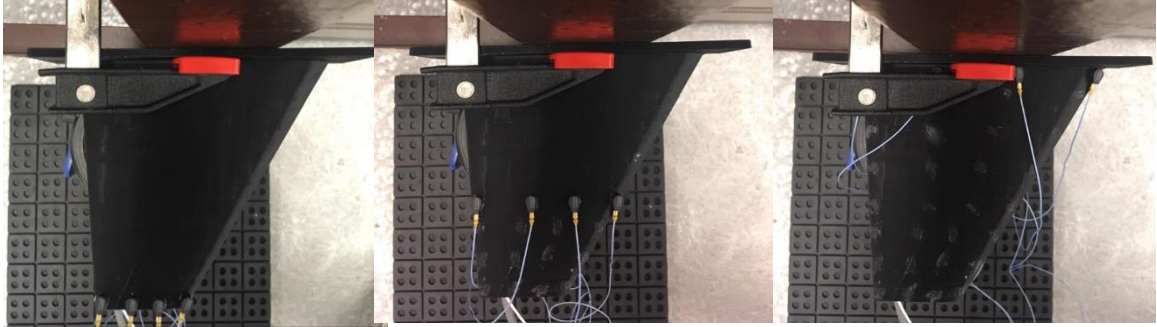


Figure 5.18 GVT test case 1, test case 4 and test case 8

In total 8 test cases were performed which resulted in 32 accelerometer output signals. As far as the input is concerned: the structure was excited by sine sweep wave input on dynamic shaker from 1 to 300 Hz in 600 seconds. This frequency range was chosen because the Nastran simulation showed that the 1st torsional mode has a natural frequency of 289.3 Hz.

An example of time domain response is shown in *Figure 5.19*. The data shows the accelerometer output signal and the input excitation force signal. The time response data for all 8 cases was transformed to frequency response data by utilizing empirical transfer function estimation and then it was analyzed in Matlab to obtain the natural frequencies and mode shapes within 0 to 300 Hz frequency range. *Figure 5.20* shows the single input-single output (SISO) frequency responses of the first test case and it can be observed that there are several peaks of magnitude, some of which correspond to natural frequencies of the structure.

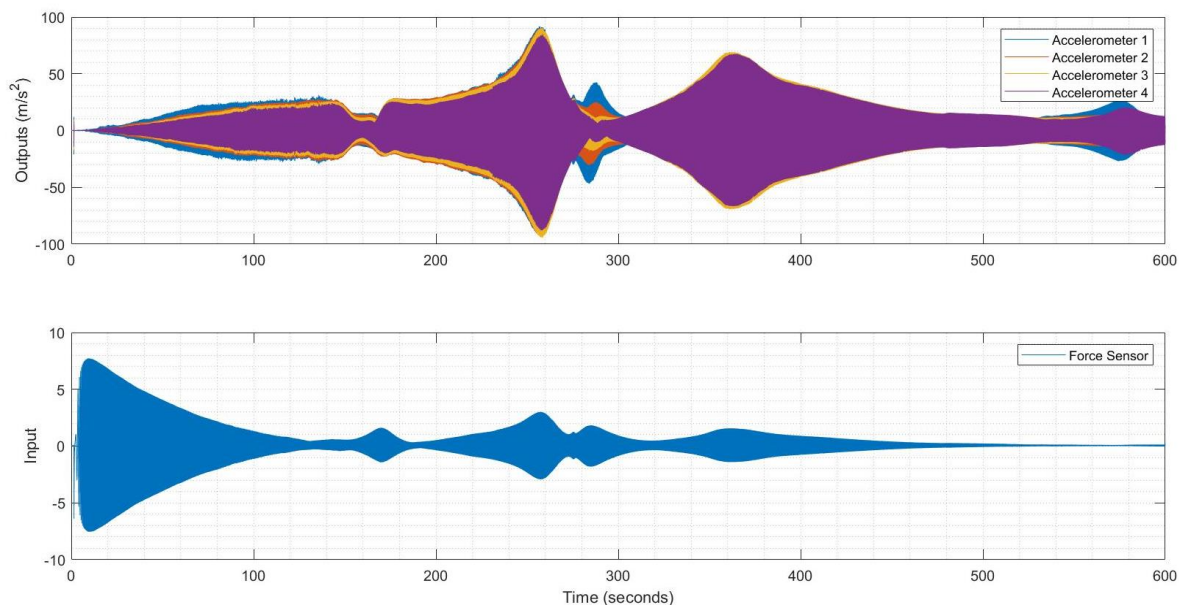


Figure 5.19 Time domain response corresponding to case 1

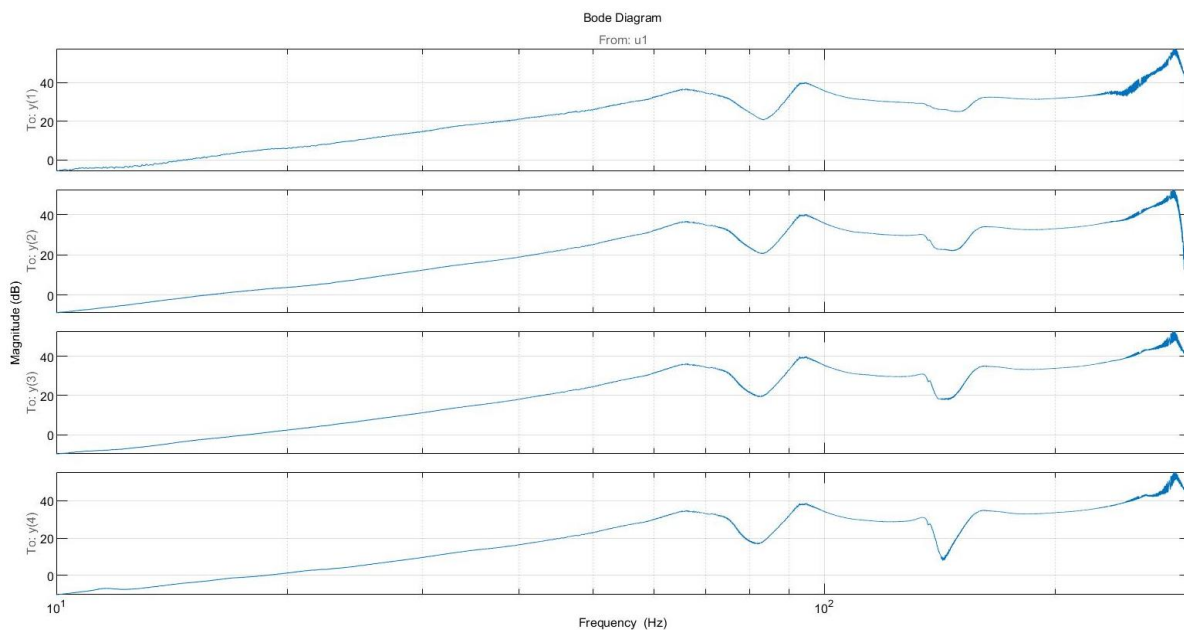


Figure 5.20 Frequency response from input force to acceleration response for case 1

After 32 individual SISO systems' frequency responses were obtained, the System Identification Toolbox from Matlab was used to identify the natural frequencies and estimate the model that would reproduce the dynamic behavior of the 3D printed wing. A state-space model with 32 states was found to be suitable in order to accurately

approximate the experimental results. The estimated model's states are all stable as shown in *Figure 5.21*. The worst and the best fits between the experimental data and the estimated model is presented in *Figure 5.22*.

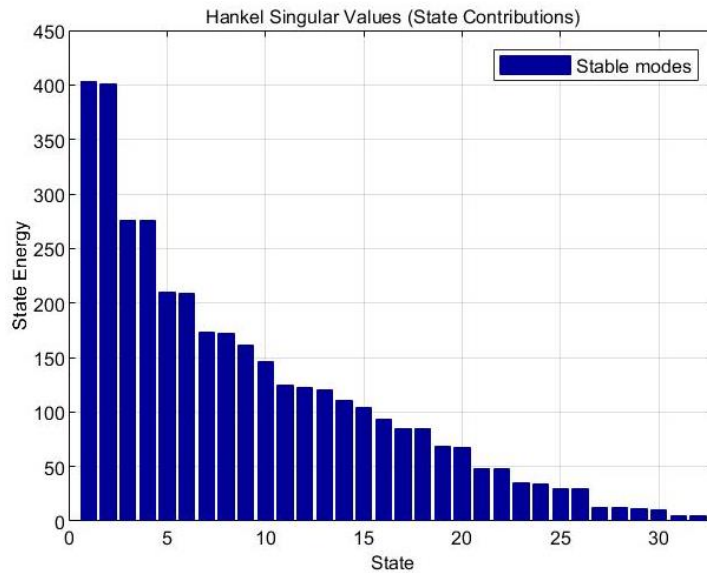


Figure 5.21 Hankel Singular Values for 32 order model

The analysis of the estimated model identified 4 modal frequencies within a range of frequencies from 1 to 300 Hz. The stability of the estimated model's modal parameters was checked as the order of the underlying model was varied, which is demonstrated in *Figure 5.23*. The inspection of the plot suggests that there are 4 modal frequencies which have values of approximately 65, 95, 165 and 285 Hz. However, in order to identify the wing's 1st bending and 1st torsion modes the mode shapes of the corresponding modal frequencies were visualized and compared to the Nastran modal simulation results.

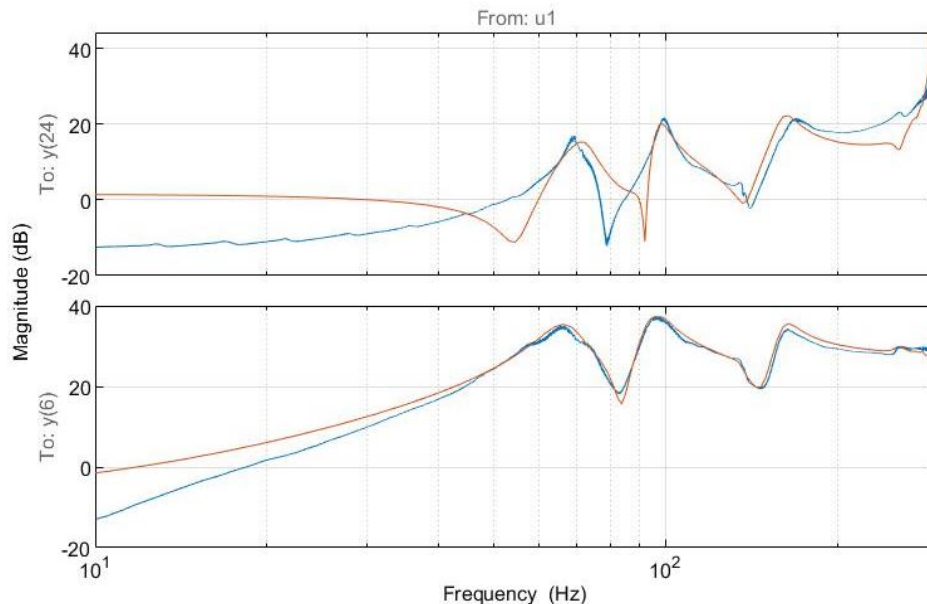


Figure 5.22 The worst (top) and the best (bottom) fit of the 32 order state-space model

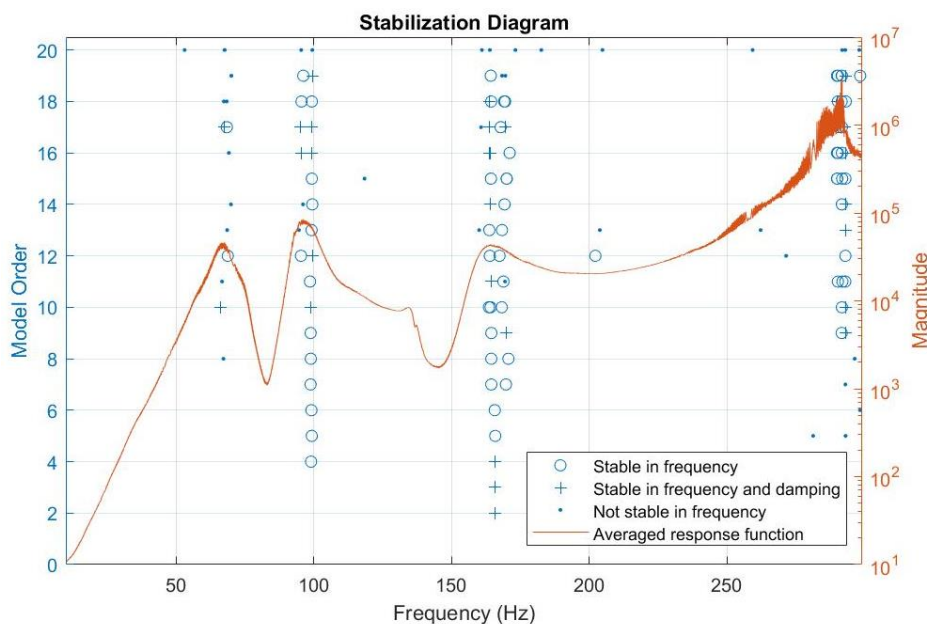


Figure 5.23 Stabilization diagram

Figure 5.24 and Figure 5.25 provide a comparison between experimentally obtained natural frequencies and mode shapes and simulated ones obtained in Nastran. The Nastran simulation showed that the 1st bending mode's frequency is 95.99 Hz which is very close to the experimental 94.31 Hz frequency shown in Figure 5.24. The 1st torsion mode's frequency obtained in Nastran is 273 Hz which is close to the experimentally

identified frequency of 283.3 Hz as it is shown in *Figure 5.25*. The mode shape of the 1st bending is very close to the experimentally obtained mode shape, however the 1st torsion mode shape obtained in Nastran has some discrepancies when compared to the experimentally obtained torsional mode which can be observed in *Figure 5.25*. This difference can be explained by the fact that Nastran modal analysis utilizes linearized model whereas experimentally obtained mode shape possesses non-linear dynamics that makes it look like a combination of torsional mode and residual minor effect of bending mode.

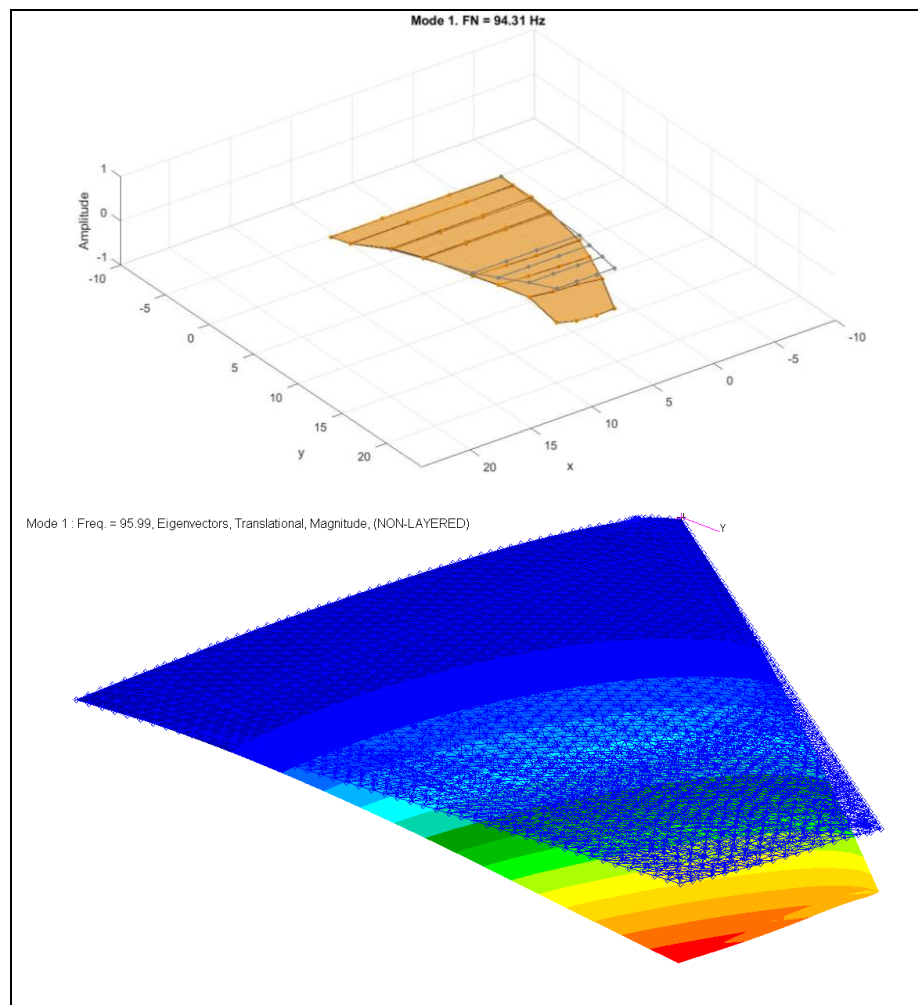


Figure 5.24 3D printed wing's experimental (top) and simulated (bottom) 1st bending mode

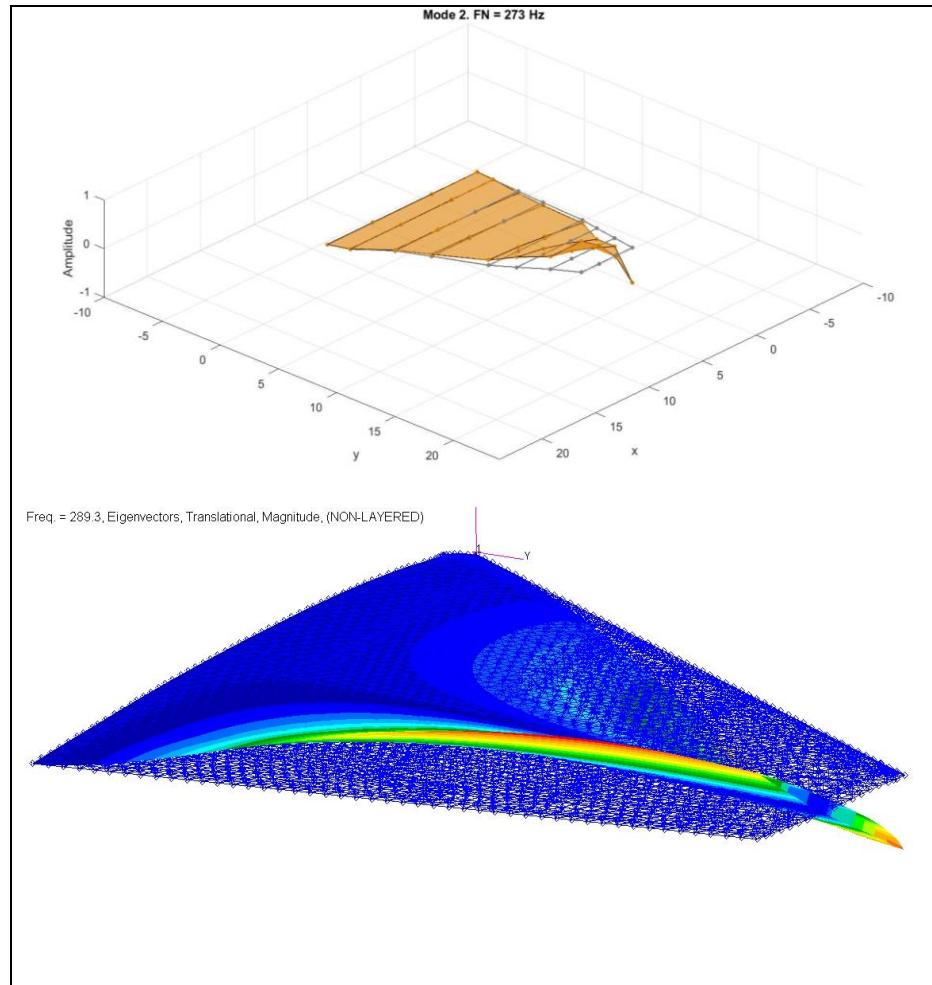


Figure 5.25 3D printed wing's experimental (top) and simulated (bottom) 1st torsion mode

Moreover, it can be noticed that the experimental values of frequencies are slightly smaller than the values obtained from simulation. This discrepancy can be attributed to the fact that the damping is not considered in Nastran simulation whereas the structural damping slightly reduces the natural frequency for the case of experiment. Similarly, the viscous damping might marginally contribute to this difference. Nevertheless, the experiment proved that the Nastran simulation accurately approximates the dynamic response of a 3D printed wing structure.

Since only the wing is planned to be tested, the flutter mechanism was chosen to be symmetric wing 1st bending/1st torsion flutter (SWBT) as it is experimentally simplest

mode to investigate and furthermore requires a simple fixture at the root (Pankonien, Reich, Lindsley & Smyers, 2017).

Prior to the manufacturing of the wing for the wind tunnel experiment, a feasibility study was performed in Patran/Nastran simulation environment to investigate whether the chosen flutter mode is attainable given dimensions and material. Thenceforth, the following section describes the future experimental setup for flutter analysis and is followed by the flutter analysis within the Nastran.

5.4 Experimental setup of the wing in ERAU wind tunnel

In order to experimentally test topologically optimized 3D printed internal structure of the wing, the new Embry-Riddle Aeronautical University's (ERAU) wind tunnel located at "MicaPlex" innovation complex was selected as to leverage its fairly large test section, which is 4 feet high, 6 feet wide and 12 feet long, and its nominal achievable flowspeed with mean turbulence intensity of less than 0.5%, which is 350 feet per second (0.3 Mach) (Langer, 2018). The depiction of ERAU wind tunnel test section is shown in *Figure 5.26*.

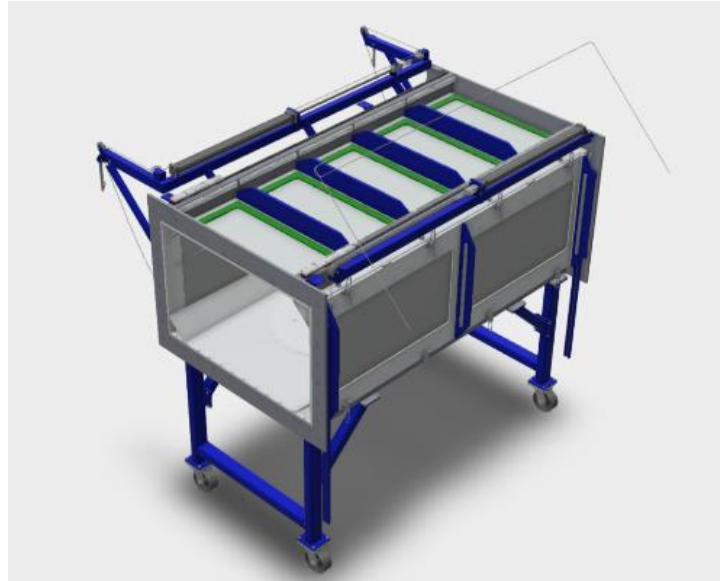


Figure 5.26 ERAU wind tunnel test section

ERAU wind tunnel's range of flowspeed allows for a more unrestrained 3D printed wing designs because it expands the choice of dimensions and material to be used by providing a wider range for the to-be-tested wing's stiffness that would inflict required flutter mechanism for experimental analysis.

There are several ways of placing the wing in the wind tunnel for aerodynamic tests. Placing the wing vertically attached to the ground or to the top wall (ceiling) of the test section could be considered as one of configurations (Ballman et al., 2011; Matsuzaki, Ueda, Miyazawa & Matsushita, 1989). Another configuration of placing the wing is to attach it to the sidewall of the wind tunnel horizontally (Scott, Coulson, Castelluccio & Heeg, 2011; Tang & Dowell, 2001) or vertically (Pankonien, Reich, Lindsley & Smyers, 2017). Further variation of this method is to attach the wing horizontally to a splitter plate (Ricketts & Doggett, 1980; Heeg, Wieseman & Chwalowski, 2016; Huang, Zhao & Hu, 2016). After thorough consideration it was decided to install wing model inside ERAU wind tunnel vertically mounted on a splitter

plate as demonstrated in Figure 5.27. The main reasons for this decision are the ease of manufacturing of the splitter plate, simple fixture using existing screw-threads on a turntable (no modification of ERAU wind tunnel section will be required) and ability to change angle of attack for each run. Wing mount that is connected to the splitter plate is perforated so as to allow positioning the wing at desired angle of attack with a step of 2 degrees.

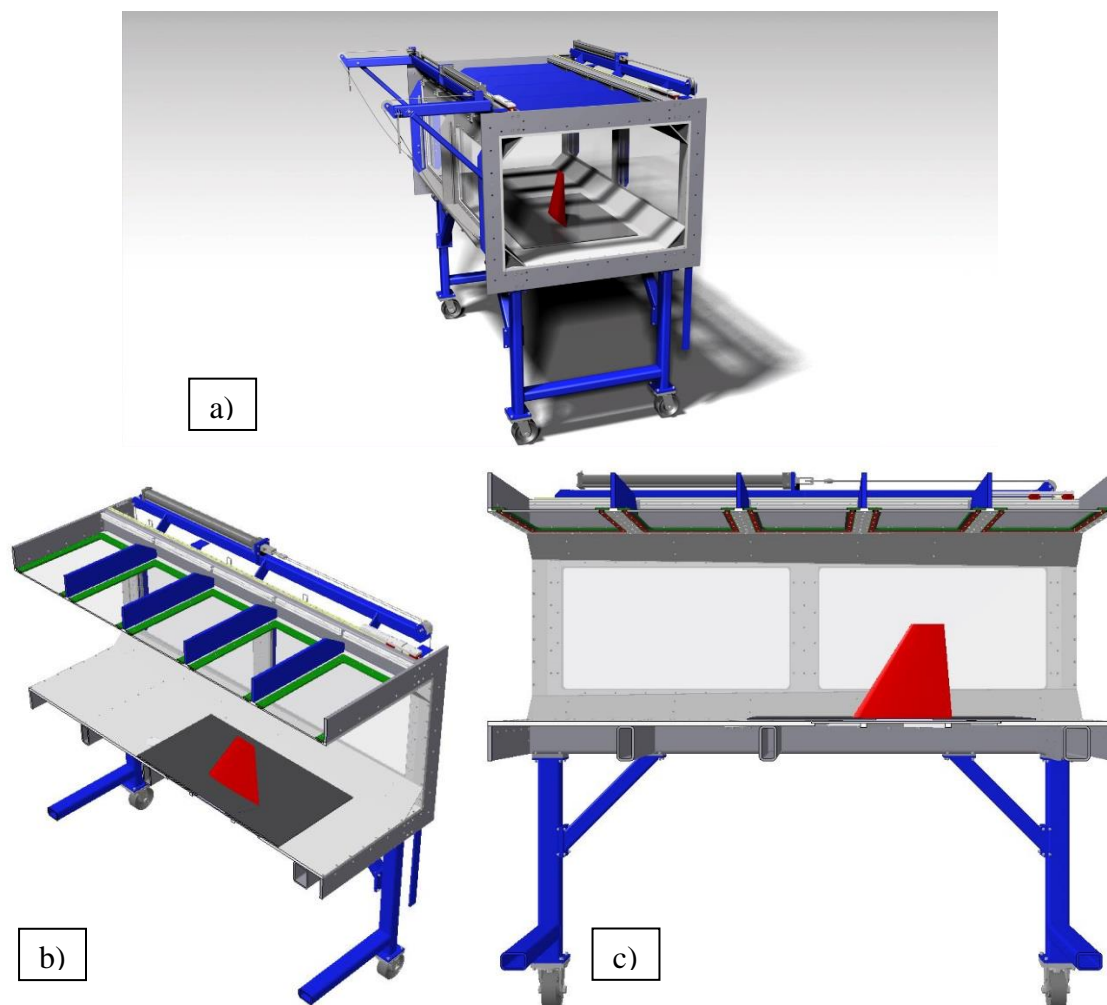


Figure 5.27 Visualization of ERAU wind tunnel section with wing model a) Rendered b) Isometric sectioned and c) Isometric side views.

The dimensions of the wing for the experimental analysis in wind tunnel is limited by the height of the test section, which is 4 feet. The dimensions of the wing that fits the

test section in the configuration described earlier is demonstrated in *Figure 5.28*.

5.5 Modal and aeroelastic analysis in Nastran/Patran

Prior to flutter analysis a modal analysis was performed in Nastran with a scaled wing made from polypropylene material called “Durus” $E = 1.1 \text{ GPa}$ produced by “Stratasys” company (Stratasys, 2018). The dimensions of the scaled wing are shown in *Figure 5.28*.

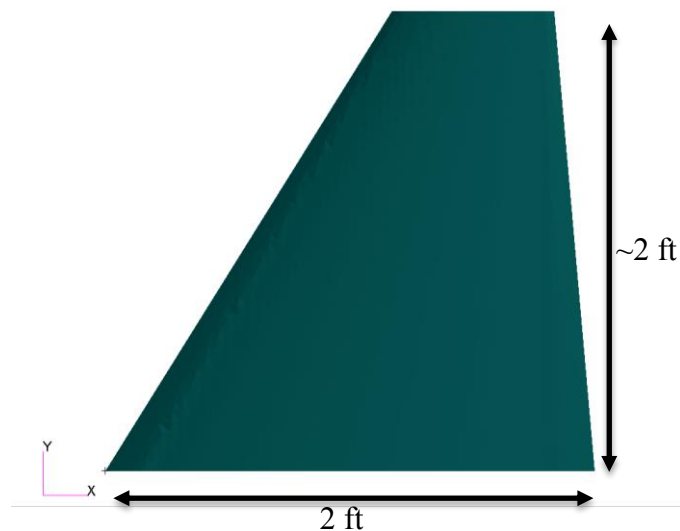


Figure 5.28 Top view of the wing model with dimensions

The results of the analysis showed that the first natural frequency is 18.66 Hz and the corresponding mode was 1st bending which is demonstrated in *Figure 5.29*. The second natural frequency yield a value of 57.19 Hz with the corresponding mode of 1st torsion which is shown in *Figure 5.30*. 2nd bending and 2nd torsion frequencies are at 71.79 and 122.5 Hz respectively. 1st torsional mode’s frequency was found to be lower than the 2nd bending mode, resulting in a favorable symmetric wing bending torsion flutter mechanism. Symmetric Wing Bending Torsion (SWBT) flutter mechanism is experimentally the simplest flutter mode to investigate since it does not include a rigid

body degree of freedom (Pankonien, Reich, Lindsley & Smyers, 2017), easing the mounting implementation via fixed root which is crucial for the future wind tunnel test.

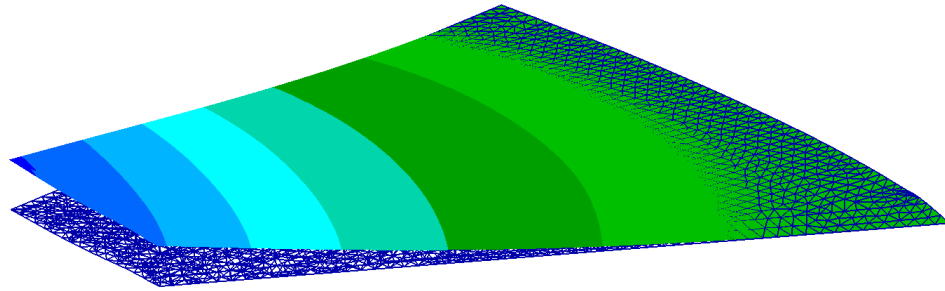


Figure 5.29 1st bending at 18.66 Hz

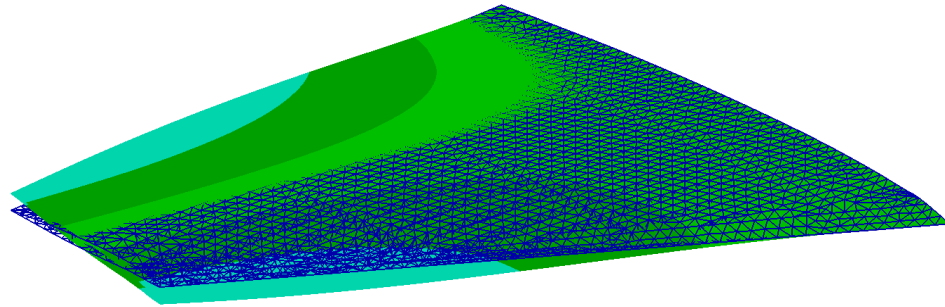


Figure 5.30 1st torsion at 57.19 Hz

Preliminary flutter analysis was carried out in Nastran's aeroelastic module. A case study was conducted in which 2 wing dimensions (2ft and 3ft) were tested. The results are $v - g$ and $v - f$ plots that demonstrate the velocity versus damping and velocity versus frequency curves, where g represents the structural damping of the vibration. The velocity at which the curve on the $v - g$ plot passes the x-axis so that the value of $g = 0$ is called the flutter speed. It is possible to determine the frequencies of the modes at flutter speed by picking the value of the velocity at which the curve passes the x-axis in *Figure 5.31* and finding values of frequencies corresponding to that velocity in *Figure 5.32*.

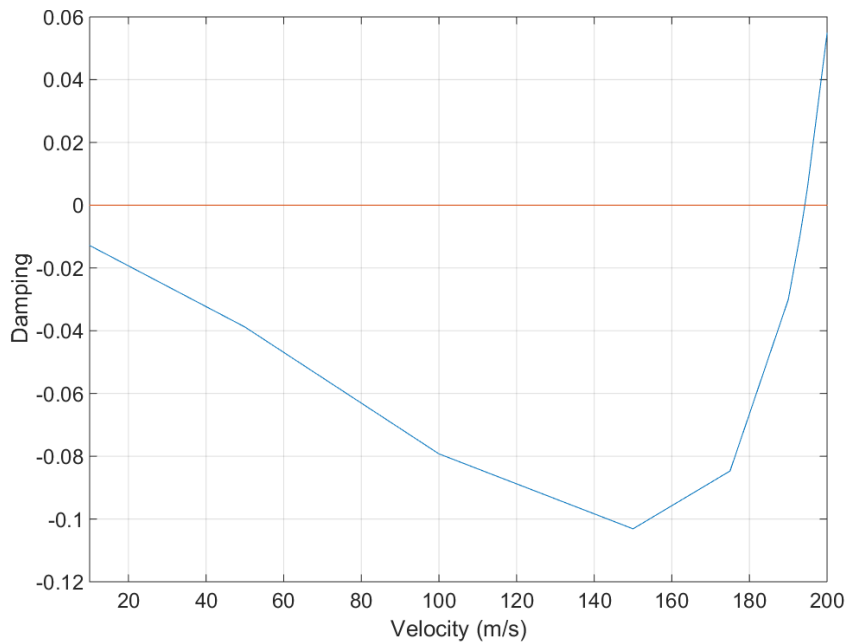


Figure 5.31 $v - g$ plot of F-5 wing, “Durus” material, $E = 1.1 \text{ GPa}$, 2 feet

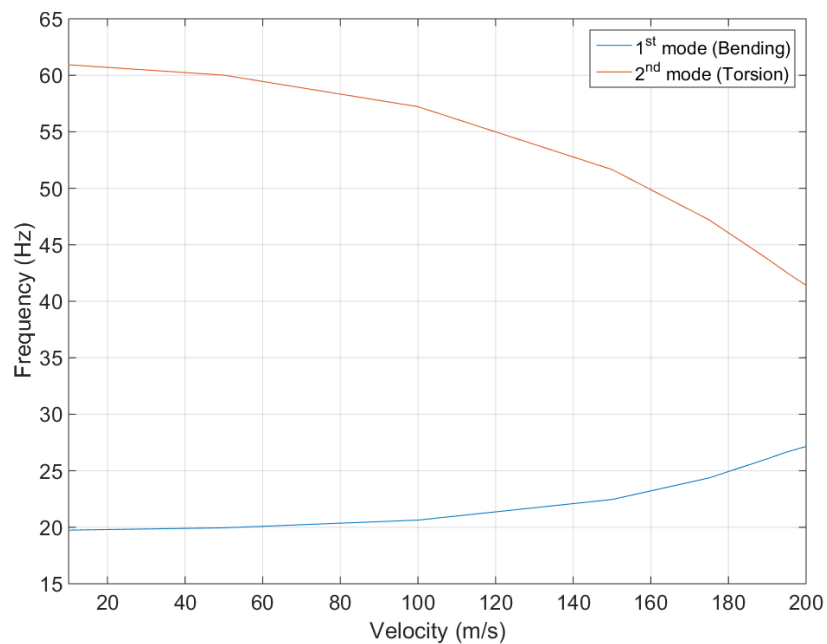


Figure 5.32 $v - f$ plot of F-5 wing, “Durus” material, $E = 1.1 \text{ GPa}$, 2 feet

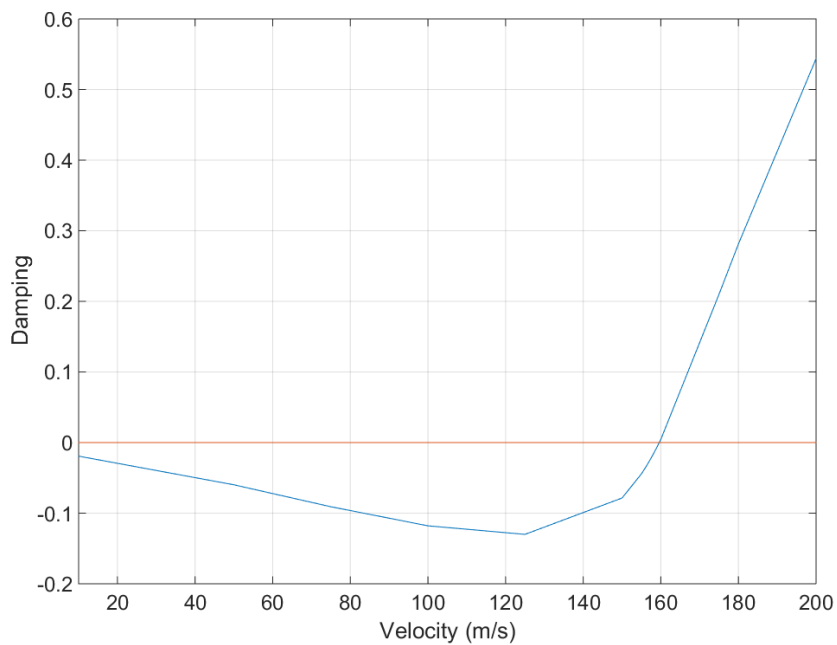


Figure 5.33 $v - g$ plot of F-5 wing, “Durus” material, $E = 1.1 \text{ GPa}$, 3 feet

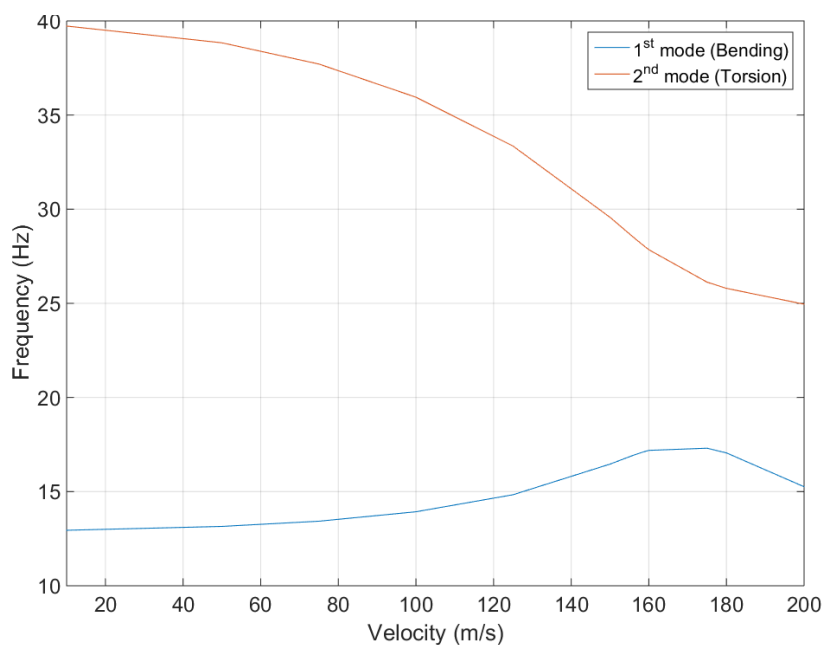


Figure 5.34 $v - f$ plot of F-5 wing, “Durus” material, $E = 1.1 \text{ GPa}$, 3 feet

For the case of 2 feet wing model the flutter speed was calculated to be 195 m/s as shown in Figure 5.31 and Figure 5.32. If the model size is increased to 3 feet it can be seen that the corresponding flutter speed is decreased. This is demonstrated in Figure 5.33 and

Figure 5.34 where flutter speed was found to be 160 m/s. The data relevant to the flutter analysis is tabulated in Table 5.3.

Table 5.3

Case study design of flutter model via stiffness and dimension control

Case		Natural Frequencies (Hz)			Predicted Flutter Speed (m/s)
Material	Characteristic Dimension	1st Bending	1st Torsion	2nd Bending	
Durus (E=1.1GPa) - Homogeneous	2 feet root chord	18.7	57.2	71.8	195
	3 feet root chord	13.3	40.4	60.6	160

As it can be seen from Table 5.3 the flutter speed is significantly higher than the ERAU wind tunnel's flowspeed limit of 100m/s. If a lower flutter speed is desired, elastomeric breaks can be incorporated in the wing model to reduce its torsional stiffness which in case would lower the torsional frequency thus lowering the flutter speed (Pankonien, Reich, Lindsley & Smyers, 2017).

Another case study was conducted to see how the flutter speed changes as the thickness of the wing model's walls are varied from 1.5 mm to 5 mm. The results are demonstrated in *Figure 5.35*, *Figure 5.36* and *Figure 5.37*. For the case of 1.5 mm wall thickness the flutter speed was obtained to be 112 m/s as shown in *Figure 5.35*. As the thickness is increased to 2.5 mm the flutter speed increases as well and reaches 139 m/s as demonstrated in *Figure 5.36*. Finally, *Figure 5.37* demonstrates a wing configuration with a wall thickness of 5 mm which has the flutter speed of 195 m/s. This simulation demonstrates that even by decreasing wing walls' thickness to 1.5 mm the flutter is still not reached given ERAU wind tunnel's limitation of 100 m/s.

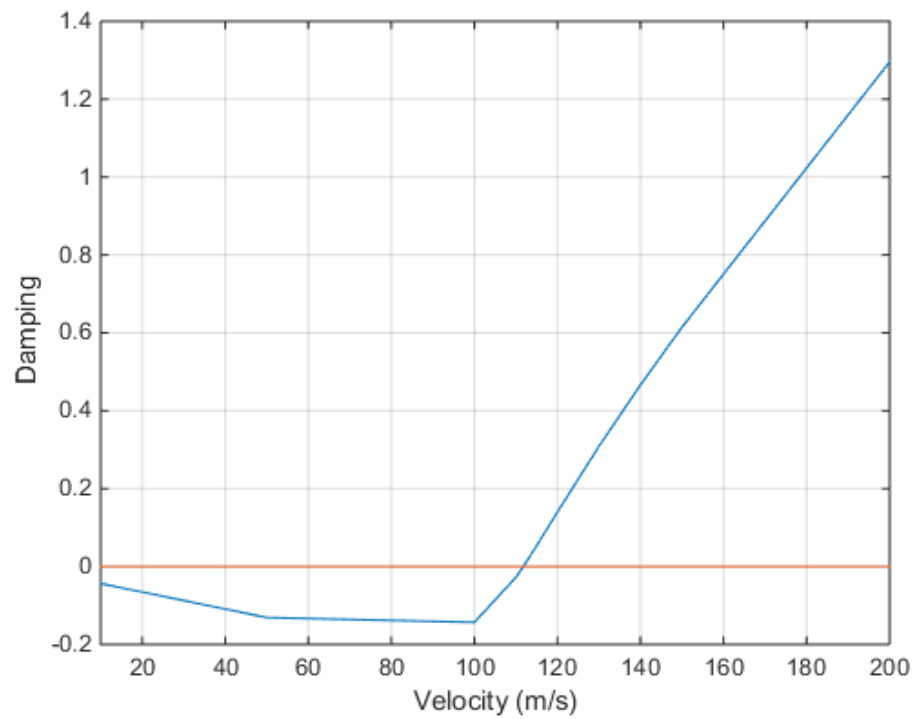


Figure 5.35 $v - g$ plot of F-5 wing, "Durus" material, $E = 1.1 \text{ GPa}$, 2 feet, 1.5 mm

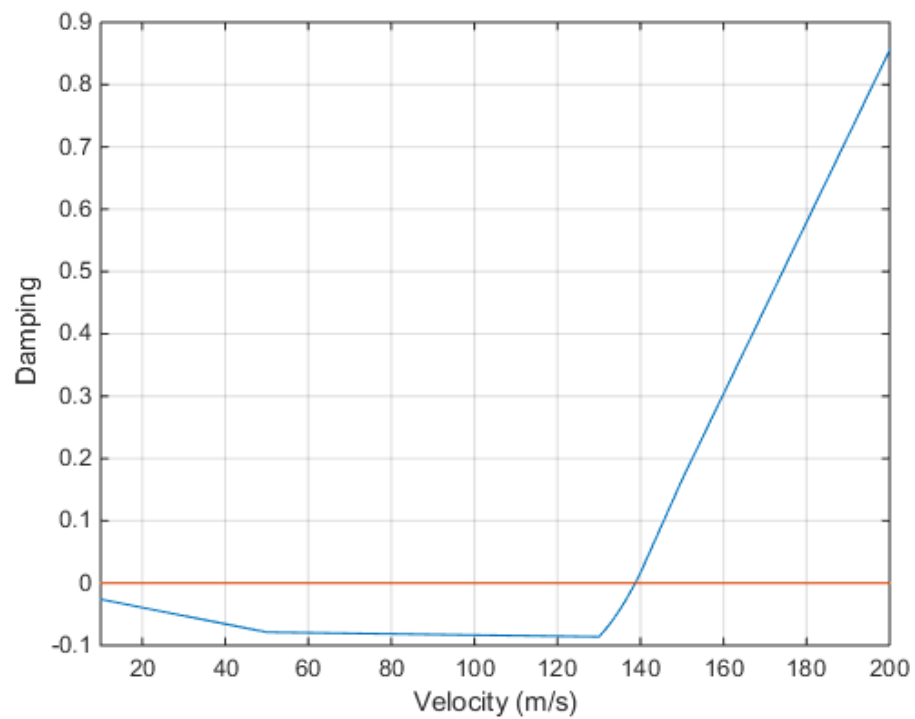


Figure 5.36 $v - g$ plot of F-5 wing, "Durus" material, $E = 1.1 \text{ GPa}$, 2 feet, 2.5 mm

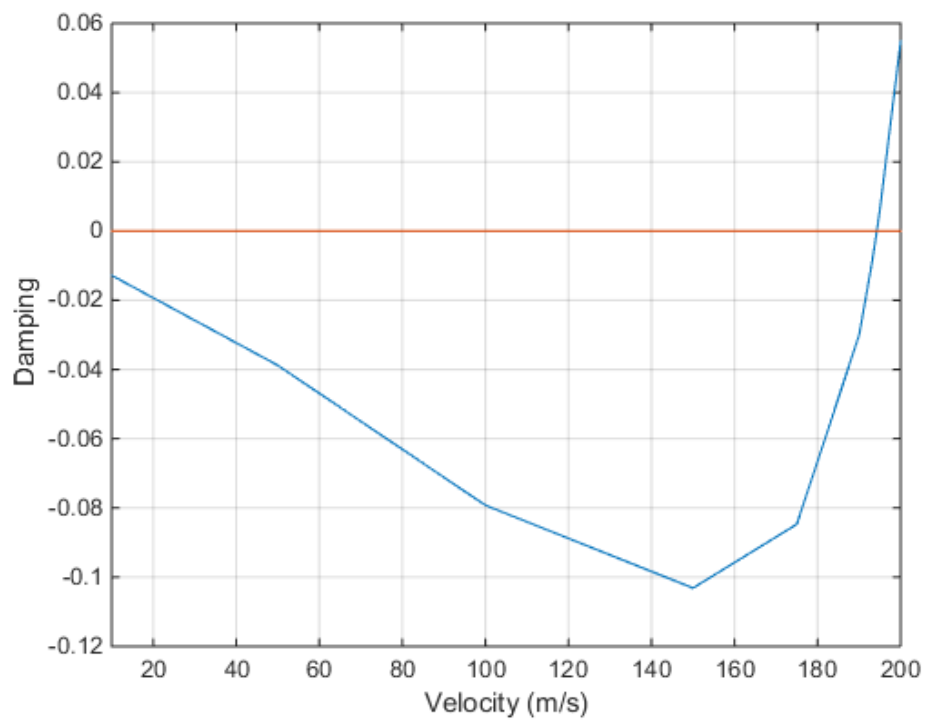


Figure 5.37 $v - g$ plot of F-5 wing, "Durus" material, $E = 1.1 \text{ GPa}$, 2 feet, 5.0 mm

6. Concluding remarks and future work

In the course of this work a significant part of aeroelastic modelling software was developed. Steady aerodynamics was modeled using vortex lattice method (VLM) and the unsteady aerodynamics was modeled using doublet lattice method (DLM). Triangular bending elements were used as a basis for a finite element method (FEM) in this work. The interpolation required to relay the results obtained from the DLM into the structural modal space (FEM) was developed as well. Moreover, a static, modal and aeroelastic analyses of F-5 wing were performed in the framework of Nastran's solver. Consequently, a prototype 3D printed F-5 wing was manufactured and a static and ground vibrational test (GVT) analyses for the purpose of validation were carried out.

The static experiment performed using 3D printed wing prototype and digital image correlation (DIC) technique showed that the finite element (FE) model is in good agreement with the experiment. Furthermore, a ground vibration test (GVT) showed that the computational modal analysis performed in Nastran is in good agreement with the experimental results. The results of the flutter analysis performed in Nastran showed that the 2 feet wing made from "Durus" 3D printing material is not going to flutter within the limit of ERAU wind tunnel's maximal flowspeed of 100 m/s. Additional flutter analysis in Nastran was carried out to see if the reduction in wing walls' thickness leads to an attainable wing bending torsion flutter. The results of this analysis showed that even reducing thickness to 1.5 mm does not result in wing fluttering below 100 m/s.

The analyses and experiments performed in this work allow for several new avenues of additional research work as well as experiments to be explored. Experimental flutter analysis results can be obtained by testing the larger 2 feet wing inside the ERAU

wind tunnel as explained in Chapter 5. Results of this analysis might be used as a source of validation for the developed Matlab Aeroelastic Code

REFERENCES

- Albano, E. and Rodden, W. P. (1969). A doublet-lattice method for calculating lift distributions on oscillating surfaces in subsonic flows. *AIAA Journal of Aircraft*, Vol. 7, No. 2, pp. 279–285.
- Anderson Jr John, D. (1984). *Fundamentals of aerodynamics*. McGraw-Hill.
- Ballmann, J., A. Boucke, B. Chen, L. Reimer, L. Reimer, M. Behr, M. Behr et al. (2011). Aero-structural wind tunnel experiments with elastic wing models at high Reynolds numbers (HIRENASD-ASDMAD). In *49th AIAA Aerospace Sciences Meeting Including the New Horizons Forum and Aerospace Exposition*, p. 882.
- Bisplinghoff, Raymond L., and Holt Ashley. (2013). *Principles of aeroelasticity*. Courier Corporation.
- Chinmaya, Panda, and S. R. P. Venkatasubramani. (2009). Aeroelasticity-in general and flutter phenomenon. In *Emerging Trends in Engineering and Technology (ICETET), 2009 2nd International Conference on*, pp. 81-85. IEEE.
- Clough, Ray W. (1965). Finite element stiffness matrices for analysis of plate bending. In *Proc. of the First Conf. on Matrix Methods in Struct. Mech.*, pp. 515-546.
- Fung, Y. C. (2002). *An introduction to the theory of aeroelasticity*. Courier Corporation.
- Harder, Robert L., and Robert N. Desmarais. (1972). Interpolation using surface splines. *Journal of aircraft* 9, no. 2: 189-191.
- Heeg, Jennifer, Carol D. Wieseman, and Pawel Chwalowski. (2016). Data comparisons and summary of the second aeroelastic prediction workshop.
- Huang, Rui, Yonghui Zhao, and Haiyan Hu. (2016). Wind-tunnel tests for active flutter control and closed-loop flutter identification. *AIAA Journal* 54, no. 7: 2089-2099.
- J.L. Tocher. (1962). *Analysis of plate bending using triangular elements*. Ph.D. dissertation. University of California, Berkeley.
- Katz, J. and Plotkin, A. (1991). *Low speed aerodynamics: From wing theory to panel Methods*. New York: McGraw-Hill Book Co.
- Kehoe, Michael W. (1995). *A historical overview of flight flutter testing*.
- Kier, Thiemo M., and Gertjan Looye. (2009). Unifying manoeuvre and gust loads analysis models. In *International Forum on Aeroelasticity and Structural Dynamics*.

- Kotikalpudi, A. (2017). Robust Flutter Analysis for Aeroservoelastic Systems (Thesis). Retrieved from https://www.aem.umn.edu/~SeilerControl/Thesis/2017/Kotikalpudi_17PhD_RobustFlutterAnalysisForASESystems.pdf
- Kotikalpudi, Aditya, Harald Pfifer, and Gary J. Balas. (2015). Unsteady aerodynamics modeling for a flexible unmanned air vehicle. In AIAA Atmospheric Flight Mechanics Conference, p. 2854.
- Lanchester, F. W. (1916). Torsional Vibrations of the Tail of an Aeroplane. Aeronaut. Research Com. R & M 276.
- Lessing, Henry C., John L. Troutman, and Gene P. Menees. (1960). Experimental determination of the pressure distribution on a rectangular wing oscillating in the first bending mode for Mach numbers from 0.24 to 1.30. Vol. 344. National Aeronautics and Space Administration.
- Livne, Eli. (2017). Aircraft active flutter suppression: State of the art and technology maturation needs. *Journal of Aircraft* 55, no. 1: 410-452.
- Locatelli, D., Yeilaghi Tamijani, A., Mulani, S. B., Liu, Q., & Kapania, R. K. (2013). Multidisciplinary optimization of supersonic wing structures using curvilinear spars and ribs (SpaRibs). In 54th AIAA/ASME/ASCE/AHS/ASC Structures, Structural Dynamics, and Materials Conference (p. 1931).
- MakerBot Industries. (2018). MakerBot Replicator 2X User Manual. Brooklyn, NY: Author
- Mason, H. (1998). Aerodynamics of 3D Lifting Surfaces through Vortex Lattice Methods. Applied Computational Aerodynamics. Department of Aerospace and Ocean Engineering Virginia Polytechnic Institute and State University, Blacksburg, Virginia 24061: 72.
- Matsuzaki, Y., T. Ueda, Y. Miyazawa, and H. Matsushita. (1989). Gust load alleviation of a transport-type wing-test and analysis. *Journal of aircraft* 26, no. 4: 322-327.
- Melin, Tomas. (2000). User's guide and reference manual for Tornado. Royal Institute of Technology (KTH), Department of aeronautics, Sweden.
- Model 2060E Modal Shaker. The Modal Shop. 3149 E Kemper Road, Cincinnati, OH 45241, USA. www.modalshop.com
- Moran, J. (1991). An Introduction to Theoretical and Computational Aerodynamics. Dover Publications.
- NASA Armstrong Fact Sheets - Active Aeroelastic Wing, [online]. Available :

<https://www.nasa.gov/centers/armstrong/news/FactSheets/FS-061-DFRC.html>

- Pankonien, Alexander M., Gregory W. Reich, Ned Lindsley, and Brian Smyers. (2017). 3D-Printed Wind Tunnel Flutter Model. In 58th AIAA/ASCE/AHS/ASC Structures, Structural Dynamics, and Materials Conference, p. 0411.
- Rao, Singiresu S. (2017). The finite element method in engineering. Butterworth-Heinemann.
- Ricketts, Rodney H., and Robert V. Doggett Jr. (1980). Wind-tunnel experiments on divergence of forward-swept wings.
- Rodden, William P., and Erwin H. Johnson. (1994). MSC/NASTRAN aeroelastic analysis: user's guide; Version 68. MacNeal-Schwendler Corporation.
- Rodden, William P., Paul F. Taylor, and Samuel C. McIntosh. (1998). Further refinement of the subsonic doublet-lattice method. *Journal of Aircraft* 35, no. 5: 720-727.
- Rodden, William P., Paul F. Taylor, Samuel C. McIntosh, and Myles L. Baker. (1999). Further convergence studies of the enhanced doublet-lattice method. *Journal of aircraft* 36, no. 4: 682-688.
- Scott, Robert, David Coulson, Mark Castelluccio, and Jennifer Heeg. (2011). Aeroservoelastic Wind-Tunnel Tests of a Free-Flying, Joined-Wing SensorCraft Model for Gust Load Alleviation. In 52nd AIAA/ASME/ASCE/AHS/ASC Structures, Structural Dynamics and Materials Conference 19th AIAA/ASME/AHS Adaptive Structures Conference 13t, p. 1960.
- Shames, I. H. (1982). *Mechanics of fluids*. McGraw-Hill New York.
- Stratasys. (2018). *Durus*. Eden Prairie, MN: Author
- T. Langer. (2018). Acceptance Test Report, ERAU Low Speed Wind Tunnel. Test report.
- Tamijani, A. Y., Gharibi, K., Kobayashi, M. H., & Kolonay, R. M. (2018). Load paths visualization in plane elasticity using load function method. *International Journal of Solids and Structures*, 135, 99-109.
- Tang, Deman, and Earl H. Dowell. (2001). Experimental and theoretical study on aeroelastic response of high-aspect-ratio wings. *AIAA journal* 39, no. 8: 1430-1441.
- Watkins, Charles E. (1959). Donald S. Woolston, and Herbert J. Cunningham. A systematic kernel function procedure for determining aerodynamic forces on oscillating or steady finite wings at subsonic speeds.

William P. Rodden. (1959). Further remarks on matrix interpolation of flexibility influence coefficients. *Journal of the Aerospace Sciences* 26, no. 11: 760-761.

VIC3D. Correlated Solutions Incorporated. 120 Kaminer Way Parkway Suite, Columbia, SC 29210, USA. www.correlatedsolutions.com.